ASSESSMENT OF TIP PLANFORM EFFECTS ON THE HOVER CHARACTERISTICS OF HELICOPTER ROTORS

A Dissertation
Presented to
The Academic Faculty

by

Chong Zhou

In Partial Fulfillment of the
Requirements for the Degree
Doctor of Philosophy in the
Aerospace Engineering

Georgia Institute of Technology
May 2019

ASSESSMENT OF TIP PLANFORM EFFECTS ON THE HOVER CHARACTERISTICS OF HELICOPTER ROTORS

Approved by:

Dr. Lakshmi N. Sankar, Advisor
School of Aerospace Engineering
Georgia Institute of Technology

Dr. Daniel P. Schrage
School of Aerospace Engineering
Georgia Institute of Technology

Dr. Jonnalagadda V. R. Prasad
School of Aerospace Engineering
Georgia Institute of Technology

Dr. Jechiel Jagoda
School of Aerospace Engineering
Georgia Institute of Technology

Dr. Philip Griffin
School of Engineering
University of Limerick

Date Approved: 03/13/2019

Dedicated to my parents,

Yi ZHOU and Xinxia QIAN

for their unconditional love and support

ACKNOWLEDGEMENTS

First I would like to express my sincere and heartfelt gratitude to my advisor and mentor, Dr. Lakshmi N. Sankar, for his guidance, patience, motivation and constant support over the years. I am indebted to his help in all the time of research and writing of this thesis. His encouragement and kind advice has made this work possible.

My appreciation also goes to Dr. Daniel P. Schrage and Dr. Jonnalagadda V. R. Prasad for their mentorship, support, and insightful comments during my thesis proposal which motivated me to widen my research from various perspectives. I would also like to thank my thesis committee members Dr. Lakshmi N. Sankar, Daniel P. Schrage, Dr. Jonnalagadda V. R. Prasad, Dr. Jechiel Jagoda and Dr. Philip Griffin for their valuable comments and suggestions for improvement of the thesis.

I have had a wonderful time in Georgia. I would like to thank all my friends and colleagues, Dr. Jeewoong Kim, Dr. Ritu Marpu Eshcol, Eliya Wing, Dr. Alpha Bah, Muhammad Ali, Zhihang Liu, Rajeev Atluri, Stephen Marone, Nana Obayashi, Powei Chen, Avani Gupta, Luke S. Battey, Dr. Zhangxian and Yuan Zhenhao Jing for their friendship and support during my years in the CFD lab.

Special thanks go to Dr. Jeewoong Kim (ART Inc.) and for his extensive help through a significant fraction this research and his vast experience in GT-Hybrid, and to Dr. Ritu Marpu Eshcol (Siemens PLM software) for her kind advising with STAR-CCM+.

I would like to thank the Rotorcraft Simulation Working Group for collaborating on all of our research activities on the assessment of the current state-of-the-art rotor hover

prediction technologies. Thanks to Dr. Nathan Hariharan and Dr. Brian E. Wake for their guidance and comments on this work.

Last but not least, I would like to thank my parents for their encouragement, support, patience and love. I cannot thank them enough for encouraging me throughout this wonderful experience.

TABLE OF CONTENTS

LIST OF TABLES

LIST OF FIGURES

LIST OF SYMBOLS AND ABBREVIATIONS

a	Speed of sound
A	Rotor disk area
b	Rotor blade number
c	Blade chord length
$C_n M^2$	Normal force coefficient, $N/(\frac{1}{2}\rho a^2 c)$
$C_{pm} M^2$	Pitching Moment coefficient, $PM/(\frac{1}{2}\rho a^2 R^2)$
$C_{fm} M^2$	Flapping Moment coefficient, $FM/(\frac{1}{2}\rho a^2 R^2)$
C_P	Power coefficient, $P/(\rho_\infty A V_{tip}^3)$
C_T	Thrust coefficient, $T/(\rho_\infty A V_{tip}^2)$
D	Rotor drag force, wind axis, positive rearward
k	Turbulence kinetic energy
L	Lift force
M_a	Freestream Mach number
M_{atip}	Advancing tip Mach number, $(\Omega R + V_\infty)/a$
P	Rotor power
q	Free stream dynamic pressure, $\frac{1}{2}\rho {V_\infty}^2$
r	Blade radial station, measured from center of rotation

R	Rotor radius
R_e	Reynolds number
Δs	First layer mesh thickness
V_∞	Free stream velocity
y^+	Viscous sub-layer length scale, $y\sqrt{\rho\tau_w}/\mu$

Greek Symbols

α	Shaft angle of attack
β_0	Blade coning angle
β_{1s}	Lateral flapping angle relative to shaft
β_{1c}	Longitudinal flapping angle relative to shaft
Γ	Blade section circulation
ε	Turbulence dissipation rate
θ_0	Blade collective pitch angle at $75\%\ R$
θ_{1c}	Longitudinal pitch angle in the shaft plane
θ_{1s}	Lateral pitch angle in the shaft plane
μ	Advance ratio
υ_T	Eddy viscosity
ρ	Air density
σ	Solidity, $bc/\pi R$
Ω	Rotor angular velocity in radians/sec

Subscripts and	Symbols
i, j, k	Indices in three coordinate directions, tensor notation
$\frac{D(\ \ )}{Dt}$	Substantial derivative
< >	Reynolds averaged quantities
$(\tilde{\ \ })$	Roe-average
$(\ \ )_{L,C,R}$	Left face, center, or right face of a cell

SUMMARY

Helicopter industry has spent much effort in improving rotor performance in hover and forward flight for decades by optimizing the blade configuration and adding passive and active control devices. Over time people have realized that the tip planform plays an important role in rotor performance both in hover and in forward flight. Tip planform also plays a role in rotor noise and blade vibrations. However, there is no universal shape for all missions, and tradeoffs are always needed to optimize the rotor performance over a range of flight conditions. Understanding the effects of different tip planforms is important for engineers and researchers to explain and predict the performance of a particular rotor configuration over a multitude of operating conditions.

Some aspects of tip shape variations are well understood. For example, blade element-momentum theory states that a combination of taper and twist can produce nearly uniform inflow velocity minimizing induced power. Furthermore, if the twist is properly chosen, the sectional lift to drag ratio could also be maximized. Sweeping the tip will mitigate the formation of shock waves over the tip, thus reducing both the wave drag and noise. Other aspects of the tip shape, in particular the anhedral effects, are not adequately understood.

Anhedral tip shapes have been successfully introduced on different blades since the end of the 1990s. Yet the mechanism of how it works on the blade was not completely understood at that time. It was clear that the tip vortex was displaced downwards in the wake by anhedral. However, how the displaced vortex position affects the flow field and the strength of the vortices-blade interaction cannot be easily visualized or quantified by

experimental means alone. With the advent of advanced computational fluid dynamics (CFD) tools, it has now become possible to systematically study the effects of tip planform shape (taper, twist, sweep, anhedral) on hover performance.

The objective of this research is to capture and investigate the effects of blade tip planform on rotor aerodynamics in hover. This work is guided by a set of test data for several advanced planforms, with the S-76 rotor serving as the baseline. Two complementary numerical modeling approaches – a hybrid Navier-Stokes/fee wake approach, and a wake capturing approach – are used to study the rotor aerodynamics in hover and forward flight. The present studies indicate that the rotor performance, as measured by the figure of merit, improves when anhedral is introduced. Anhedral rotors are seen to produce a smother blade loading and a more uniform inflow, which is expected to result in reduced induced power for a given thrust loading. In forward flight, the anhedral tip behaved similar to the baseline swept tapered tip. A judicious combination of twist, taper, and anhedral may be used within a CFD framework such as the one described here to design rotors that have excellent hover and forward flight characteristics.

CHAPTER 1. INTRODUCTION

1.1 Preliminary Remarks

A distinguishing feature of helicopters compared to other flight vehicles is their reliance on the main rotor for all forces and moments needed to operate the vehicle. With the use of cyclic and collective pitch, pilots can readily vary and control the thrust, propulsive and side forces. Pilots can also control the vehicle attitude by tilting the rotor disk. Because helicopters spend a bulk of the operations in hover, rotors are first designed to ensure optimum hover performance, before other aspects of operations such as forward flight and maneuvers are addressed.

Helicopters differ from other flight vehicles in that the rotor provided all of the forces and moments required to operate the vehicle, such as lift, propulsive force, side force, pitching moment and rolling moment. The rotor must be designed so that these forces and moments are generated efficiently (i.e. with the least amount of power) without excessive adverse effects (like blade vibrations and noise). Because helicopters spend much of their operations in hover or slow loitering operations, the rotors must be particularly efficient in these conditions. Since the tip region produces the bulk of the thrust and consumes most of the power, the tip regions must be properly designed.

During early development of helicopters, the blade designs were guided by propeller theory (Glauert [1]) and incorporated taper and twist. As computational tools matured, more advanced blade shapes were explored. Inspired by fixed wing tip design, a swept back tip was innovatively used on Sikorsky S-67 [2]. Because of its great success, other

rotors such as Black Hawk, Apache and S-76 soon followed the idea. In the following years, more exotic tip planforms were followed. A series of rotors were designed and developed by Westland Helicopters under the British Experimental Rotor Program (BERP). In this design, the tip leading edge was moved forward reducing the nose-down pitching moments created at the tip, and a backward sweep was used to reduce and delay the compressibility effects and shock formation. In addition, the notch, as shown in Figure 1 produces a vortex fence, keeping the tip from stalling.

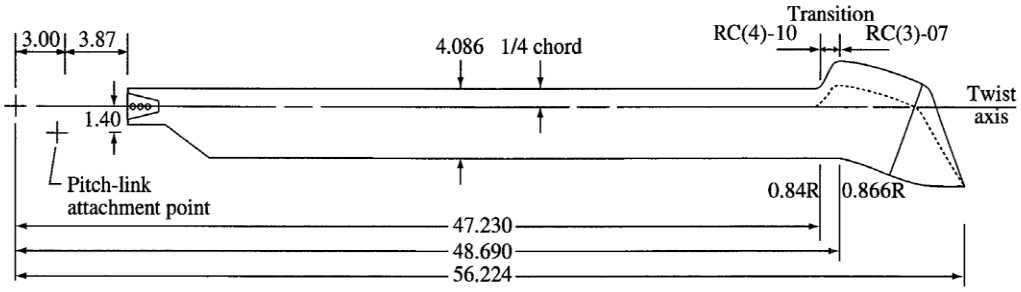

Figure 1 BERP-type rotor blade [3]

Other systematic experimental studies have been conducted about tip effects on rotor aerodynamic performance [4] [5]. One of these studies by Balch focused on the S-76 rotor and demonstrated that anhedral tip gives the best performance in hover compared to other tip planforms [6].

Anhedral has been successfully introduced on different blades since the end of the 1990s, such as BERP blade and S-76 blade, yet the mechanism of how it works on the blade was not completely understood at the time [7] [8] [9]. It was clear that the tip vortex was displaced downwards in the wake by anhedral, but how the displaced vortex position

affects the flow field and the strength of the vortices-blade interaction are still not visualized or quantified [10].

1.2 Motivation and Objectives

This work is motivated by these earlier studies where a series of increasingly complex computational tools were used to analyze and design advanced rotors. Specifically, the present study focuses on an improved understanding of advanced anhedral tips in relation to other conventional tip shapes, such as rectangular and swept-tapered tips.

The primary objectives of the current study are to:

1. Validate the computational methodology for the rotors in hover through comparisons with experimental data.
2. Assess the sensitivity of tip planform effects on the hover and forward flight performance advanced blade tip shapes.
3. Offer a physical explanation of how the blade tip shapes impact rotor performance in hover.

In this subsection, a brief description of the research is given, which includes a description the S-76 blade geometry, the flow conditions simulated in the research and an introduction of the solver applied in the rotor simulations. The objectives of the thesis are listed in the end.

1.3 Organization of the Document

This document is organized as follows. Chapter 2 gives a brief description of the tip geometries considered, and the available test data. Chapter 3 gives a brief introduction of the methodologies, such as meshing topologies and turbulence modeling, required in the CFD simulations. Chapter 4 presents the details of the numerical methodologies employed in the current work. Chapter 5 CHAPTER 4 presents discussions of numerical validations of the two solvers for hover and forward flight conditions. In Chapter 6, the detailed results for different thrust setting and flight conditions of S-76 are shown, and the discussions based on physical analysis are made. Chapter 7 consists of conclusions, suggestions and recommendations for future work.

CHAPTER 2. BLADE GEOMETRY, TEST DATA, AND AIAA HOVER WORKSHOP ACTIVITIES

In this chapter, a brief description of the geometries tested by Balch [6] is given. A summary of available test data is presented. A summary of workshop activities related to this geometry is also given.

2.1 Description of the Blade Geometry

The baseline rotor simulated in the case is a scaled S76 model which is 24% of the Sikorsky production rotor, with sweep and taper. The rectangular tip is a variation of the baseline shape with zero sweep and no taper. The details of the blade geometry are shown in Figure 2 below.

The rotor hub is not considered in the computational domain. As shown in published research [11], the effect of the hub on the S76 rotor performance in hover is negligible when the simulation is under a periodic condition and is not affected by the starting vortex. Table 1 shows the main geometric properties of the baseline tip shape. The blade chord is adjusted for the rectangular shape to maintain the same rotor solidity as the baseline rotor. The anhedral tip is modified by adding 20° of anhedral angle at 95% radial location, while maintain the solidity to be the same as that of the baseline rotor.

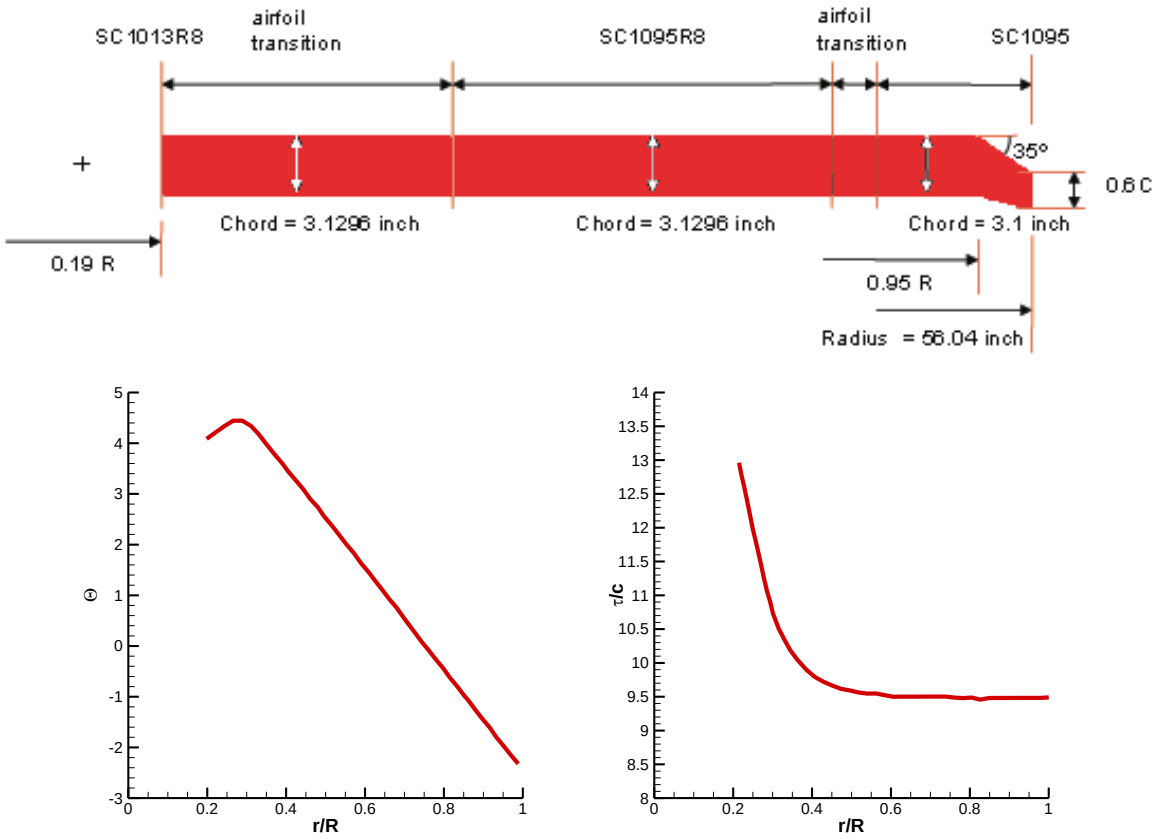

Figure 2 S76 Baseline planform description

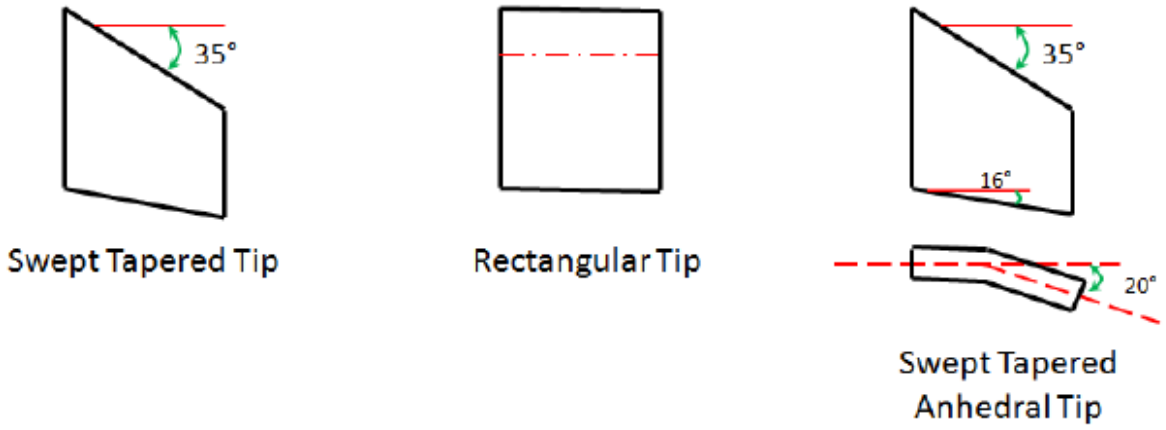

Figure 3 Tip planforms Considered in this Study

Table 1 Blade configuration and dimensions

Number of blades	4
Radius	56.04”
Nominal Chord	3.1”
Equivalent Chord	3.035”
Tip Taper	60% c
Root Cutout	19% R
Sweep (leading-edge)	35 degrees at 95% R
Rotor Solidity	0.07043
Airfoil	SC1013R8, SC1095R8, SC1095
Scale	1/4.71
Twist	-10° linear twist
Rotor rotational tip Mach number	0.65

2.2 Description of the Experiment

The tests results compared in this study for the hover condition were conducted in the Sikorsky Model Hover Test Facility using the Basic Model Test Rig. This test facility includes the hover pad, the model assembly area and the data acquisition and processing systems. It is a self-contained helicopter test rig which can handle a range of rotor system and model support schemes. The test model is a $1/1.471$ scaled model of the real rotor blades. The blades were tested with five different tips. In addition to the tip planform shown in [12], there are other two tip planforms that were considered: $20°$ swept only and $60°$ tapered only. The five tips were tested at a range of tip Mach numbers and thrust settings.

The data compared with the forward flight simulations comes from a full-scale helicopter rotor test which was conducted in the NASA Ames 40ft by 80ft Wind Tunnel with a four bladed S-76 rotor system [13]. Four blade tip planforms were investigated

swept/tapered, swept, tapered, and rectangular. The wind tunnel wall correction was estimated by an incremental change in the angle-of-attack which is proportional to the rotor lift: $\Delta\alpha = K(\frac{L}{q})$, where $K = 0.00197$ deg/ft^2. By adding this angle increment to the uncorrected, geometric rotor shaft angle α_u, the corrected angle-of-attack of the rotor disk in free air: $\alpha_c = \alpha_u + \Delta\alpha$ is obtained. The measured forces and moments, after accounting for the tare correction, were resolved into this new wind-axis system. This wall correction is based on conventional fixed wing techniques, for a wing of span equal to the rotor diameter [14]. It should be noted that the reported values of θ_{1s} in the experiments were in measured in the control plane, with the angle-of-attack $\alpha_{con} = \alpha_c - \theta_{1s}$, where α_c is a function of lift of the rotor. In the present study, additional trimming is needed to match the measured thrust values.

2.3 AIAA Hover Workshop Activities

Under the charter of the AIAA Applied Aerodynamics Technical Committee, a number of researchers, including the present author, have assembled a Rotorcraft Simulation Working Group with the immediate purpose of assessing current state-of-the-art in hover prediction methodology, determining critical challenges in consistently and accurately predicting hover performance, and serving as leading catalyst in the development of computational methods for solving rotorcraft problems [15] [16] [17] [18] [19].

There were several challenges in setting up a common rotor-in-hover test case to enable a workshop and share hover performance predictions from the participants [20] [21]. These included obtaining a publicly available realistic geometry with reliable force

balance, surface pressure tap, and PIV data, and complications due to blade aero-elastic deformations. The team discussed several candidate existing benchmark cases including the UH60A model rotor [22], HART rotor, Comanche rotor, and S-76 [23]. It was concluded that the S-76, because of its linear twist, and somewhat publicly available section geometry, and planforms, was the best candidate for a systematic evaluation of the capabilities and gaps of current generation of codes. For these comparisons, the effect of aeroelastic deformation was not considered. The baseline S-76 blade geometry, with built-in aeroelastic deformations for a representative loading configuration was provided to all potential participants.

An invited session was organized at the AIAA SciTech 2014 Conference. This session was limited to the baseline S-76 computations, with tip-shape effects deferred for future workshops. The participants included Georgia Tech in collaboration with Sikorsky, Boeing Helicopters [24] [25] [26] [27], University of Maryland, University of Toledo, US Army AeroFlightDynamics Directorate, University of Liverpool, and KAIST [28] [29].

A refined surface grid with 291 axial and 98 radial grid points was generated and provided to all the participants through the APA Rotor Simulation Working Group share-point site. The volume gridding strategy was entirely left to the user's discretion – to take advantage of all beneficial features of the solvers (e.g. overset mesh, adaptive grids, and unstructured grids).

The model provided had a blunt open tip. If users wished to close the tip with a rounded surface, the following procedure was prescribed: Chop off 1/2 maximum t/c (which is 9.5%) of the tip airfoil from the blade 2. Revolve the upper and lower points of

the airfoil about each midpoint of the section to produce a tip cap surface. In the present work, the blunt open tip was used.

To allow for direct comparison with other's results and to determine how well the various approaches capture the general trends, the participants conducted a collective sweep by increments of 1 degree [30]. The following results were obtained, and supplied in graphical form and tabular form:

(i) Plots of C_T and C_Q versus collective pitch were provided, along with tables of C_Q versus C_T, and Figure of merit versus C_T [31].

(ii) Blade loading distributions, section thrust and torque coefficients, as a function of radial position r/R were collected and compared.

(iii) Pressure distributions as sectional chordwise plots of C_p versus x/c were collected and compared at the following radial stations (r/R): 0.20, 0.40, 0.60, 0.70, 0.75, 0.80, 0.85, 0.90, 0.925, 0.95, 0.975, and 0.99 were provided and compared.

(iv) Tip vortex trajectory plots as a function of wake age were compared [32].

The workshop activities continue at this writing, with focus on these areas:

- Focus on solution convergence and what constitutes a converged hover solution [33] [34]
- Expanding standardized post-processing for flow visualization across all solutions [35] [36] [37]
- Comparative predictions on the effects of high thrust conditions
- Vortex wake breakdown in high fidelity simulations [38]

- Investigation of aero-elastic twist windup
- Investigation of the 4/rev signal history in time-dependent solutions [39]
- Complete the three tips shapes and Mach number conditions [40] [41] [42] [43] [44]
- Investigate peak bound circulation strength vs. tip vortex strength [45] [46]
- Quantify first tip vortex passage radial and axial miss distance with respect to the local blade ¼ chord line (r/R & z/R) [47]
- Investigate transition modeling and turbulence modeling effects [48] [49] [50] [51] [52]
- Perform grid resolution studies, near field and far field [53] [54] [55] [56]
- Perform temporal accuracy studies [57] [58]
- Investigate higher order schemes [59]
- Investigate steady state vs unsteady simulations
- Investigate near-body/far-body grid adaption
- Perform validation studies with other relevant data sets [60] [61]
- Investigate effects of far field boundary conditions/ and/or extent
- Investigate installations effects
- Study impact of different hub geometry approximations
- Incorporate structural mode

CHAPTER 3. LITERATURE SURVEY

In this chapter, we briefly review the evolution of rotor design, and computational techniques that enabled these developments. For a more comprehensive review of rotor design, the reader is referred to an article by Brocklehurst et al [62].

3.1 First Generation Analyses and Designs

The first generation rotor designs have their roots in propeller theory, commonly known as the combined blade element-momentum (BEM) theory [63]. In this theory, the rotor disk is divided into concentric rings of width Δr as shown in Figure 1 below. The area of the ring is $\Delta A = 2\pi r \Delta r$. The mass flow rate through this annulus ring is $\rho(V+v)A$ where ρ is the freestream density, V is the forward velocity of the propeller (or axial velocity of the helicopter rotor in climb), and v is the induced velocity at the rotor disk.

According to momentum theory, the change in the axial velocity between a station far upstream of the propeller (or far above the rotor), and far downstream (or far below, in the case of a helicopter rotor) may be shown to be 2v. Thus the rate of change of momentum of the fluid that flows through this annulus ring may be computed as:

$$\Delta T = \rho(V + v)\,\Delta A\,(2v) = 4\pi r\rho\,(V + v)\Delta r \qquad (1)$$

This change in momentum is caused by the axial force ΔT exerted by the blade sections (or blade elements) on the fluid.

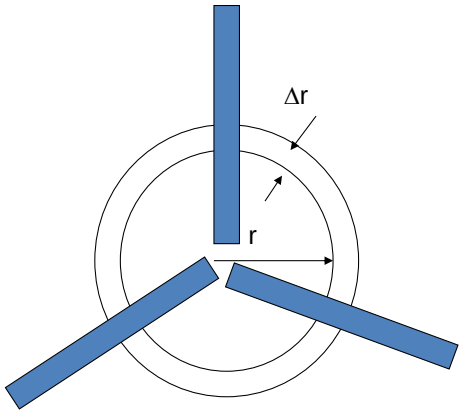

Figure 4 Annulus ring of width Δr

We may also look at this axial force from a blade element theory perspective. There are 'b' blades. The local chord of each blade is c(r). Thus the blade area intercepted by the annulus, as shown in Figure 4, is $Bc\Delta r$. Let the local blade sectional lift coefficient be C_l. The local dynamic pressure is given approximately as $\frac{1}{2}\rho\ (\Omega r)^2$. Assuming that the lift force predominantly occurs in a direction normal to the rotor disk, we can express ΔT from a blade element theory perspective as

$$\Delta T = \tfrac{1}{2}\ \rho\ (\Omega r)^2\ bc\ C_\ell\ \Delta r \qquad (2)$$

Equating Equations 1 and 2, we get an expression for the induced velocity v in hover (V=0):

$$4\pi r v = \tfrac{1}{2}(\Omega r)^2\ bc\ C_\ell \qquad (3)$$

From momentum theory, the induced power is minimum of the inflow v is constant all across the rotor disk. If we assume that the blade sections are operating at a constant coefficient, it is evident that the chord would vary inversely with r.

$$c(r)= 8\pi v/(b\, C_{\ell}\, \Omega^2 r) \qquad (4)$$

Equation 4 indicates that the local chord in the tip region must be smaller compared to chord near the root region, i.e. the rotor must be nonlinearly tapered. For manufacturing reasons, and for improved performance in other regimes of flight (e.g. forward flight), designers have only used untapered rotors, or employed rotors with a small amount of taper only in the tip regions as shown in Figure 5.

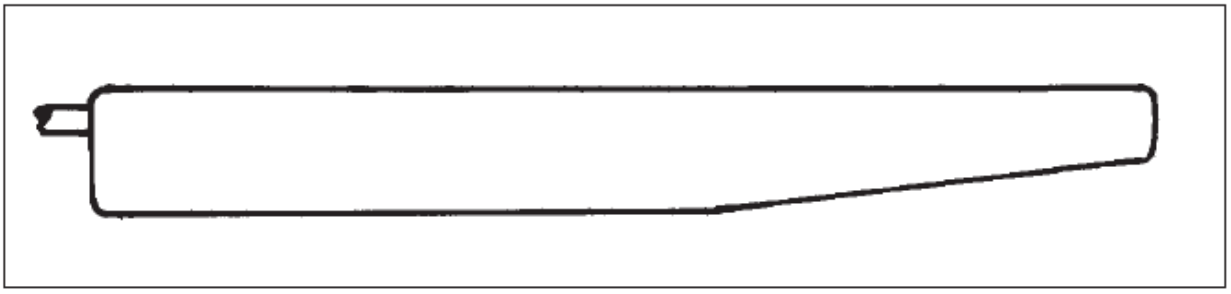

Figure 5 Tapered Rotor Planform used in Sikorsky Rotor R4

The blade element-momentum theory also gives indication on how the rotor must be twisted. For a constant "optimum" lift coefficient over all sections of the rotor blade, i.e. for the lift coefficient that maximizes lift to drag C_{ℓ}/C_{d} ratio, it follows that the angle of attack must be constant as well. Thus, the local section angle θ (sum of blade collective pitch and twist) relative to the plane of rotation should vary as

$$\alpha = \theta - \arctan[(V+v)/(\Omega r)] \quad (5)$$

Such a highly nonlinear pitch variation is employed only in propellers in axial flight and in axial turbines. For helicopter rotors, such a large twist variation will cause the blade to stall at the root, and lead to increased fluctuations in air loads and resultant structural vibrations. Therefore, helicopter rotors have a linear twist. All of these guidelines for taper and twist may be gleaned from the very simple, and physically intuitive, blade element-momentum theory.

The analytical estimates for the induced velocity shown above work well only for lightly loaded rotors. For highly loaded rotors, it is necessary to compute the induced velocity from Biot Savart law, assuming a prescribed tip vortex geometry [64, 65], or a "free wake" [66] [67] which moves at the local flow velocity. The vortex strength may be assumed to be the peak bound circulation in a single tip vortex model. For more accurate results, a multiple trailer vortex model that includes the inner wake is used. In this approach, the strength of each of the "trailer vortices" is computed from the change in the bound circulation. Many of the rotors from the post-Vietnam era such as the UH-60A Black Hawk [68] and the Apache AH-64A rotor, and related civilian helicopters during the 1970s and the 1980s.

3.2 Second Generation Rotor Analyses and Designs

As the need for higher forward speeds arose, researchers and designers had to develop techniques for modeling transonic flow effects in the rotor tip regions. Cole and Murman were the first to solve 2-D transonic flow using small disturbance theory for lifting

and non-lifting airfoils [69]. Caradonna and Isom soon extended this technique to three dimensions and modeled lifting helicopter rotors [70]. This theory was used to assess the effects of sweep and taper on transonic flow around conventional advanced blade tips [71] [72] as shown in Figure 6. The pressure distribution over the blades were used to computing loading noise and shock noise. As a result, highly efficient blade tip shapes that were also quite in hover and forward flight emerged.

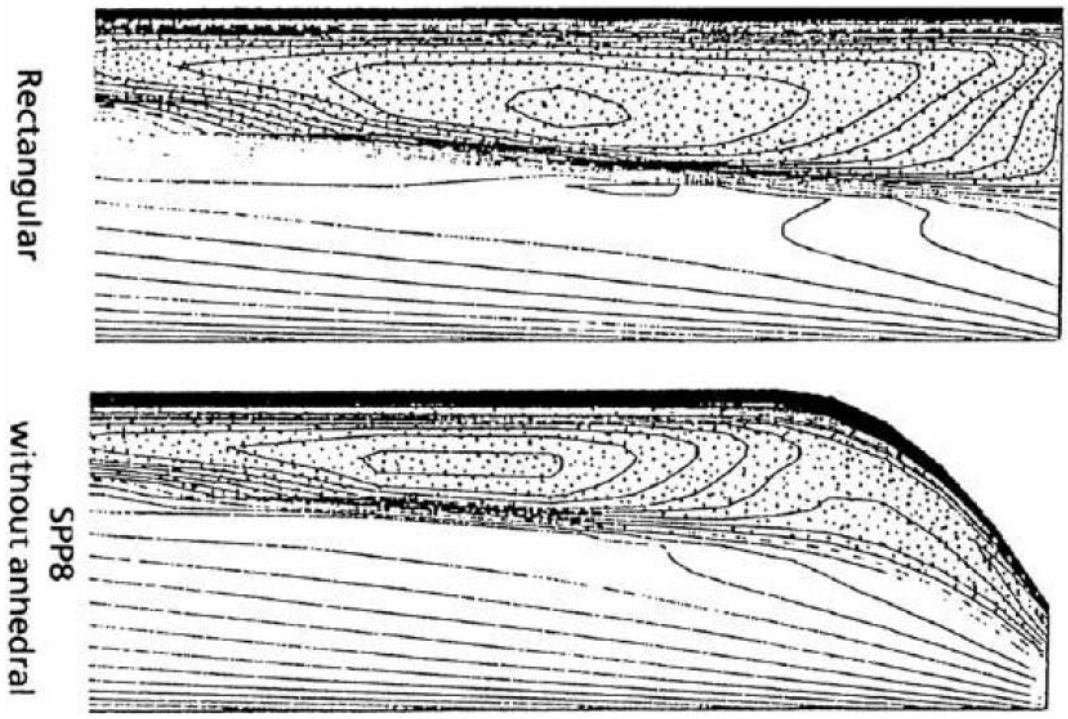

Figure 6 Pressure field over rectangular and parabolic tip shaped blades at fixed C_T/σ

Because these theories were by themselves unable to capture the helical tip vortex structures and the associated inflow, an improved estimate of inflow velocity was needed.

Tung, Caradonna, and Johnson were the first researchers to successfully link the induced inflow from free wake analyses to transonic potential flow analyses [73]. These authors also incorporated elastic deformations experienced by the blade as corrections to the blade section angle of attack. Other researchers developed more advance transonic full potential analyses for helicopter rotors [74] [75]. These methods were also coupled to inflow from free wake analyses and structural such as those found in the comprehensive rotor codes.

3.3 Third Generation Analyses and Tools

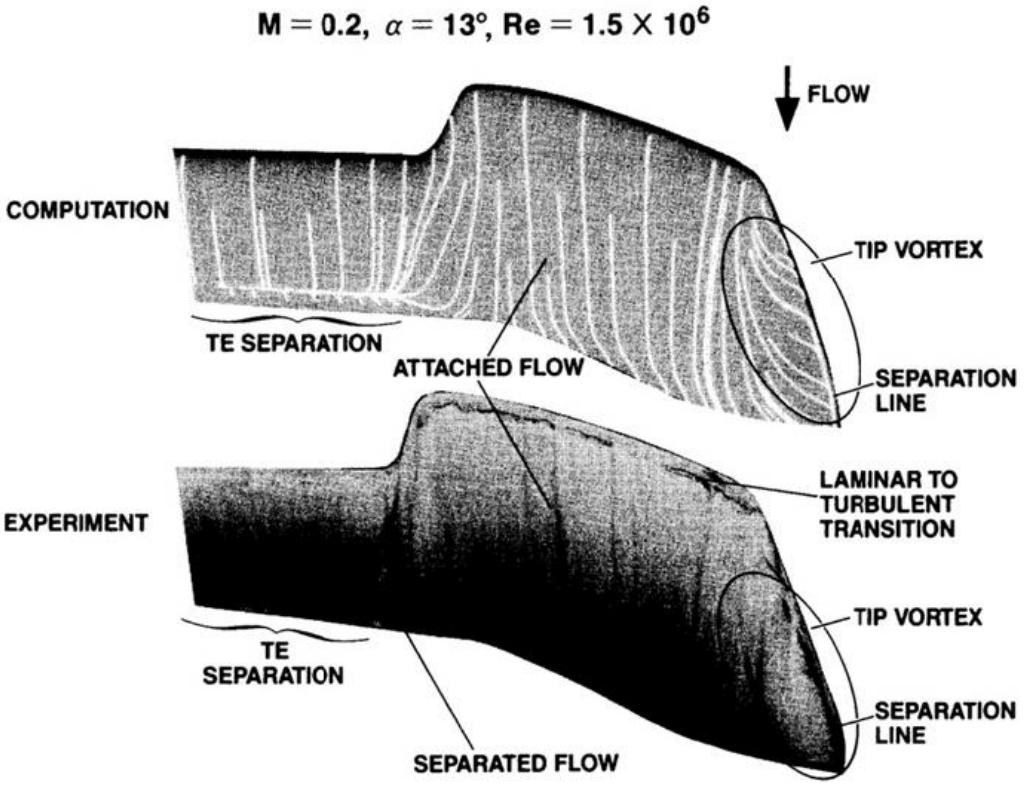

Figure 7 Viscous flow over the advanced British experimental rotor tip (BERP) in hover

As computational power increased, and as algorithms for solving the Euler and Navier-Stokes equations on curvilinear body fitted grids became available [76] [77], these

approaches were quickly adapted for inviscid and viscous flow over helicopter rotors [78] [79] [80] [81] [82]. Duque applied these techniques to successfully model rotor flow over an advanced British Experimental Rotor Tip (BERP) in hover [83] as shown in Figure 7.

More advanced planforms [84] are shown Figure 8. These studies demonstrated that flow over the BERP tip remains attached even in high speed forward flight. Experimental and computational studies were also used to modify the blade twist and minimize the induced power in hover. Additional studies of the BERP tips are given by Perry [85] and Harrison et al [86].

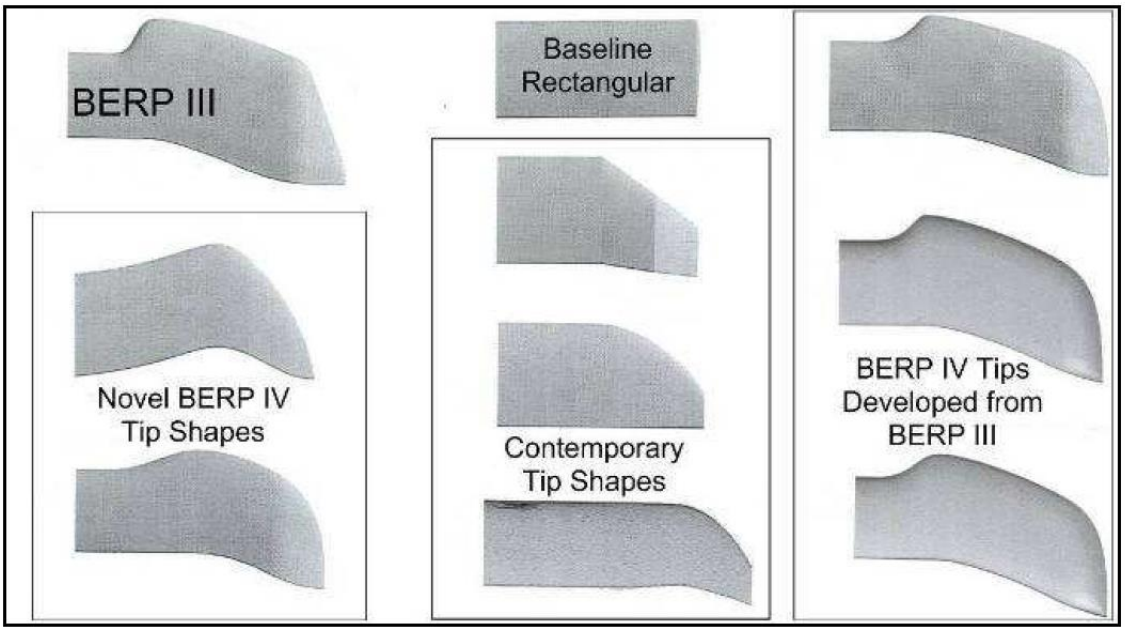

Figure 8 Various BERP planforms analyzed computationally and experimentally during the BERP development program

Wake capturing Navier-Stokes methods quickly followed [87].Results from these methods for the UH60 model rotor show good agreement with experiments at moderate thrust conditions. Comparison of results between the UH-60A rotor and the BRERP rotor

with equivalent tip dynamic pressure indicates that the BERP blade, with an unconventional planform, gives more thrust at the cost of more power and a reduced Figure of Merit. Under high thrust conditions considered, severe shock-induced flow separation was observed for the UH60 blade, while the BERP blade developed more thrust and minimal separation. The BERP blade also produced a tighter tip vortex compared with the UH60 blade.

CHAPTER 4. NUMERICAL VALIDATION AND MESH SENSITIVITY STUDIES

The S-76 simulation results and comparisons with the experimental data are shown in this section with a brief description of the mesh and boundary conditions for the two solvers, GT-Hybrid and STAR-CCM+, discussed in the previous chapter. The parameters of interests for the comparisons are pressure distributions, integrated force and moments, wake trajectory and the rotor figure of merit.

4.1 Mesh Density Sensitivity Analysis

Because the wake structure, in particular the wake structure determined by the wake capturing model employed in STAR-CCM+, is sensitive to grid density due to the inherent diffusion present in the scheme, a number of grid sensitivity studies were conducted using both the solvers to ensure that the computed performance characteristics are independent of the type of the grid.

4.1.1 GT-Hybrid Grid Sensitivity Studies

Two different grid densities are chosen to investigate its effects on hover performance for the S-76 rotor swept-tapered planform (baseline in the thesis). A cross-section of the volume grid used in the simulations is shown in Figure 9. The fine grid consists of 291 points in the wrap-around direction, 98 radial grid points on the blade, and 45 points in the normal direction. The coarse C-H grid consists of 131 points in the wrap-around direction, 70 radial grid points on the blade, and 45 points in the normal direction. An in-house grid algebraic generator was used to generate these grids.

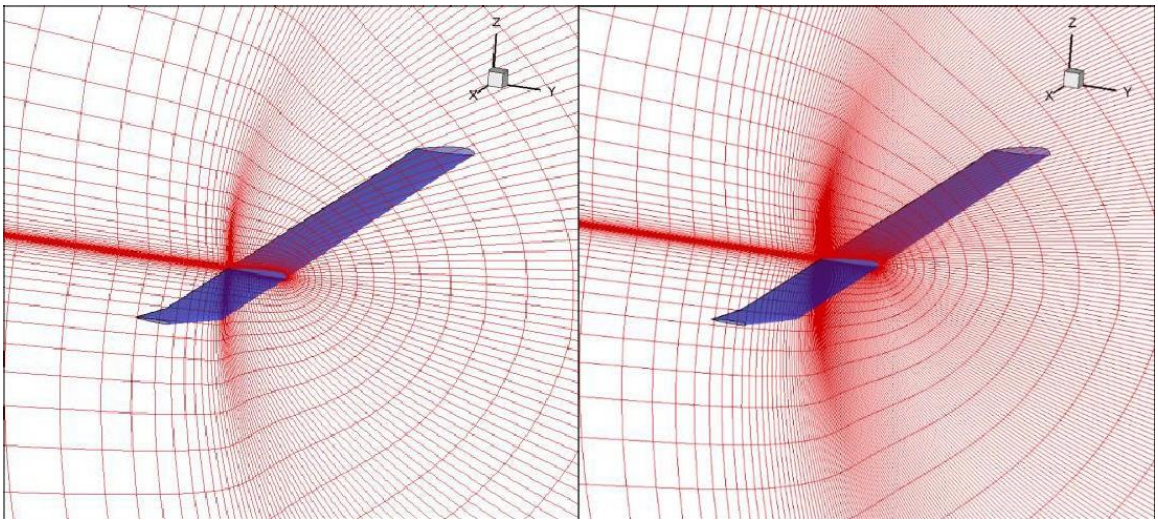

Figure 9 Coarse Grid (131 × 70 × 45) and fine grid (291 × 98 × 45) used in GT-Hybrid (The numbers denote the number of grids points in chord wise, span wise and out wise respectively) [88]

For solutions presented in this work, the Roe upwind, third order accuracy scheme with the $k-\omega$ turbulence model is used. Figure 10 shows the effects of grid density on integrated hover performance parameters such as thrust coefficient C_T, torque coefficient C_Q as well as the figure of merit FM.

The figure of merit (FM) is defined as the ratio of ideal power to the required power, expressed as $\frac{1}{\sqrt{2}}\frac{C_T^{3/2}}{C_q}$. Slight differences between the coarse and fine grid are seen in the prediction of thrust coefficients. The predicted torque starts to deviate from that computed with a fine mesh as the collective pitch angle increases. As may be expected, the refined mesh CFD results are closer to measurements, presumably due to the smaller discretization errors, and lower numerical diffusion created by the mesh.

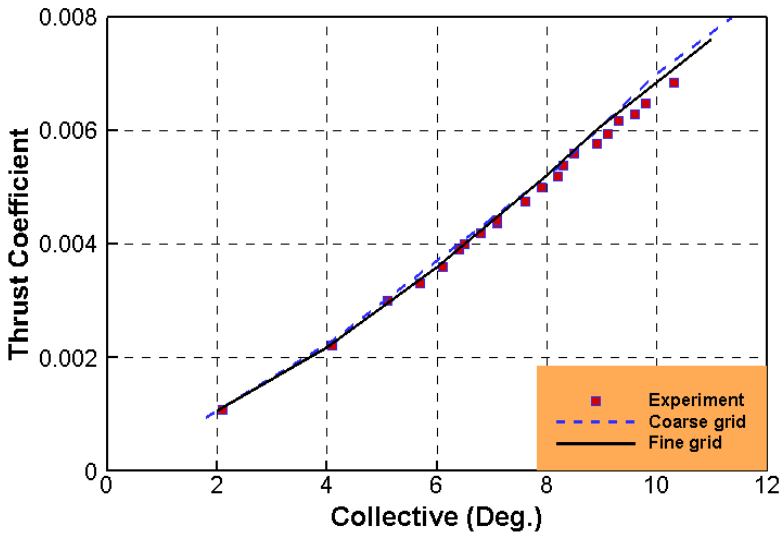

(a) Thrust coefficient vs collective pitch

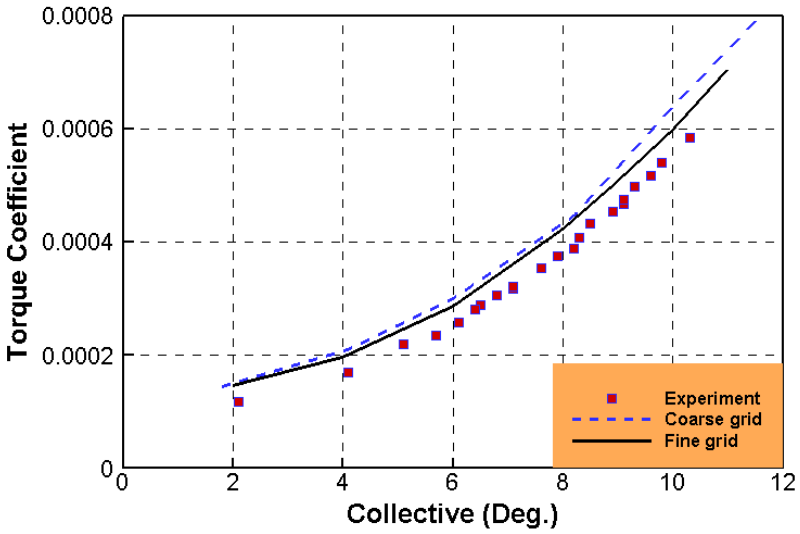

(b) Torque coefficient vs collective pitch

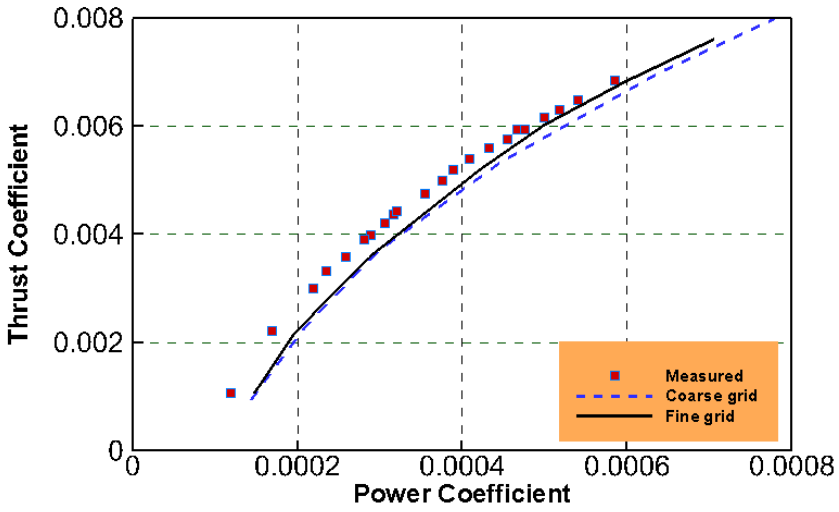

(c) Thrust coefficient vs power coefficient

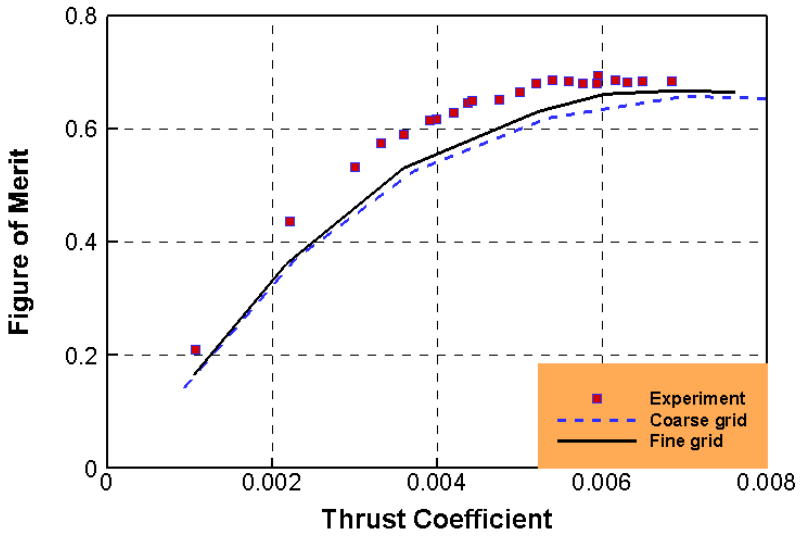

(d) Figure of merit vs thrust coefficient

Figure 10 Performance characteristics (GT-Hybrid) [88]

Both grids captured C_T/σ value of 0.09 well at a collective pitch angle of 9.5°. At this collective pitch angle, tip vortex descent rate and contraction rate between two grids

are compared, as shown in Figure 11. The tip vortex descent rates are nearly the same, however, there is a slight difference for the contraction rate after 180 degrees of vortex age.

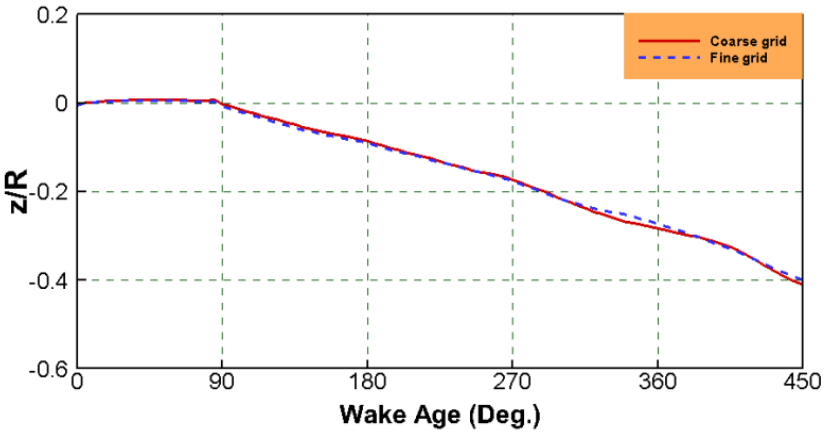

(a) Tip Vortex Descent Rate

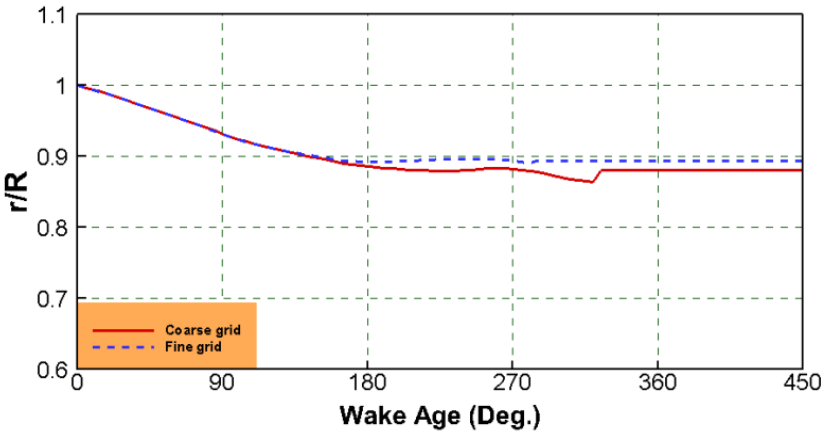

(b) Tip Vortex Contraction Rate

Figure 11 Effects of near field grid on the tip vortex descent rate and contraction rate

From the comparisons above, it is shown that the mesh refinement has a slight nut noticeable effect on the converged solutions, and in particular on the torque coefficient C_Q and the figure of merit. It was concluded that the refined mesh is adequate for the entire

thrust sweep. Therefore, the refined mesh with 291 × 98 × 45 cells have been used for further simulations.

4.1.2 STAR-CCM+ Grid Sensitivity Studies

Because the computational time required by STAR-CCM+ solver is 10 times of that required by GT-Hybrid, only a limited grid refinement study was attempted at a single collective pitch of $\theta_0 = 9.3°$. Two grids with 15 Million grid points and 32 million grid points were considered. The results are shown in Table 2.

Table 2 Effects of Mesh Sensitivity on Performance Predictions

Case #	θ_0 **(degree)**	C_T	C_q	**FM**
Mesh 15M cells	9.3	6.153e-03	5.253e-04	0.650
Mesh 22M cells	9.3	6.182e-03	5.230e-04	0.657
Experiment	9.3	6.180e-03	4.991e-04	0.688

As shown in Table 2, the difference between solutions obtained from coarser mesh and finer mesh is roughly 1% for FM. Other quantities (radial distribution of thrust and torque) and wake structures showed very slight differences. In this work, the 22 M grid was used for all further studies.

Another parameter of interest in this study is the wake trajectory. The vortex core radius, or alternatively the radius of the iso-surface by Q-criterion, is sensitive to the numerical diffusion created by the spatial discretization. In order to ensure that a given mesh is applicable for further simulations, a mesh density analysis with respect to the positions of shed tip vortex needs to be conducted. The wake trajectory comparisons of

STAR-CCM+ solvers with two mesh densities are studied, and the results of computed iso-surface of Q–criterion (which represents the size of the shed vortex) are shown in Figure 12.

In addition, a vorticity confinement model has been used, that reduces the non-physical vortex core diffusion by introducing a force term to the momentum equations. This force term goes to zero as the grid is refined, restoring the original Navier-Stokes equations. According to previous CFD results by other researchers, and our own in-house studies, use of a vorticity confinement model does not change the integrated force but improves the accuracy of the wake trajectory by reducing artificial numerical diffusion of the tip vortex structures [89] [90].

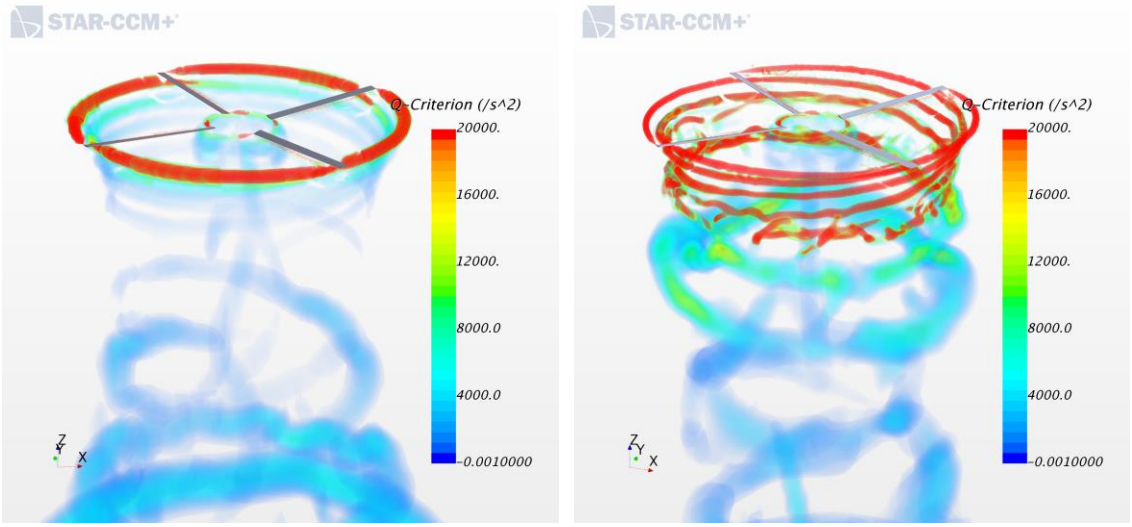

(a) Mesh contains 15 million cells (b) Mesh contains 22 million cells

Figure 12 Wake trajectory comparisons of simulations with different mesh densities

4.2 Comparison of Results and Validation

In additional to the mesh density analysis conducted in the previous section, results from the hybrid solver and the full wake capturing solver employed in STAR-CCM+ have also been compared with the solutions obtained by other researchers.

4.2.1 Mesh Description

The surface mesh for both GT-Hybrid and STAR-CCM+ is extruded from the airfoils specified at selected radial locations of 18.9%, 26.5%, 40%, 75%, 80%, 84%, 95% and 100% radius of blade. These airfoils have a blunt trailing edge. The trailing edge of the airfoil sections have been modified to achieve a sharp trailing edge as shown in Figure 13. The unstructured surface mesh employed in STAR-CCM+ is shown in Figure 14, along with region refinement at the leading, trailing edges and the tip region. In order to account for collective pitch, the blade surface mesh was rotated by the collective pitch angle of θ_0. The pre-cone angle is set to be 3.5° for all the cases in hover, to match the test data.

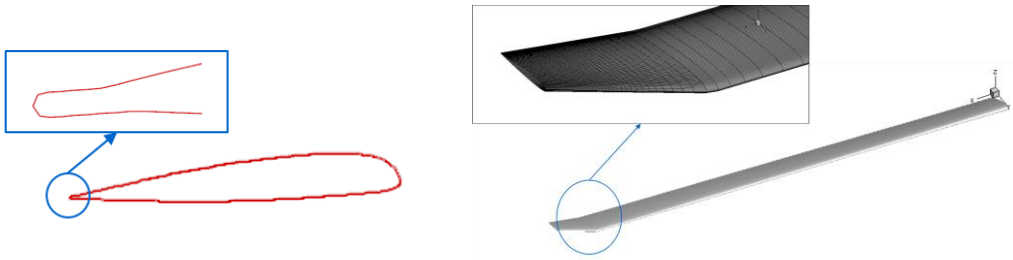

Figure 13 Surface grid used in GT-Hybrid

The volume meshes used in GT-Hybrid are structured meshes generated using an in-house grid generator, which extrudes the structured surface mesh to a 3D C block mesh as shown in Figure 9. The blade form and the airfoil coordinates are specified as part of the input stream. Any parametric change to the blade geometry (e.g. the sweep) will have to be done external to the grid generator. The overset mesh used in STAR-CCM+ is created within STAR-CCM+ package through a pipelined meshing process. This process allows for parametric changes to the rotor geometries.

The simulations performed using STAR-CCM+ utilizes an overset mesh approach. The stationary background grid is comprised of a single cylindrical block with trimmed hexahedral unstructured elements. The background grid extends 10 radii above, 20 radii below and 5 radii in the radial direction. Volumetric refinement regions are in place to capture the vortex structures in the vicinity of the rotor. Each rotor blade is enclosed within a cylindrical overset mesh. The near body grid consists of unstructured, trimmed, hexahedral elements which are able to accommodate blades of complex shapes. The near-body grid is refined at the leading edge, trailing edge and the tip regions using localized volumetric refinement regions in order to resolve the tip vortices. Figure 14 depicts the background stationary grid and the near-body overset grids. The near-body grids sweep through the stationary background mesh and interpolations are performed at the overset interface using the distance linear interpolation method. The coupling between the background and the overset cells is fully implicit.

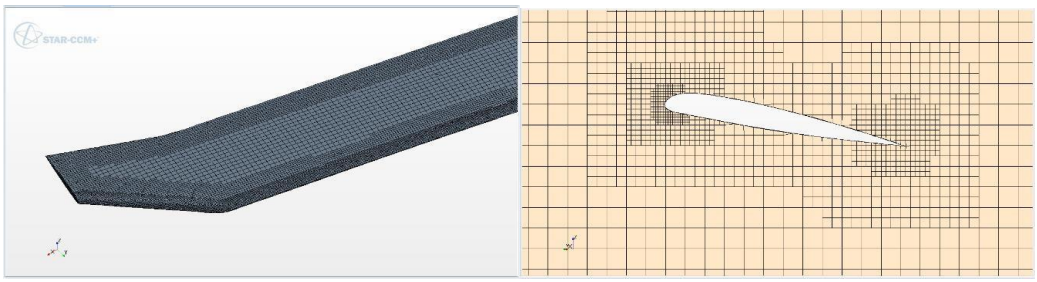

(a) Blade surface grid (b) Cross-section of near-body grid

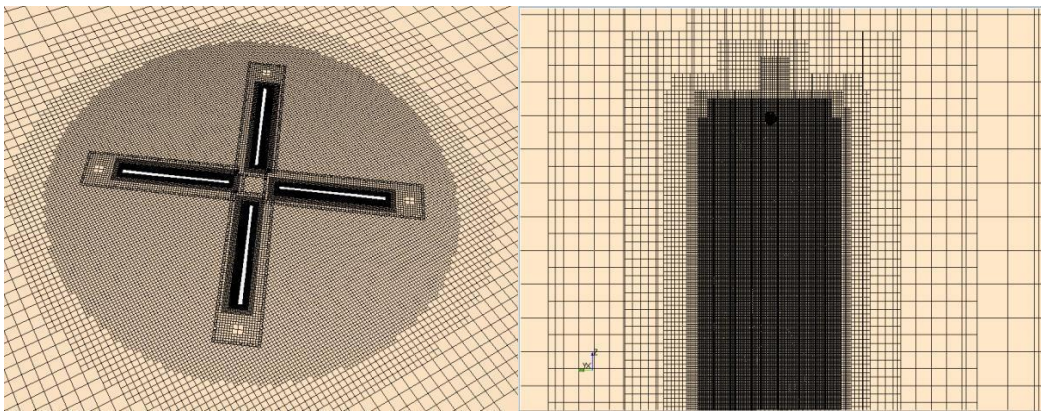

(c) Overview of overset grids (d) Cross-section of back ground field grid

Figure 14 Surface and cross section of volume grid in STAR-CCM+

The trimmed mesher within STAR-CCM+ is able to utilize volumetric refinement zones to refine the mesh in the wake region as well as use mesh elements conservatively in far- field regions. The near body grids (with a y^+ value of 1 normal to the surface) allow $k-\omega$ SST model to capture the boundary layer in fine detail. The computational cells used in the background mesh were 4 million, while each of the 4 overset regions used 4.5 million cells. The total number of computational cells used were 22 million. A sample rendering

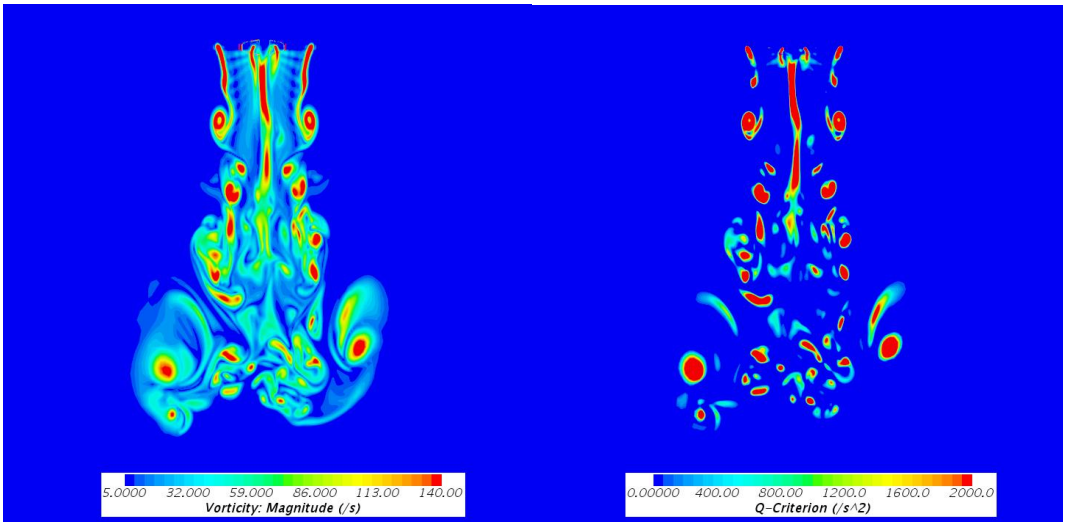

Figure 15 Vorticity and Q-criterion distribution of baseline at C_T/σ = 0.09

of the tip vortex structure for the swept-tapered rotor at C_T/σ of 0.09 is shown in Figure 15. The wake structure and the starting vortex are well captured in the plot.

4.2.2 Integrated Load Comparisons with Other Solvers

Comparisons of GT-Hybrid results with several other Navier-Stokes solvers are shown in Figure 16. For the variation of C_T with the collective pitch angle, it is seen that all the computed data are in good agreement with each other and the experimental data. At higher pitch settings, GT-Hybrid has a tendency to slightly over predict the thrust coefficient, and STAR-CCM+ captures the experimental results better.

The other results shown on Figure 16 are from participants in an AIAA Hover Workshop. There has not been any attempt to among users to use comparable grids, identical turbulence models or similar scheme with the same order of accuracies. As a consequence, the calculations do show some differences between different methodologies.

Table 3 Mesh and solver descriptions of other solvers compared in the study

	OVERFLOW [91]	OVERTURN [92]	Helios (Boeing) [93]	TURNS [94]
# Grid Points	63.4M	-	400M	0.2 M
Scheme Accuracy	2nd order near the blade 5th order in the off-body 2nd order in time	3rd order MUSCL in space 2nd order backward in time	2nd order in space 2nd order in time	3rd order Upwind Scheme
Turbulence Model	Spalart Allmaras model	Baldwin and Lomax, Spalart-Allmaras, or K-ω SST model	Spalart-Allmaras model	Spalart Allmaras model
Wall-clock time (single case on different computers)	117 Hour/240 cores	-	-	5-6 hours/ 1 core

The solvers and grid used in different research are shown in Table 3.Keeping these differences in mind, it is seen that GT-Hybrid and STAR-CCM+ tend to over predict the torque coefficients. The other analyses (Helios, OVERTURNS simulations done at University of Maryland, and the simulations done at KAIST) give very favorable agreement with test data.

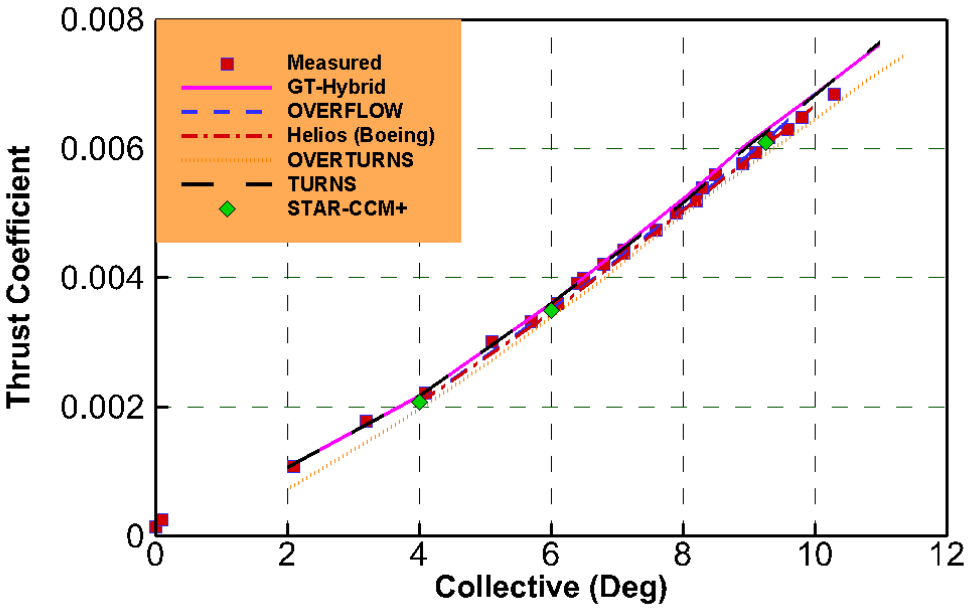

(a) Thrust coefficients vs. collective pitching angle

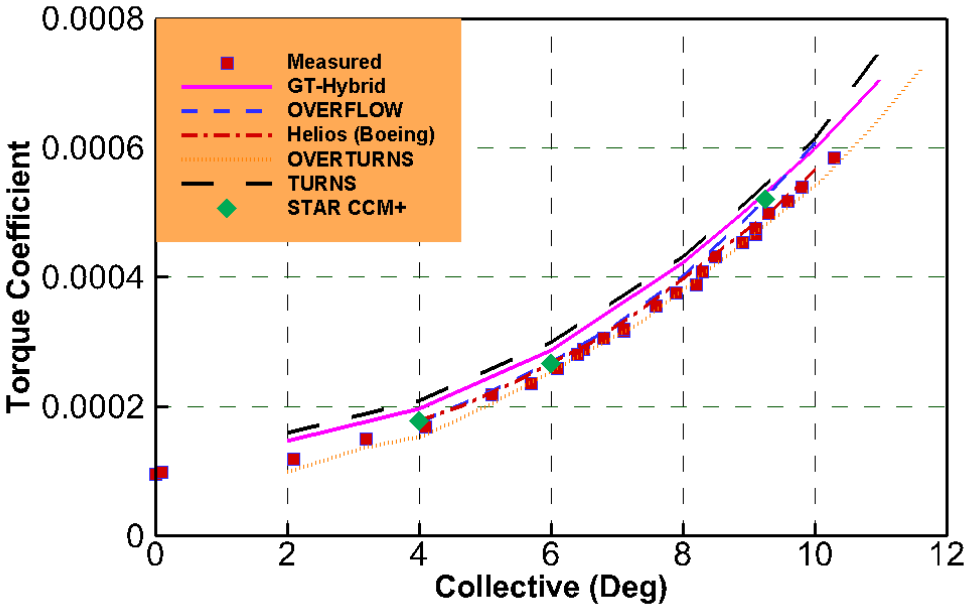

(a) Power coefficients vs. collective pitching angle

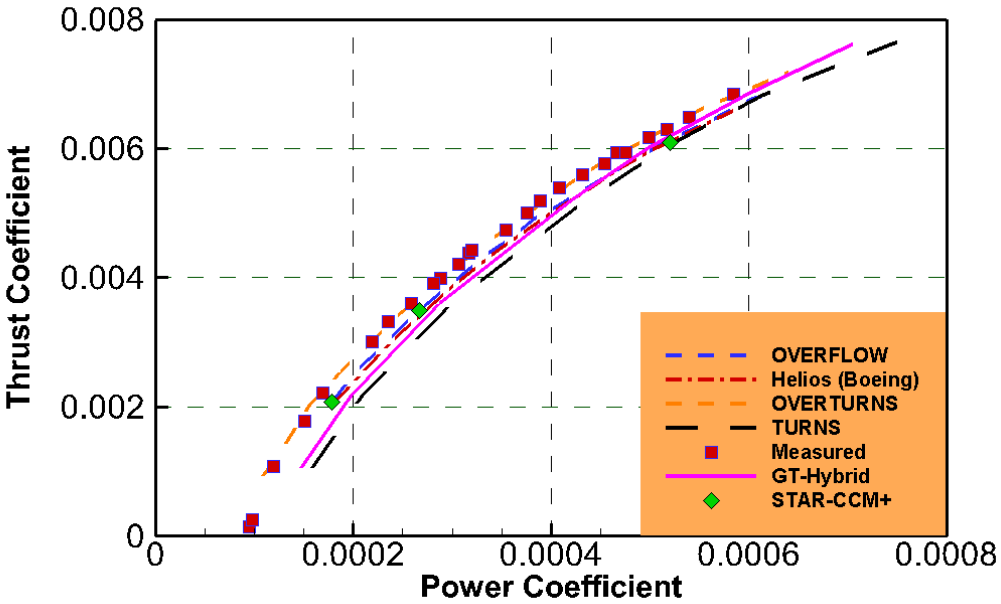

(a) Thrust coefficients vs. power coefficients

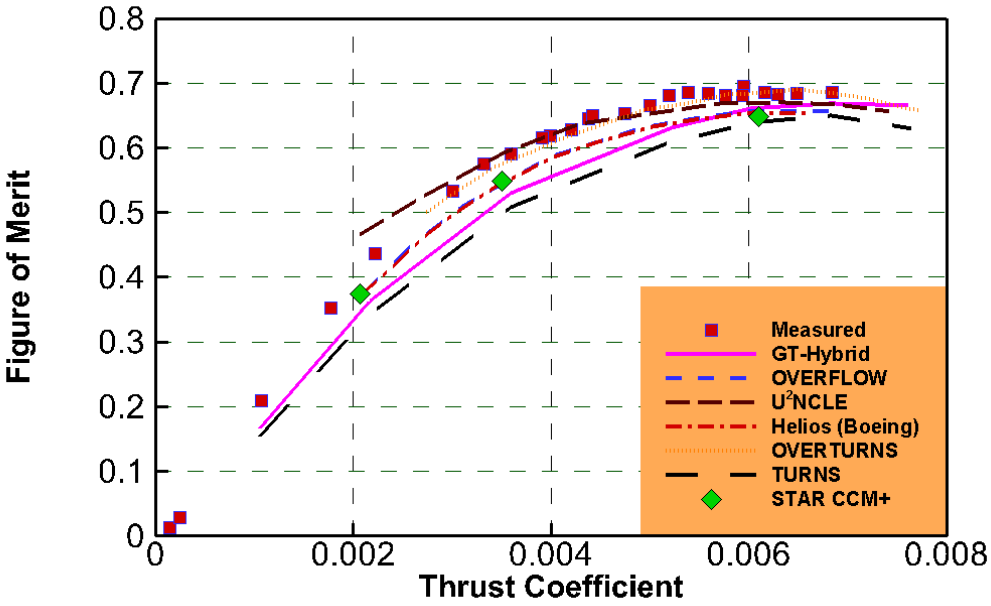

(a) Figure of merit vs. thrust coefficients

Figure 16 Hover performance characteristics of the baseline planform

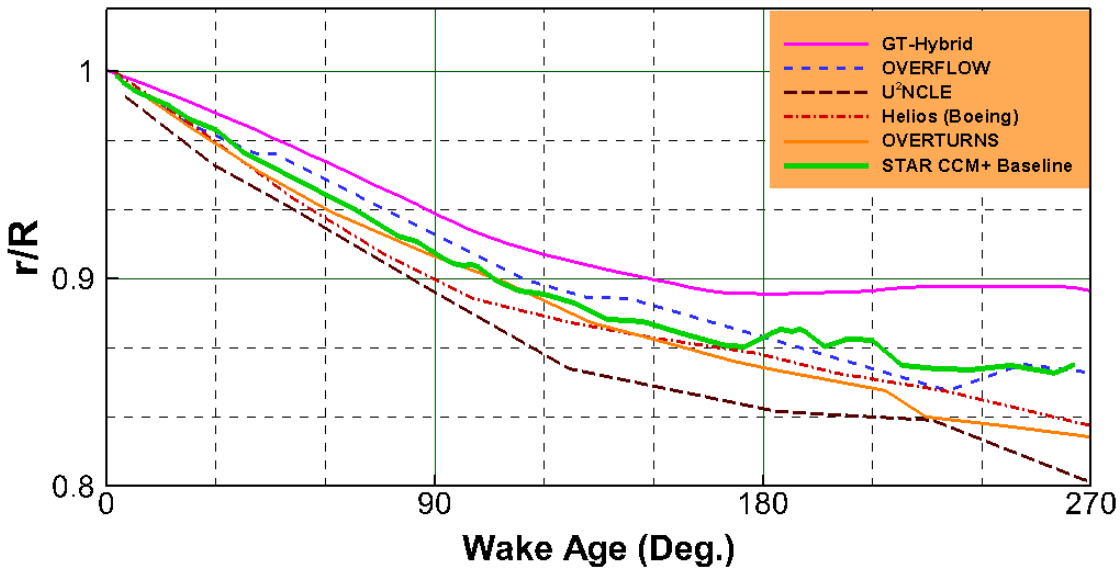

(a) Tip Vortex Descent Rate

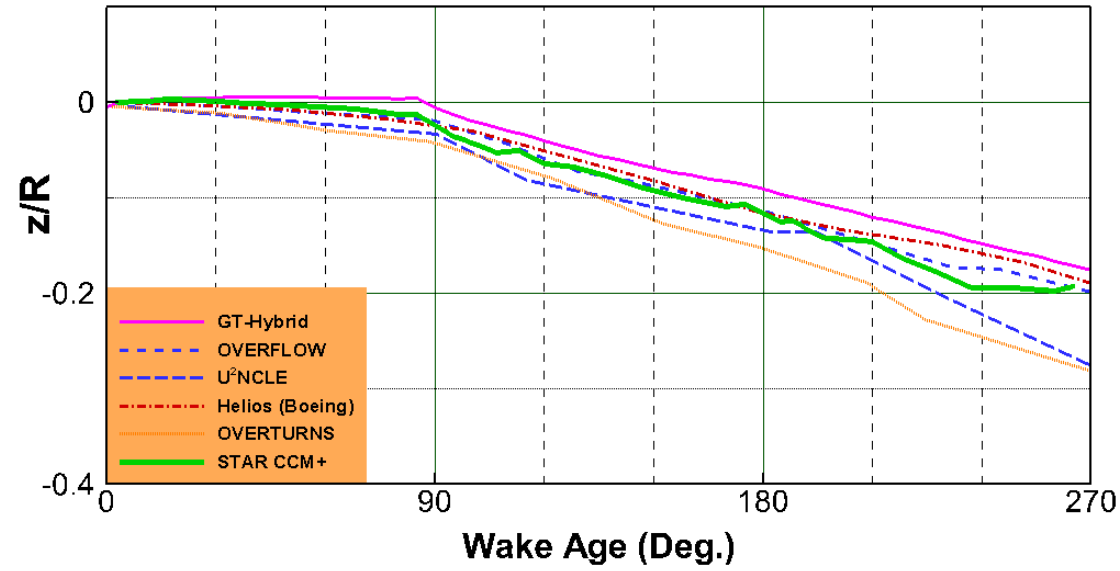

(b) Tip Vortex Contraction Rate

Figure 17 Computed Tip Vortex descent rate and Contraction Rate for Baseline case ($C_T/\sigma = 0.09$)

4.2.3 Wake Comparisons

Figure 17 shows the tip vortex descent and contraction rate for the baseline at $C_T = 0.09$ predicted by different solvers with respect to the vortex age from 0° to 270°. Because the hover performance is strongly influenced by rotor inflow, which is in turn determined by the tip vortex trajectory, tip vortex geometry and strength are important parameters in rotor CFD validations. As there is no test data available for the present cases, only the comparisons between different CFD solvers are possible.

Considering that GT-Hybrid method utilizes the free vortex (Lagrangian) method in the near field with a far field trajectory model based on fitting the behavior at a specified wake age while all the other methods use a wake capturing (Eulerian) method, correlation between the GT-Hybrid and others could only be achieved for the first revolution (360° of vortex age) when the vortex is coherent with a very small vortex core radius. At higher vortex ages, factors such as numerical diffusion, grid density, etc., begin to cause deviations among the various methods.

It is also observed that the GT-Hybrid free wake methodology predicts a significantly different tip vortex contraction rate at higher wake ages, compared to other methods. These differences in the tip vortex descent rate, contraction rate and strength of vortex cores influence the hover performance prediction by the different methods, especially at lower collective pitch angles.

On the other hand, the wake capturing model used in STAR-CCM+ captures the wake contraction well before 180° wake age, compared to OVERTRUNS which has the

most agreement with the experimental data considering the integrated thrust and torque coefficients. However, it under-predicts the decent rate of the tip vortex.

4.2.4 Pressure Comparisons

As a further verification of the solvers' capabilities, comparison of surface pressure distributions between three solvers - GT-Hybrid, STAR-CCM+, and OVERFLOW – have been done for the baseline S-76 configuration, and for a rectangular planform of same solidity. The OVERFLOW results are from AIAA Hover Workshop archives. The surface pressure distributions shown in Figure 18 are calculated corresponding to $C_T/\sigma = 0.09$ condition for the two tip planforms. It is observed that there is a marginal difference at the inboard location of 75% radius position between the two solvers. Compared to STAR-CCM+ and OVERFLOW [95], GT-Hybrid over-predicts the suction peak at the inboard location of 40% radius position for both rectangular and swept and tapered (baseline) case. Results of STAR-CCM+ agree generally well with solutions obtained from OVERFLOW, except for the pressure suction at 97.5% radius position where STAR-CCM+ prediction is similar to GT-Hybrid.

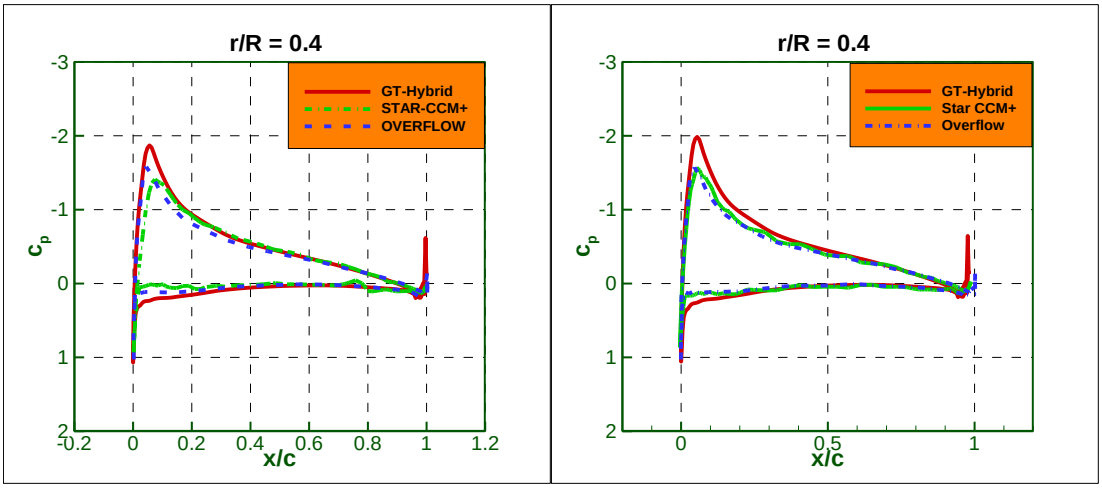

(a) 40% span wise (b) 40% span wise

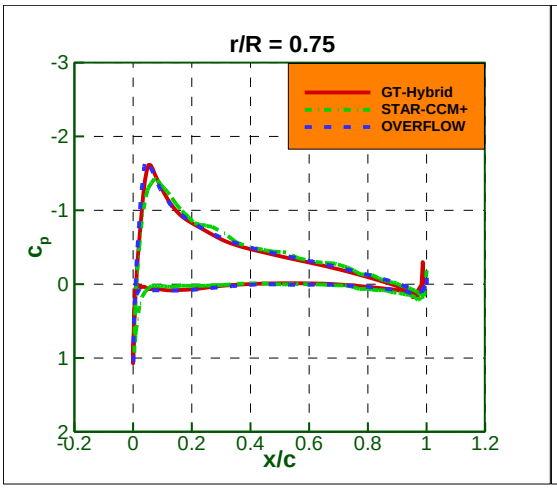

(c) 75% span wise

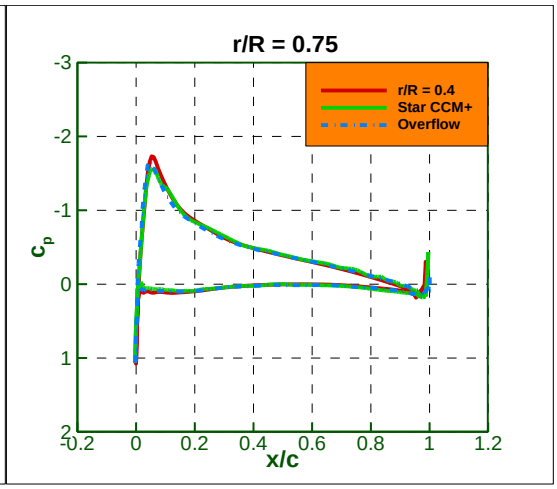

(d) 75% span wise

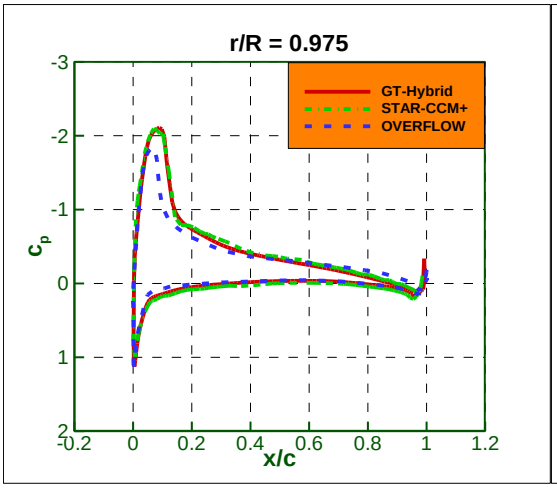

(e) 97.5% span wise

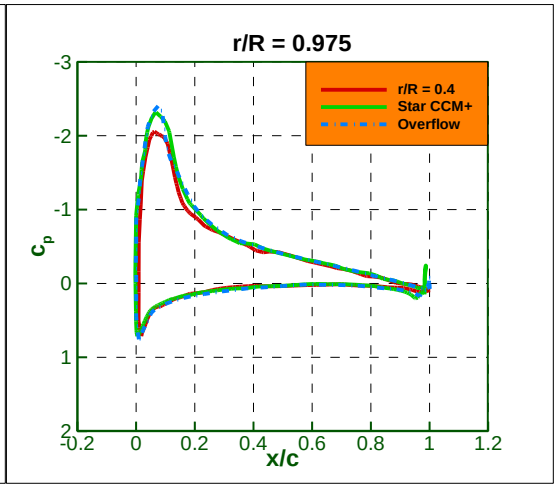

(f) 97.5% span wise

Figure 18 Comparisons of pressure coefficient span wise distribution of the rectangular tip Plan- form (left) and swept tapered Planform (right) at $C_T/\sigma = 0.09$ obtained from different solvers

In summary, both GT-Hybrid and STAR-CCM+ give a reasonable estimation of integrated force and flow field data (vortex trajectory), compared with either experimental

data or solutions obtained from other CFD solver (with different level of fidelities). In the present work, GT-Hybrid was used extensively for preliminary studies and for trimming the rotor for a specified thrust setting. STAR-CCM+ was used in subsequent studies.

CHAPTER 5. ASSESSMENT OF TIP PLANFORM EFFECTS

In the previous chapter, the flow solvers were validated using test data available for the baseline S-76 rotor with a swept tapered tip shape. In this chapter, simulations of rotors with different tip planforms are conducted. Since these simulations are all performed in house, a wealth of data-flow field, vorticity, surface pressures, and integrated thrust and torque are available for detail analysis of the physical phenomena. Only a small subset of these results are shown here, highlighting the differences between the various planforms.

These results are presented in the following order. First, the measured and predicted performances of the three rotors, in terms of integrated loads (thrust, power, figure of merit) are presented and compared against test data. Next, the performance data for the three rotors are shown in tabular form. It is found that the anhedral planform does the best among the three planforms. Finally, the physical mechanisms behind this improvement (for the anhedral rotor) are explored from the flow field data.

5.1 Measured and Predicted Performance of the Rectangular Planform Rotor

Figure 19 shows the hover performance of the S-76 rotor with the rectangular planform. The variation of thrust and torque with collective pitch is comparable between the two solvers at high pitch settings, but differs markedly from each other at low pitch settings where GT-Hybrid predicts a higher torque while STAR-CCM+ is close to experiment [13] [6]. This difference is caused by the relatively higher induced velocities from the free wake model at low thrust settings, giving rise to higher induced power. At a

low collective pitch (under 5°), the wake tends to remain close to the rotor plane of rotation and hence affects the induced velocity to a greater extent.

Figure 19 plot (c) and (d) show the improved correlations of C_T vs. C_q and C_T vs. FM using the wake capture model in STAR-CCM+ compared to the free wake model in GT-Hybrid. At a high collective pitch setting of 9.5° for both the solvers, the under-prediction in thrust is compensated by the under-prediction in torque which results in a figure of merit value that matches closely with the experiment.

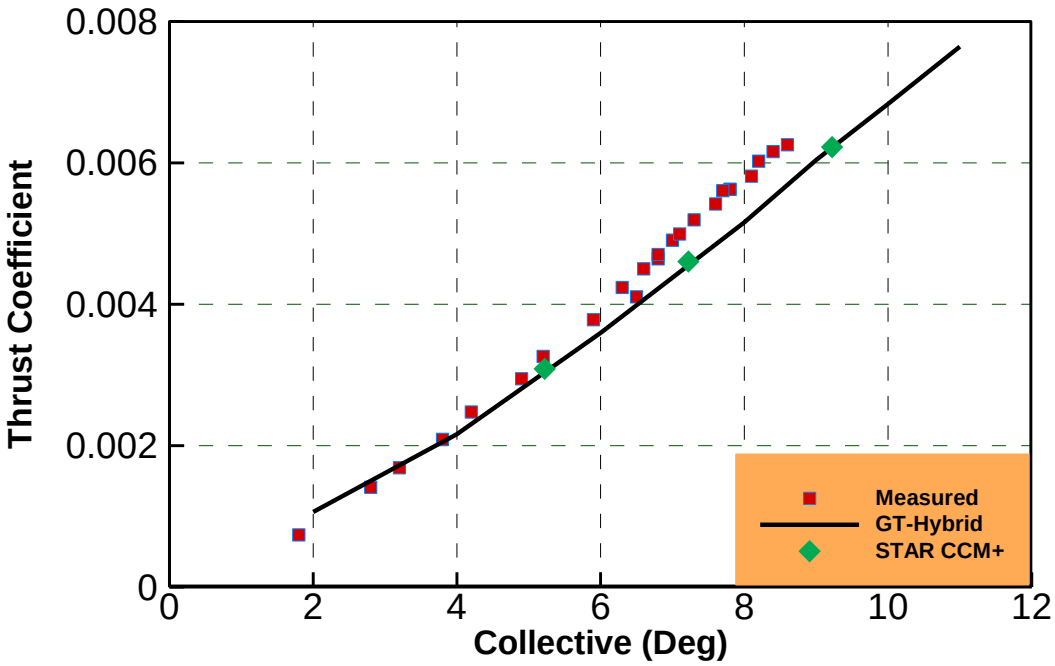

(a) Thrust coefficient vs collective pitch

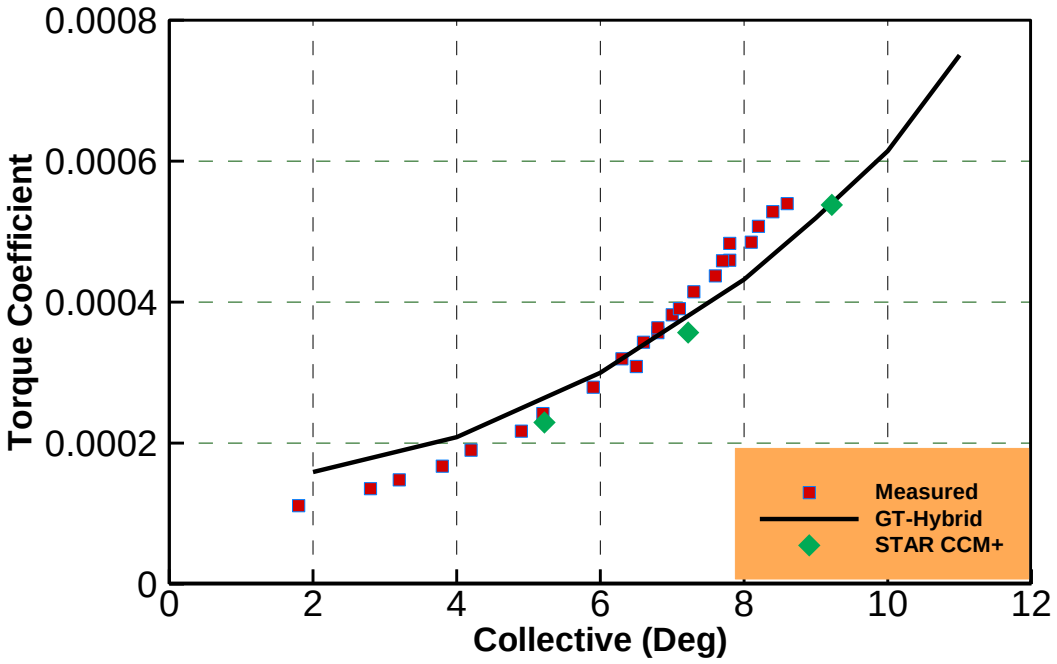

(b) Torque coefficient vs collective pitch

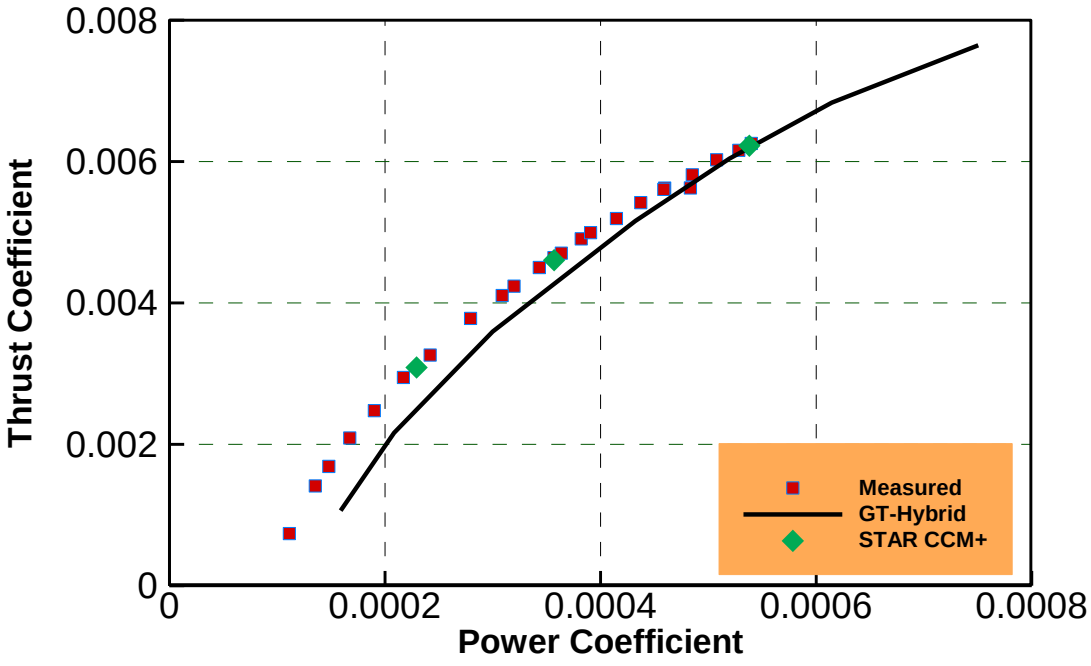

(c) Thrust coefficient vs power coefficient

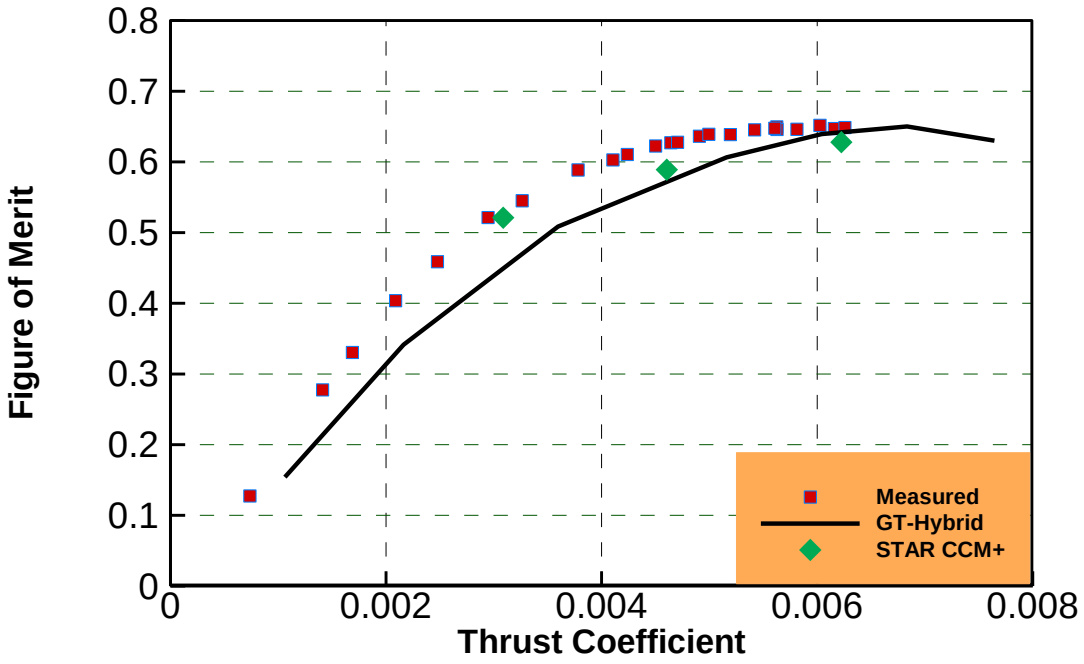

(d) Figure of merit vs thrust coefficient

Figure 19 Performance characteristics of the rectangular tip planform

5.2 Measured and Predicted Performance of the Anhedral Planform Rotor

Figure 20 shows the predicted integrated loads for the rotor with anhedral planform. Both solvers (GT-Hybrid and STAR-CCM+) agree well with each other on how the thrust and torque vs. power vary with each other. The figure of merit values also agree with each other. Slight differences between the test data and the predictions are evident.

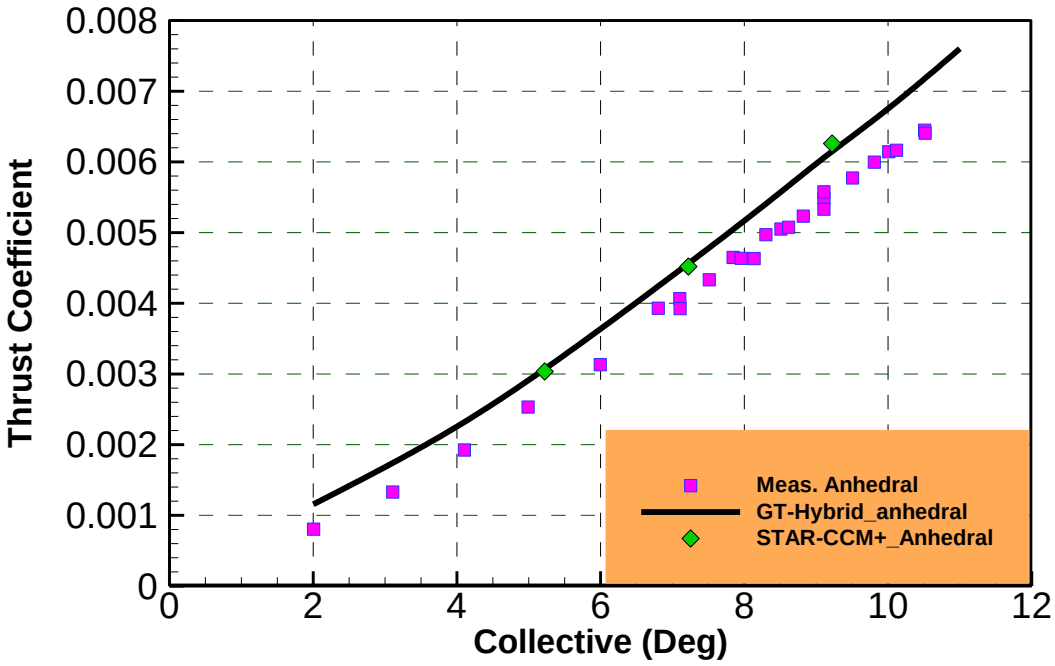

(a) Thrust coefficient vs collective pitch

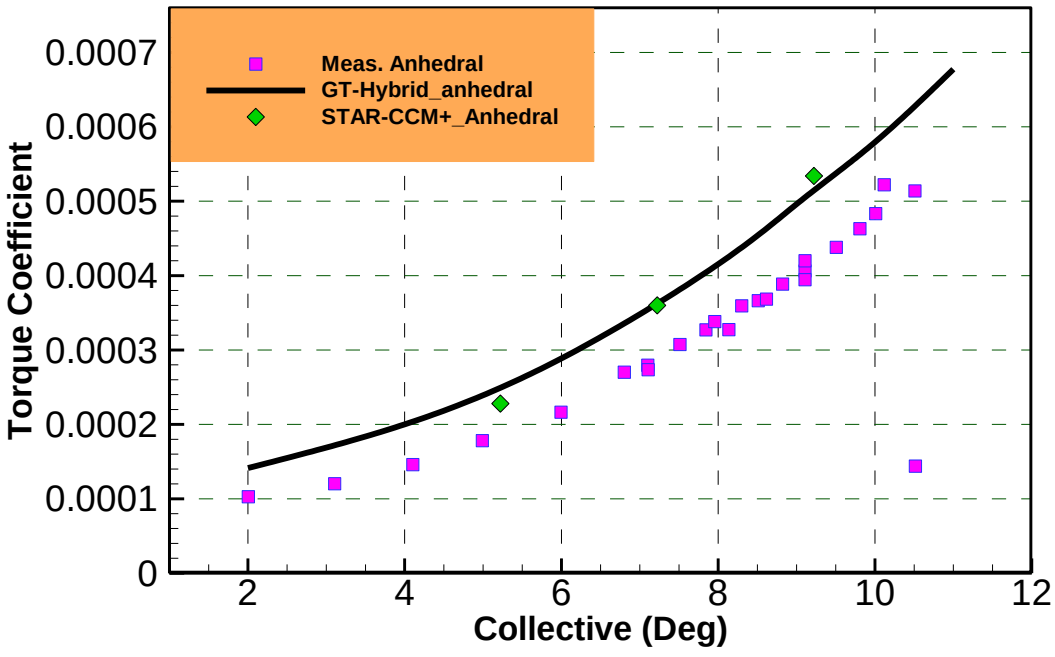

(b) Torque coefficient vs collective pitch

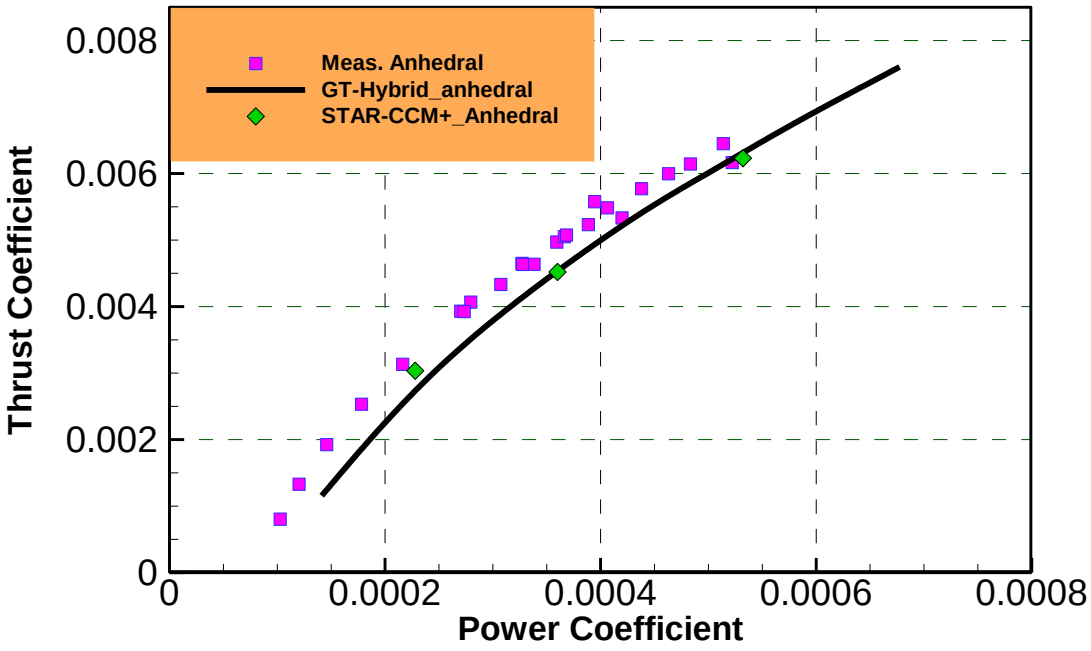

(c) Thrust coefficient vs power coefficient

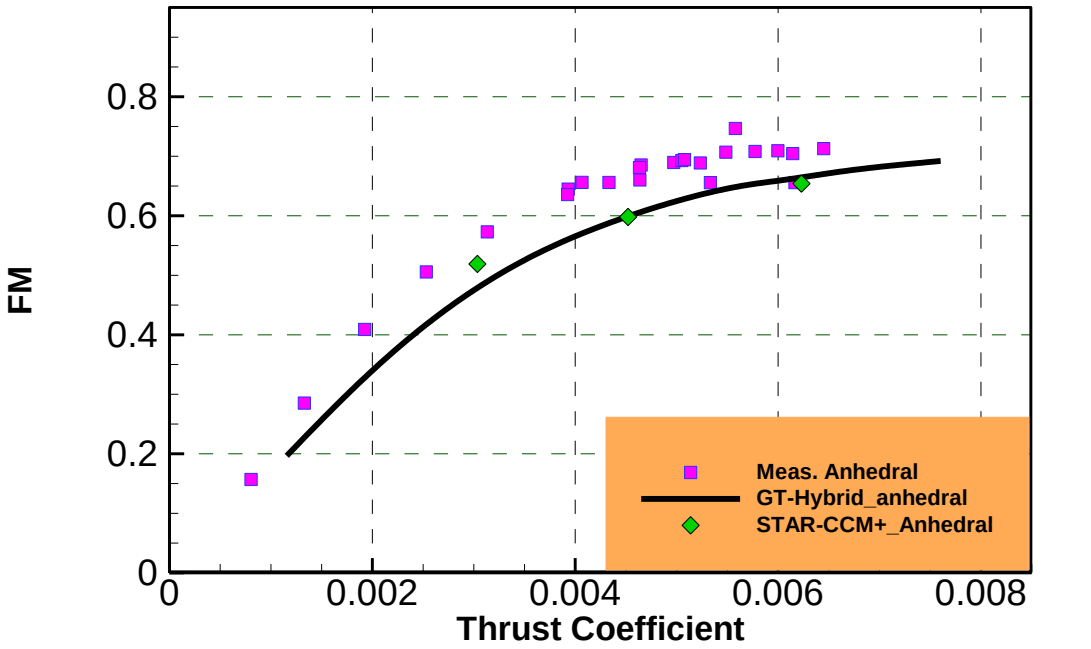

(d) Figure of merit vs thrust coefficient

Figure 20 Performance characteristics of the anhedral tip planform

It is shown in Figure 20 that the rotor performance has been improved by adding anhedral to the tip. As CFD methods are capable of producing a wealth of data on the tip vortex formation, roll-up, and subsequent evolution, the flow field visualization is shown in the next sub-section, accompanied by analysis for physical explanations of this improvement.

5.3 Effects of Planform on Figure of Merit

As stated earlier, the variation of figure of merit with thrust over the entire operating range is of particular interest. The test data [6] indicate that the unswept tip begins to pay a penalty at higher tip Mach numbers (0.65 in the present case). The straight tapered blade is more efficient at lower thrust settings. As thrust setting increases, its performance diminishes presumably due to transonic effects, relative to swept tips. The swept tapered tip with anhedral performs significantly better than all the other planforms over the entire range.

We next present the predicted data for the various planforms in Figure 21. To prevent data clutter, only the results from GT-Hybrid are shown. It is seen that the anhedral rotor has the best performance, i.e. highest figure of merit, particularly at high thrust settings. Rectangular planform has the worst performance. These findings are consistent with the test data shown in Figure 21.

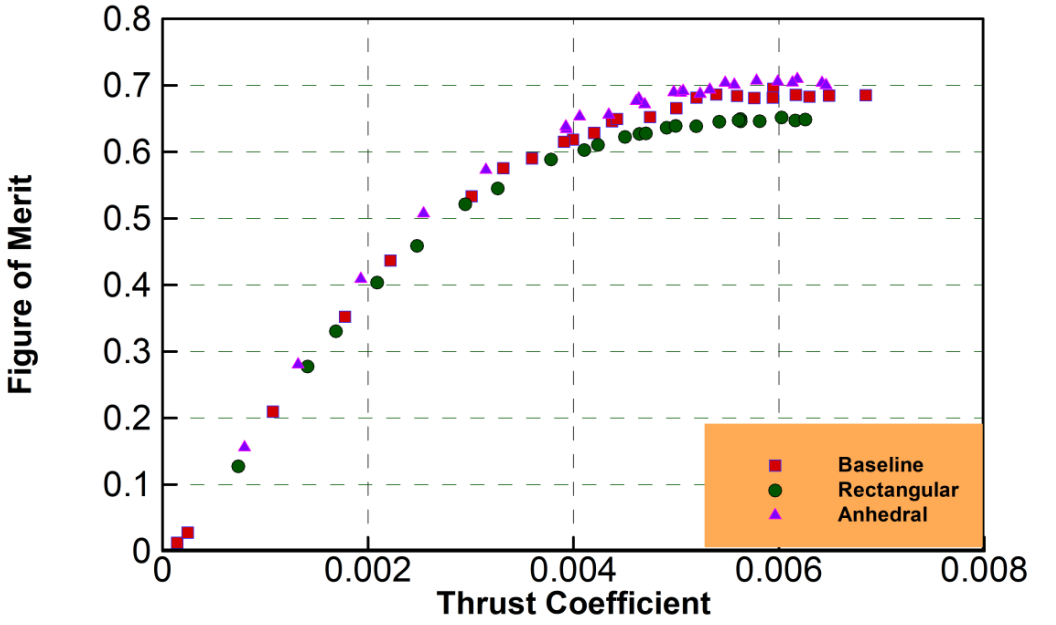

(a) Measured figure of merit data for various planforms at M_{tip}= 0.65 [6]

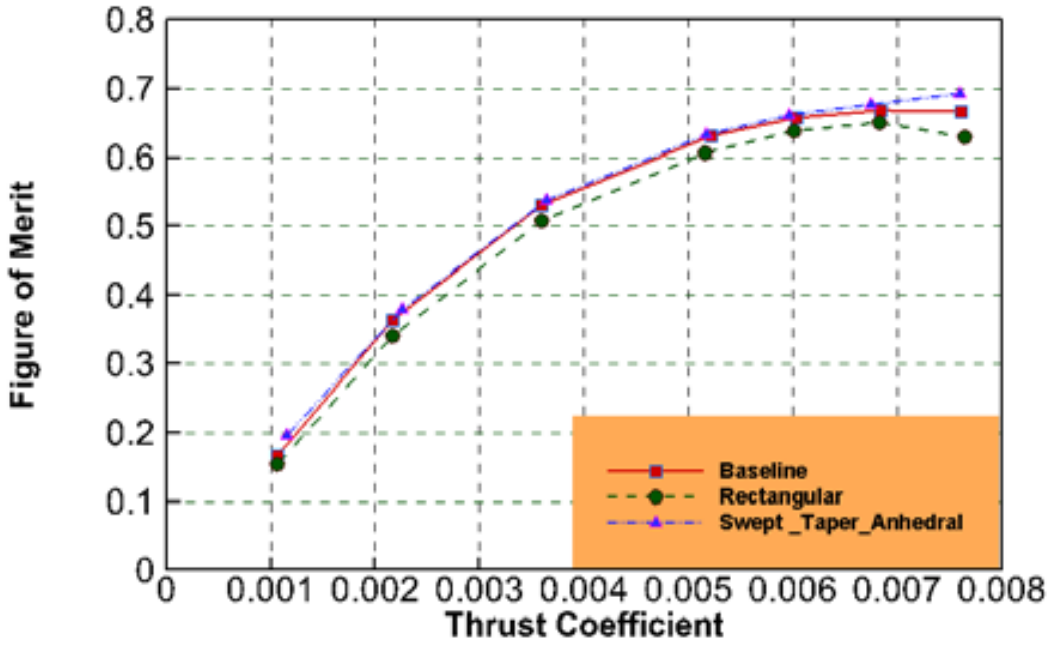

(b) Effects of planform on figure of merit (Calculations)

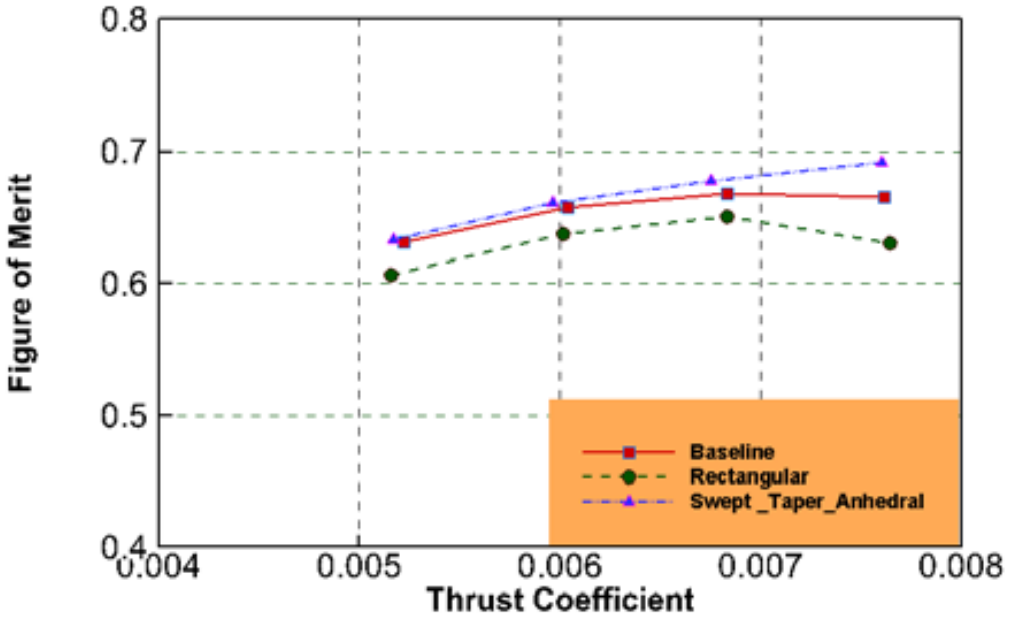

(b) Effects of planform on figure of merit (Calculations Enlarged View, Calculations)

Figure 21: Effects of planform on figure of merit

To understand the improved performance of the baseline rotor over the rectangular planform, surface pressure contours, and radial loading have been examined for a representative thrust setting of $C_T/\sigma = 0.086$. The sweep and the taper both tend to reduce the tip loading as shown Figure 21, relative to the rectangular planform. The reduction in the wetted area relative to the rectangular planform also has a small effect on the profile power. These factors collectively influence the figure of merit as seen in Figure 23. We next look at the anhedral tip. An examination of the blade loading shown in Figure 22 indicates a further reduction in tip loading compared to the rectangular planform or the baseline S-76 planform.

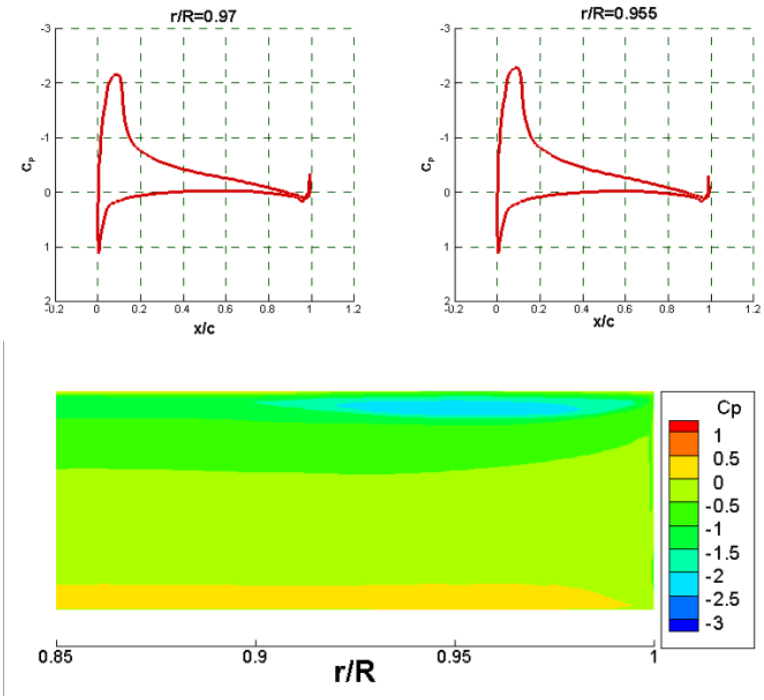

(a) Rectangular Tip ($C_T/\sigma = 0.086$)

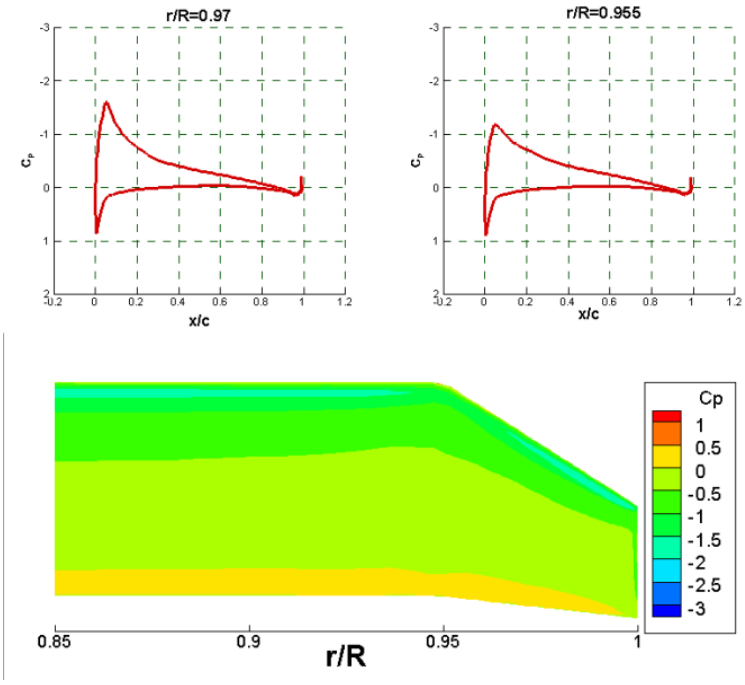

(b) Baseline Swept Tapered Tip ($C_T/\sigma = 0.086$)

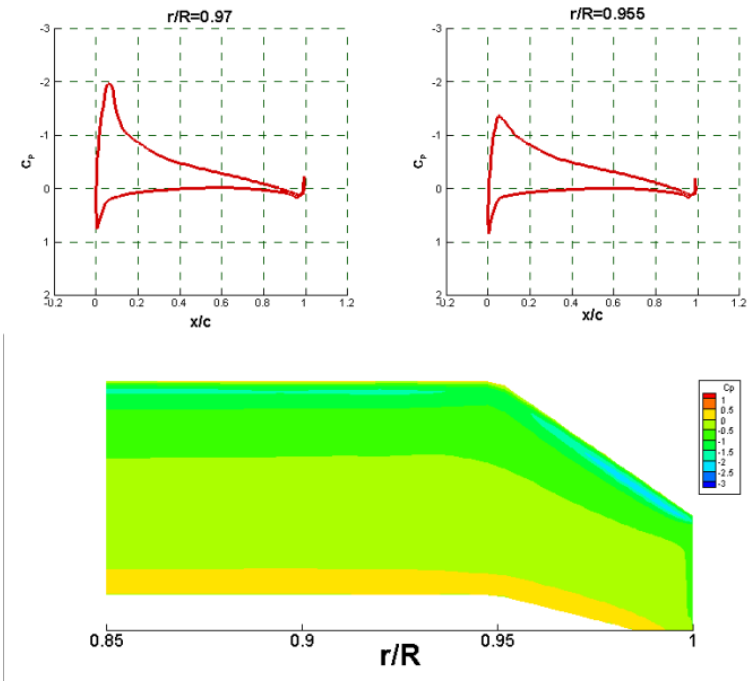

(c) Anhedral Tip ($C_T/\sigma = 0.086$)

Figure 22 Pressure Distribution over the Tip Region for Three Planforms

The effects of tip planform on the surface pressure distribution are shown in Figure 22. In addition to the tip load reduction caused by introducing taper and sweeping angle to the blades, Figure 22 (c) shows there is a little increase of tip loading at the really tip region (98% radius) adding by anhedral angle, making the blade loading even more uniform. More detailed results of blade loading which can be represented by the bound circulation distribution on the rotor blade will be shown in the next section.

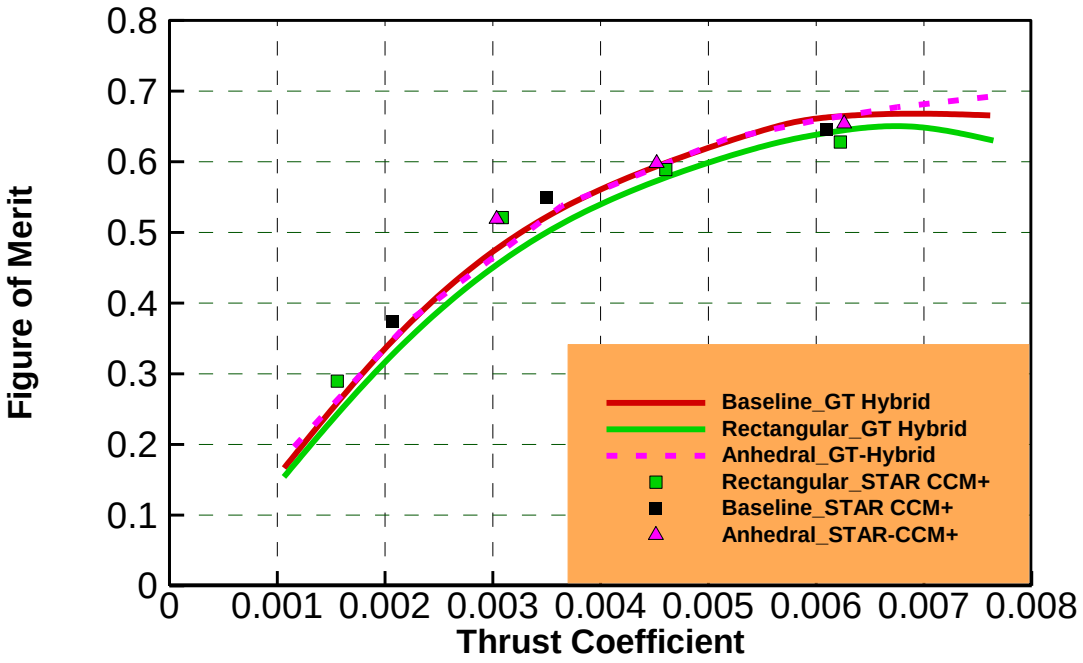

(a) CFD results of tip planform effects on rotor performance

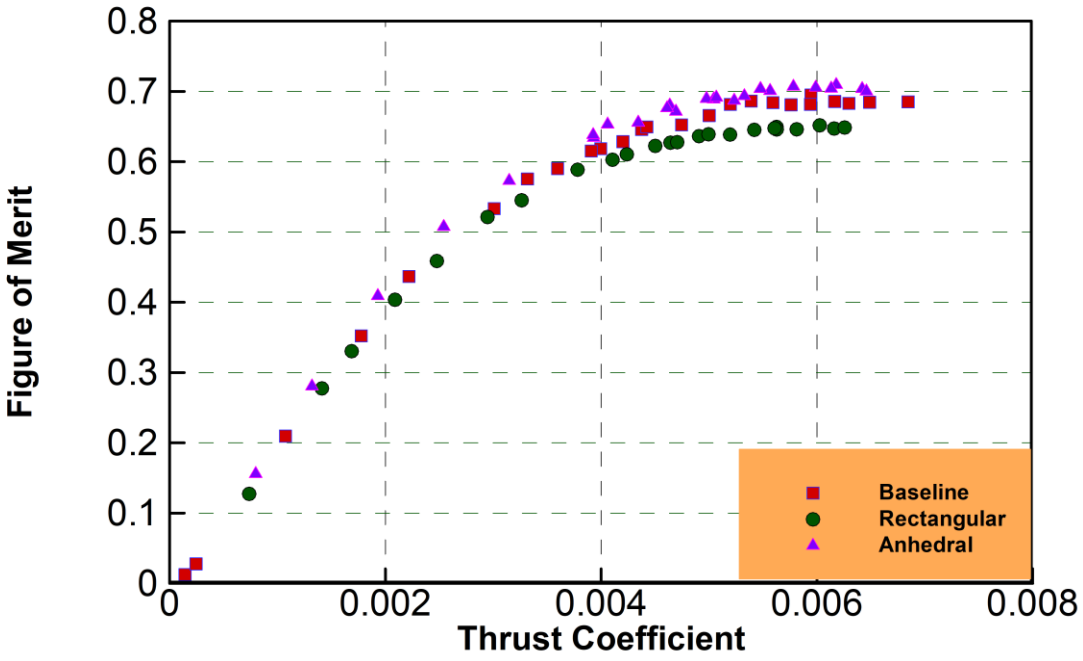

(b) Experimental results of tip planform effects on rotor performance

Figure 23: Effects of planform on figure of merit

The effects of tip planform on the figure of merit are shown in Figure 23. As expected, tapering and sweeping leading edge improves the rotor performance by increasing FM at particular thrust settings. Another observation from the plot is that anhedral tip improves the rotor performance as well, though not significantly, and the change of FM is mainly due to the reducing of induced power. As shown in Table 4, the profile drag is not affected by the tip planform much (up to 3% differences in the profile power and up to 0.2% differences in total power). That means the tip planform mainly affects the induced power. This conclusion is consistent for both numerical solutions (from GT-Hybrid and STAR-CCM+) and experimental data, and it is interesting because it still remains unknown how the anhedral tip shape affects the thrust and torque.

Table 4 Tip planform impact on decomposed power coefficients

	C_T	C_Q	FM	$C_Q(Profile)$
Rectangular	0.00632	0.00054	0.65620	0.0000302
Baseline	0.00625	0.00055	0.63963	0.0000310
Anhedral	0.00627	0.00053	0.65402	0.0000313

There are many possible reasons for the improved performance of the anhedral tip relative to the baseline swept tapered tip. The hypothesis tested in this study is that the tip vortex is released at a lower location, below the rotor disk, for the anhedral tip compared to the other tip shapes. The slightly increased clearance between the vortex and rotor blades would make the inflow more uniform, as a result of mitigated tip vortex.

There are also many other aspects to explain the phenomenon of this performance improvements. The following sections focus on the physical explanations based on CFD results, and are attempted to disentangle the effects of pressure distribution (which dominants the thrust of the rotor), the induced velocity distribution (which affects the FM) and other important parameters which may lead to improvement in figure of merit.

5.4 Effects of Planform on Bound Circulation

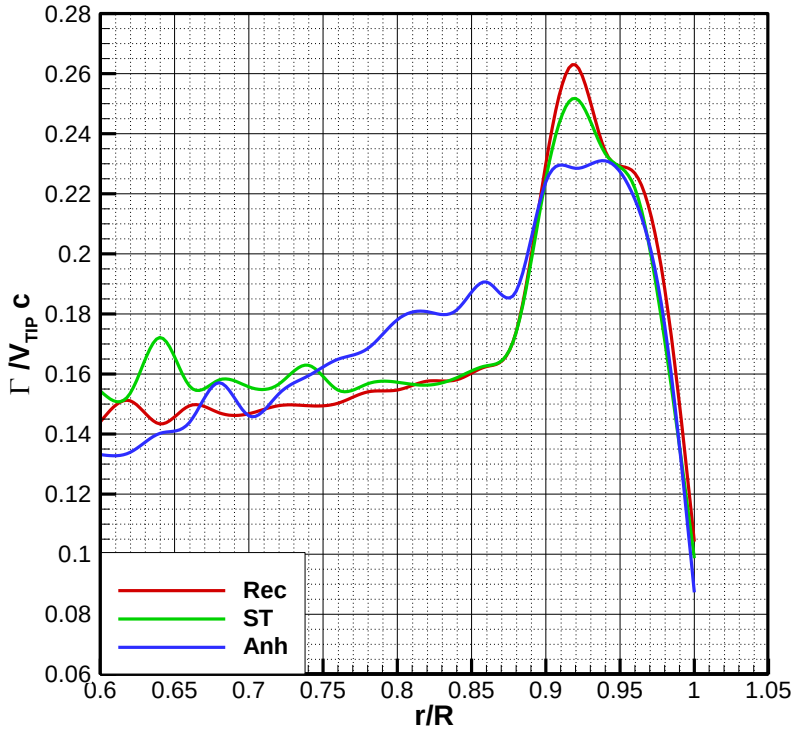

Figure 24 Bound Circulation Distribution on the Blade

Figure 24 shows that bound circulation distribution (from STAR-CCM+) on rotor blade. The bound circulation was numerically computed by a contour integral of the velocity vector along a trapezoidal control surface around the rotor blades, as shown in Figure 25.

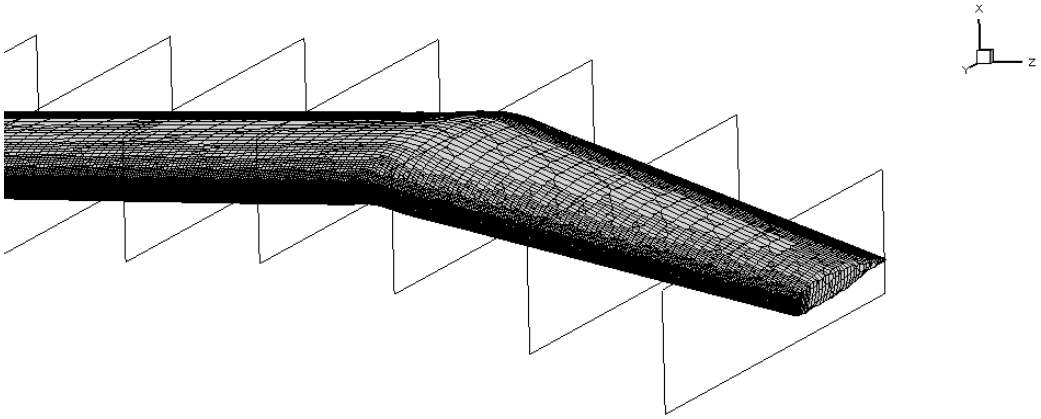

Figure 25 Control surface created to calculate the bound circulation

From Kutta–Joukowski theorem, the sectional lift distribution is linear proportional to the bound circulation. We notice that the anhedral tip has a smoother variation of bound circulation compared to the baseline tip and the rectangular tip. Since tip loading will influence the tip vortex strength, it also follows that a swept-tapered-anhedral tip will have weaker tip vortices.

5.5 Effects of Planform on Inflow Distribution

The radial variation gives rise to trailing vortices, which in turn influence the induced flow. A smoother radial distribution of bound vortices imply weaker trailing vortices, which in turn imply a smoother induced velocity distribution.

Figure 26 shows the inflow velocities computed numerically for the swept and tapered tip shapes with and without anhedral on the rotor disk at a collective pitching of 9.5°. Because the results are solved in the condition of hover, the induced velocity distribution is periodic: the results at 30°, 120°, 210°, and 300° azimuth angles all collapse into a single curve, and the period is 90°.

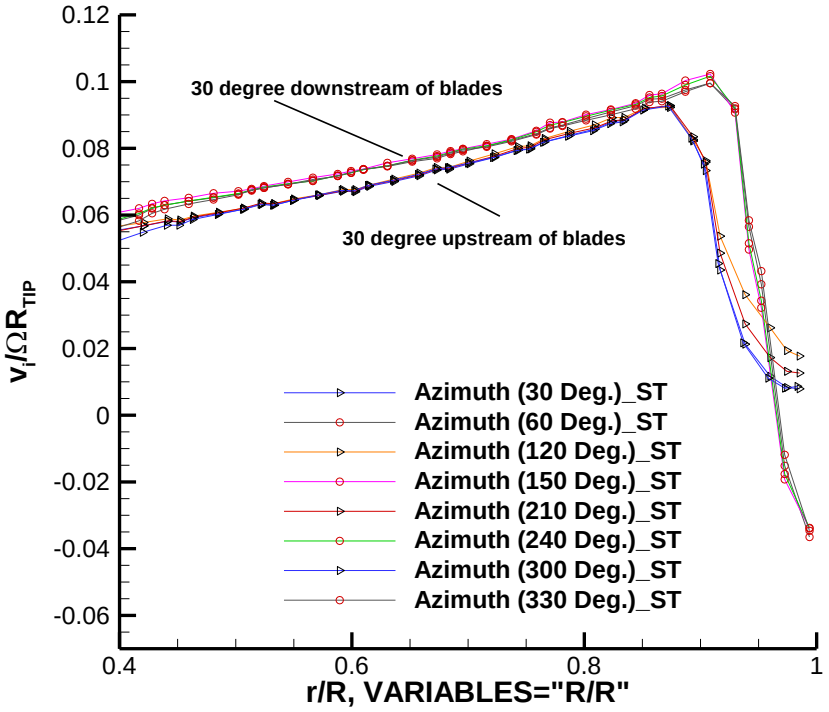

(a) Baseline tip

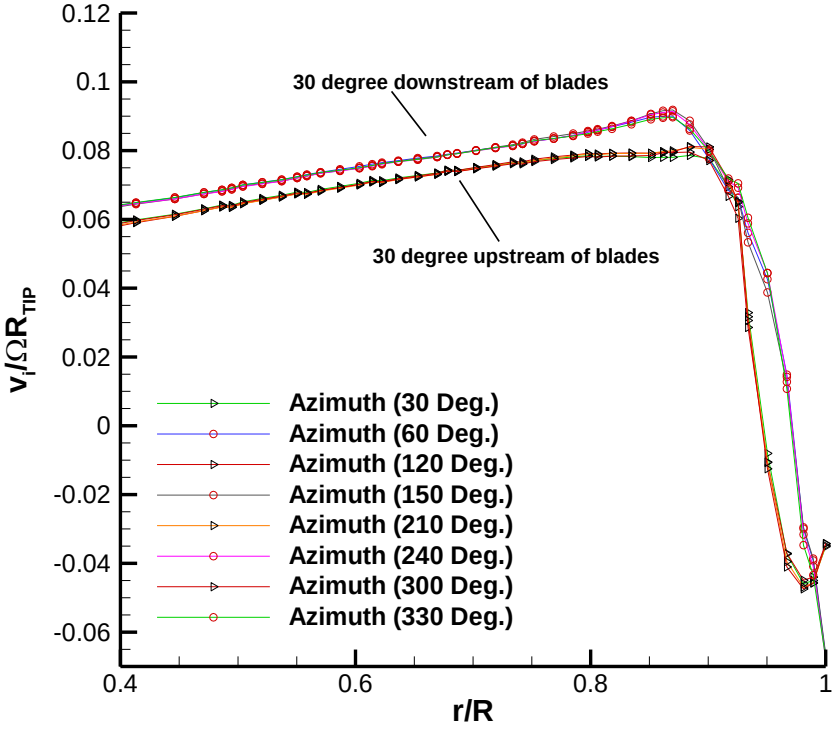

(b) Anhedral tip

Figure 26 Induced velocity distributions on the rotor disk with $\theta_0 = 9.5°$ at different azimuth angles

It is observed that the induced velocity at 30° downstream of the blades is higher than at 30° upstream of the blades for both rotors. This is simply indicative of the effects of blade bound circulation on the induced velocity upstream and downstream. It is also shown that compared to the baseline, the anhedral tip shape produces an induced velocity with a lower increasing slope in the span wise direction, which gives a smaller variance of the induced velocity.

A time-averaged induced velocity field is shown in Figure 27 for all the three rotors. It is seen that the anhedral tip has a near uniform inflow over the entire radius compared to the other rotors. From classical blade element-momentum theory, such a uniform inflow leads to the theoretically lowest induced power consumed.

In addition to the induced velocity distribution for the baseline and anhedral tip planform shown in Figure 26 and Figure 27, contours of non-dimensionalized induced velocity $\lambda = V/\Omega R$ (where V is the inflow or induced velocity in hover on the rotor disk) over the entire rotor disk have also been generated for the three planforms and are shown in Figure 28 (a), (b), (c). The areas of regions that have high induced velocity (shown in red and orange in the contour plots) shrink monotonically as we proceed from the rectangular tip, to the baseline swept taper tip, and ultimately to the anhedral tip shape. Consistent with the results shown in Figure 26 above, that the anhedral tip indeed produces a more uniform inflow over a large extent of the rotor, and this would contribute to the improved figure of merit.

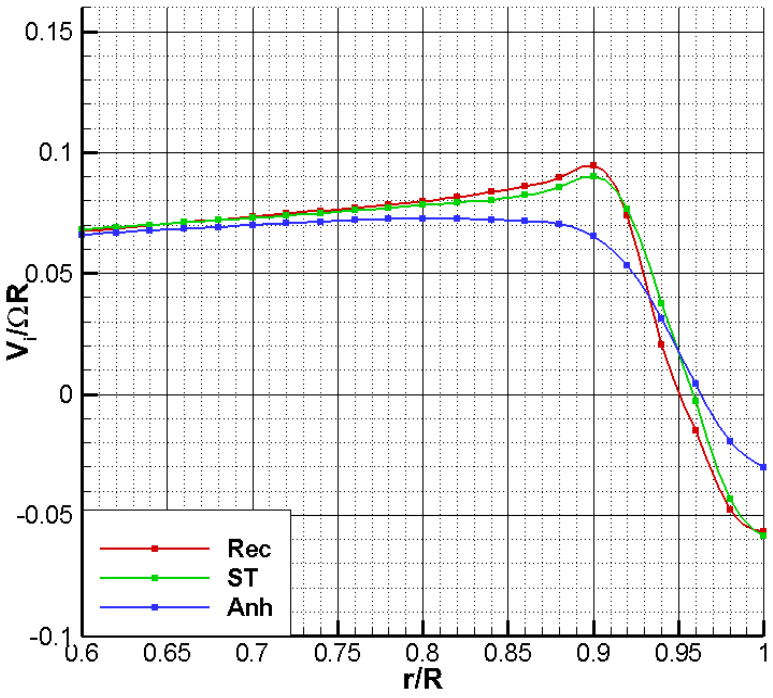

Figure 27 Non-dimensionalized Induced Velocity Distribution over the Rotor Disk

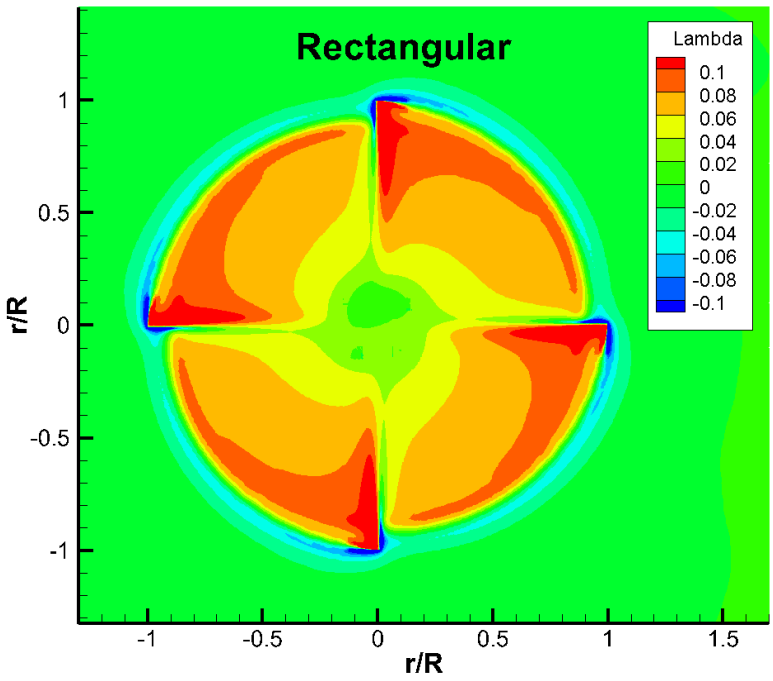

(a) Rectangular tip

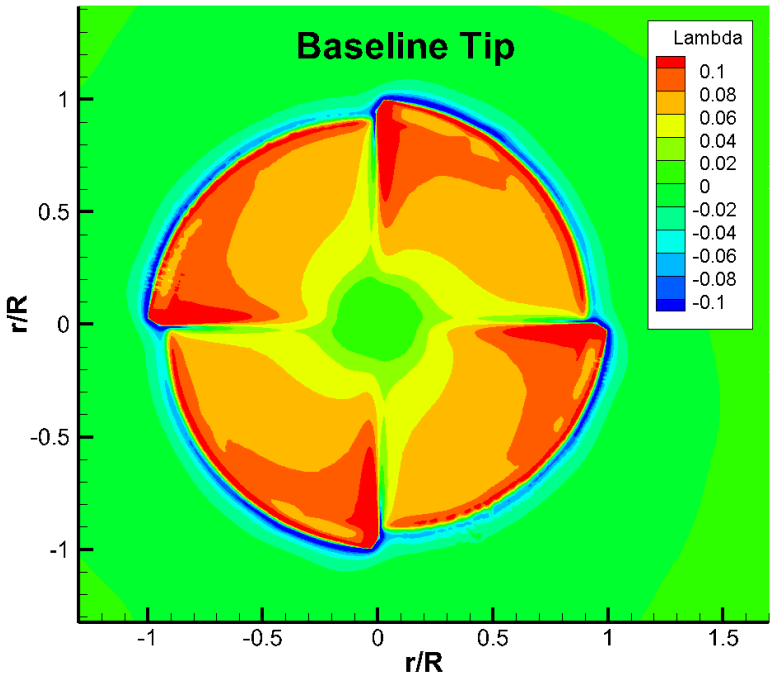

(b) Baseline tip

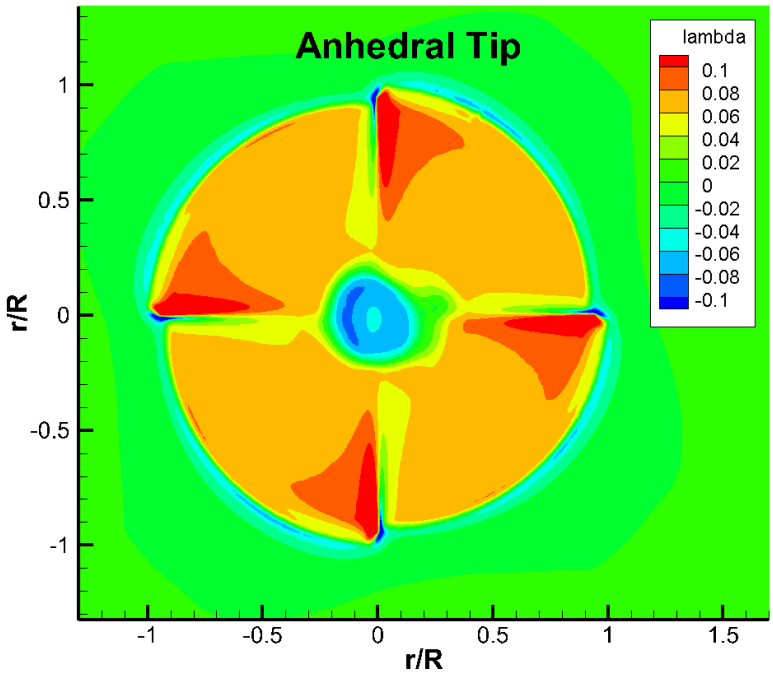

(c) Anhedral tip

Figure 28 Contour plots of the inflow velocity for the anhedral and baseline tip, at 9.5 degrees collective angle

5.6 Effects of Planform on Trailing Vortex Structures

As observed previously, the influence of tip vortex on the induced velocity distribution on the rotor disk is weaker for blades with anhedral tip relative to the baseline and rectangular planform. Flow visualization studies are conducted and shown in this section to gain an insight of the trailing vortex structures for the three planforms (at the same blade loading $C_T/\sigma = 0.09$). In particular, the vorticity distribution at an azimuthal plane 3° behind the blade tip is examined. Only the outer edges of the vortex contours are shown in Figure 29, and the centroid of the vortices is used as an indication of the tip vortex location. To quantify and compare the positions of the tip vortex for all configurations, the iso-surface of the Q-criterion is used which is a common way of show the vortex positions and radius.

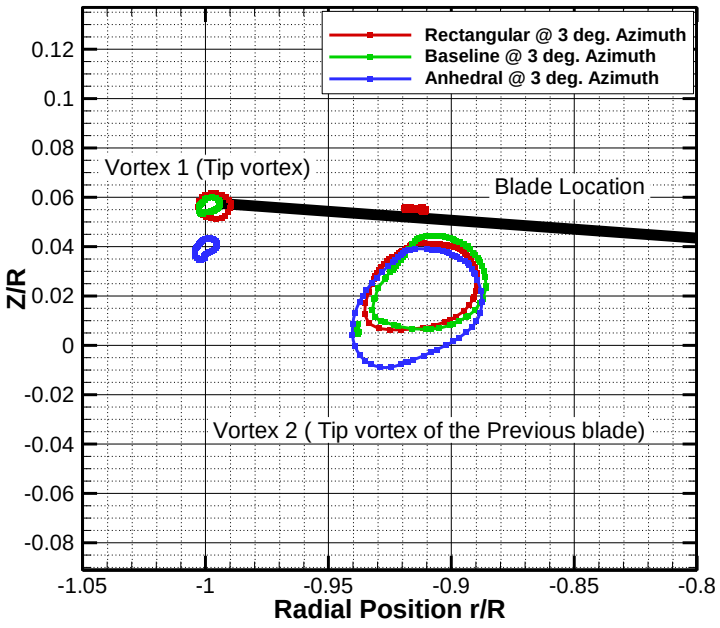

Figure 29 Tip Vortex contours immediately (3°) behind the blade trailing edge

It is seen that the primary tip vortex is released at a slightly lower location for the anhedral tip. In addition, the tip vortex shed from the previous anhedral blade is seen to be more diffused compared to the same blade with a baseline S-76 tip or the rectangular tip. According to Biot-Savart Law, this diffused vortex structure would also be expected to give rise to a smoother inflow distribution.

We next look at the tip vortex structures in more detail. Figure 30 shows the tip vortices for the S-76 baseline configuration released from the current blade and the previous two blades. The older tip vortices are seen at the lower positions, advected by the inflow directed downwards. There is a slight diffusion of the vortex structures from the previous blades compared to the current one.

Figure 31 shows similar visualizations for the anhedral tip. First of all, it is consistently seen that the vortices from the previous two blades are slightly more diffused compared to the S-76 configuration although nearly identical grid densities and turbulence model are employed.

We also see that after 10° wake age, there is a vortex below the current tip vortex which is caused by the merging of two vortices – a vortex shed from the current blade (at the bend point of anhedral tip) and an older tip vortex shed from the previous blades. These two vortices are displaced vertically, and the upper vortex can be traced back to the radial location where the anhedral bend of the planform occurs. It is intuitive to expect that adding anhedral angle to the blade would change the span wise circulation distribution because of the upper vortex shed from the bend corner on the rotor blades. Therefore, the weaker vortex (compared to the tip vortex) shed at the anhedral bending point of the planform is

Baseline Tip

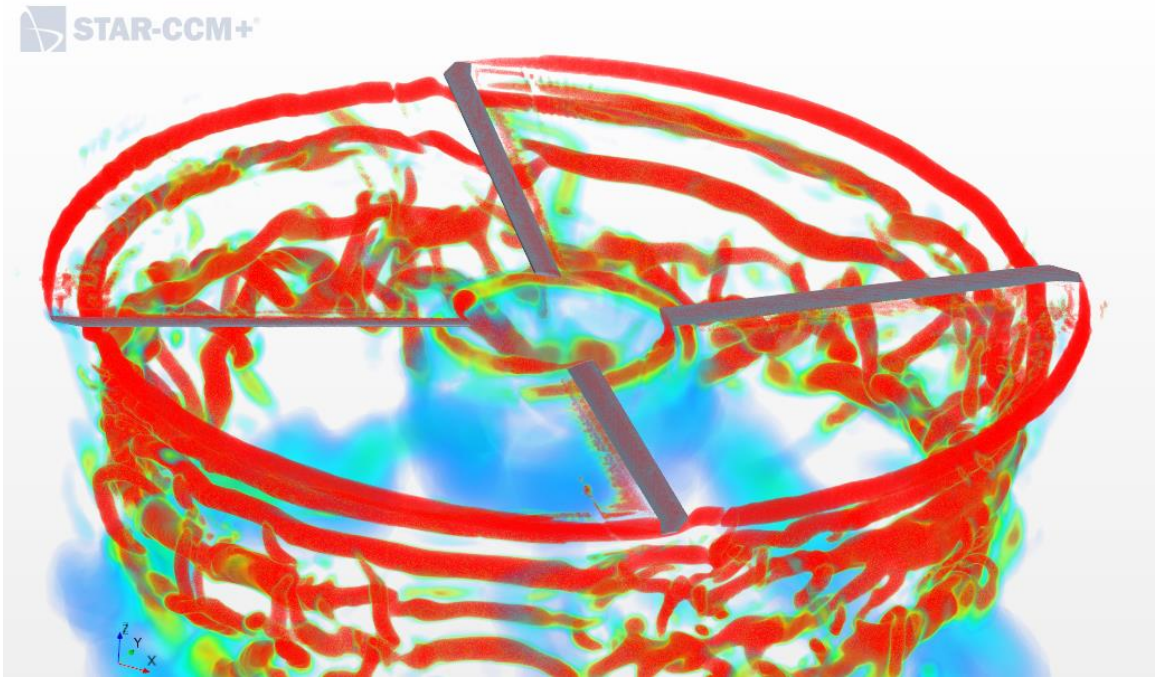

Tip vortex from the previous blade

Tip vortex

Vortex due to BVI

Enlarged

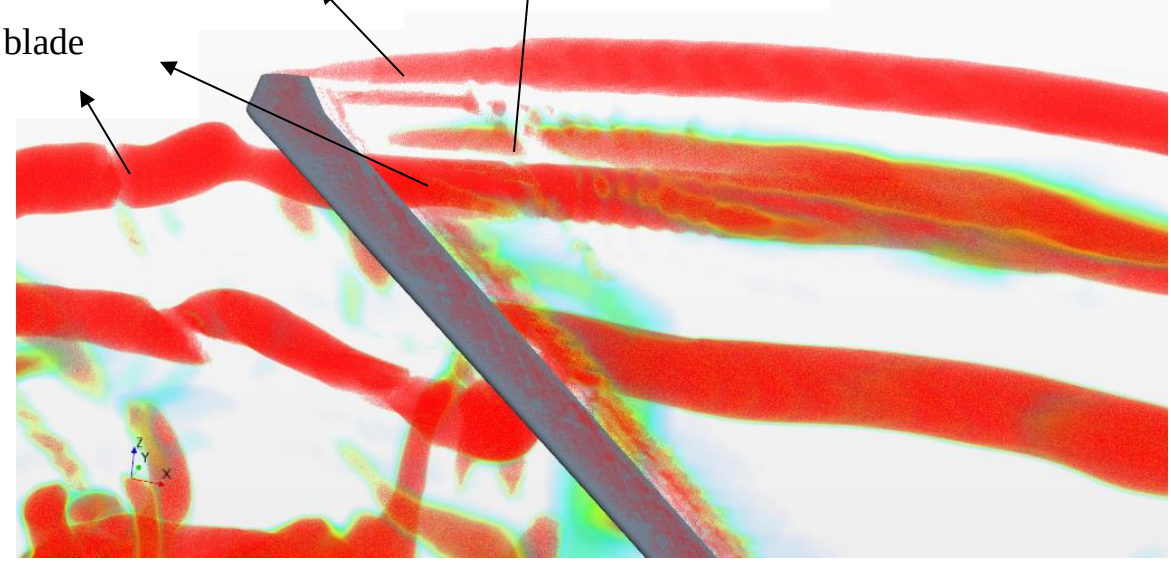

Figure 30 Wake structure released from the baseline tip

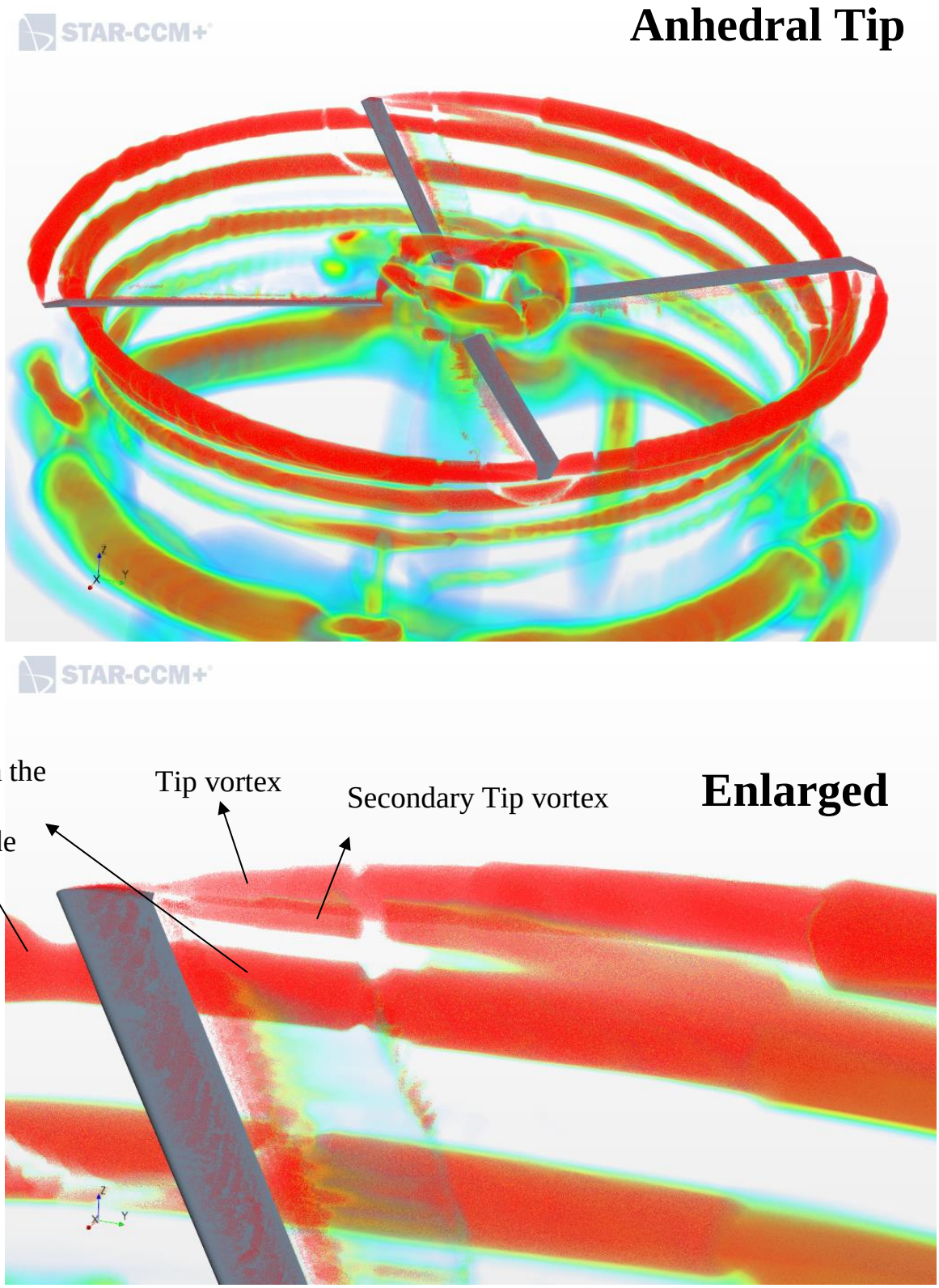

Figure 31 Wake structure released from the anhedral tip

called secondary tip vortex in this thesis, and detailed analysis of the circulation distribution on the rotor blades will be shown in the next sub-section. Because of the presence of the weaker vortex shed from the anhedral tip bend location and weaker tip vortex, the anhedral tip case is also expected to have a smoothed out inflow distribution over the rotor disk.

5.7 Anhedral Angle Sensitivity on FM

Once the influence of anhedral angle on rotor performance in hover and forward flight is well analyzed, a parametric study of the variation of anhedral angle is conducted for an overall picture of the understanding.

The simulation with a sweep of anhedral angles trimmed at the same thrust setting has been conducted in this work using STAR CCM+. The results for the performance are shown in Table 5 and in Figure 32.

Table 5 Effect of Anhedral Angle on Rotor Performance (Rotor is trimmed for $C_T/\sigma = 0.09$)

Anhedral Angle	0°	5°	10°	15°	20°
C_T	0.006260	0.006370	0.006289	0.006292	0.006300
C_Q	0.000540	0.000545	0.000531	0.000530	0.000530
Figure of Merit	0.648942	0.659747	0.663752	0.666220	0.667661

Experimental data is available only at 0° and 20° anhedral angles, shown as the green rectangular dot in Figure 32. The differences between the predictions and measurements are 4.9% and 4.7% respectively at these two anhedral values. From the figure, the wake capture model predicts the trends of FM well compared to the experimental data, but the absolute values are slightly off by a fixed amount. The identification of the origin of this slight difference requires more work.

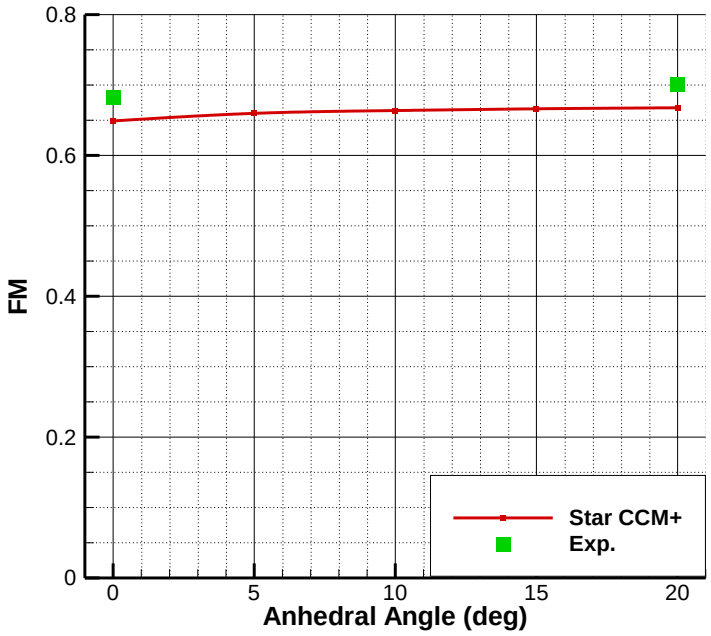

Figure 32 Comparisons of results from Star-CCM+ and the experiment

As shown in the numerical simulations, increasing the anhedral angle improves the rotor efficiency, but the relationship is not linear such that beyond 16 degrees adding more does not show additional improvements in the figure of merit.

CHAPTER 6. TIP PLANFORM EFFECTS IN FORWARD FLIGHT

In the previous chapter, we primarily focused on the effects of the tip planform on hover performance. In this section, we investigate how the tip planform affects the forward flight performance as a function of thrust setting C_T/σ at a representative advance ratio of 0.25, and hover tip Mach number of 0.6.

6.1 Trim and Cyclic Pitch Control

Trimming a rotor in hover is relatively straightforward. For a specified thrust setting C_T/σ, it is only necessary to iteratively adjust the collective pitch angle θ_0. The coning angle β_0 of the rotor may be found from the equation:

$$I\Omega^2\beta_0 = \int_{Hinge}^{Tip} L'r \; dr$$

A very simple rigid body rotation is needed to rotate the grid as β_0 changes with trim.

In forward flight, in addition to the thrust setting C_T/σ, it is customary to specify the shaft angle of attack α shaft (or the tip path plane angle α_{TPP}), and the pitching and rolling moments at the hub. The shaft angle determines the tip path angle, and vice versa, and affects the propulsive force generated by the rotor. In this work, the shaft angle of attack (measured in experiments) was used, with the recommended corrections for wind tunnel wall interference effects [14] [12].

The trim variables are the collective pitch θ_0, the longitidinl cyclic θ_{1c}, and the lateral cyclic θ_{1s}. The blade undergoes a sinusoidal pitching montion as shown below:

$$\theta = \theta_0 + \theta_{1c}cos\Psi + \theta_{1s}sin\Psi$$

The trim variables are iteratively adjusted until the specified thrust setting and the specified hub moments are achieved. In this study, the hub moments were set to zero. Thus,

$$\frac{1}{2\pi}\int_{Hinge}^{Tip} L'rsin(\varphi)\ drd\varphi = 0$$

$$\frac{1}{2\pi}\int_{Hinge}^{Tip} L'rcos(\varphi)\ drd\varphi = 0$$

Instead of specifying the thrust setting, the collective pitch was specified and the resulting thrust was computed.

The blade flapping response was computed from

$$I\ddot{\beta} + I\Omega^2\beta = \int_{Hinge}^{Tip} L'rcos(\varphi)\ dr$$

A harmonic balancing approach was used to solve the above equation. In this approach, we first assume the flapping motion:

$$\beta = \beta_0 + \beta_{1c}cos\Psi + \beta_{1s}sin\Psi + \beta_{2c}cos2\Psi + \beta_{2s}sin2\Psi + \cdots$$

Only the first harmonics are kept. We next represent the right hand side as a Fourier series. We equated the constant term, and the sine and cosine terms on the left and right sides to extract the flapping dynamics.

Table 6 shows the resulting values for a range of collective pitch settings.

Table 6 Cyclic pitching setting for 5 runs with $\mu = 0.25, M_{tip} = 0.60$ [14] [12]

θ_0	θ_{1c}	θ_{1s}	β_{1c}	β_{1c}	C_T/σ	C_Q/σ	$\Delta\alpha$
2	8.67	2.60	0.17	0.07	0.01779	0.001092	0.13
4	8.5	3.74	0.17	0.2	0.03833	0.001245	0.27
6	8.39	4.75	0.03	0.19	0.05809	0.001544	0.42
8	8.29	6.38	0.12	0.19	0.07790	0.002120	0.56
10	7.81	7.58	0.07	0.31	0.09931	0.002900	0.71

6.2 Integrated Data in Forward Flight Condition

Forward flight calculations have been done for the baseline rotor and the rotor with the anhedral tip for the conditions shown in Table 6 above [14]. It is was necessary to perform the calculations for five full revolutions of the rotor, in order to remove the transients in the solution that arise during the impulsive start. Figure 33 shows the azimuthal variation of the thrust coefficient and the hub moments for a representative condition, of the baseline S-76 rotor, for revolutions from 3 to 5. It is seen that periodicity has been established after the second revolution, and that the hub moments are varying about the mean zero values.

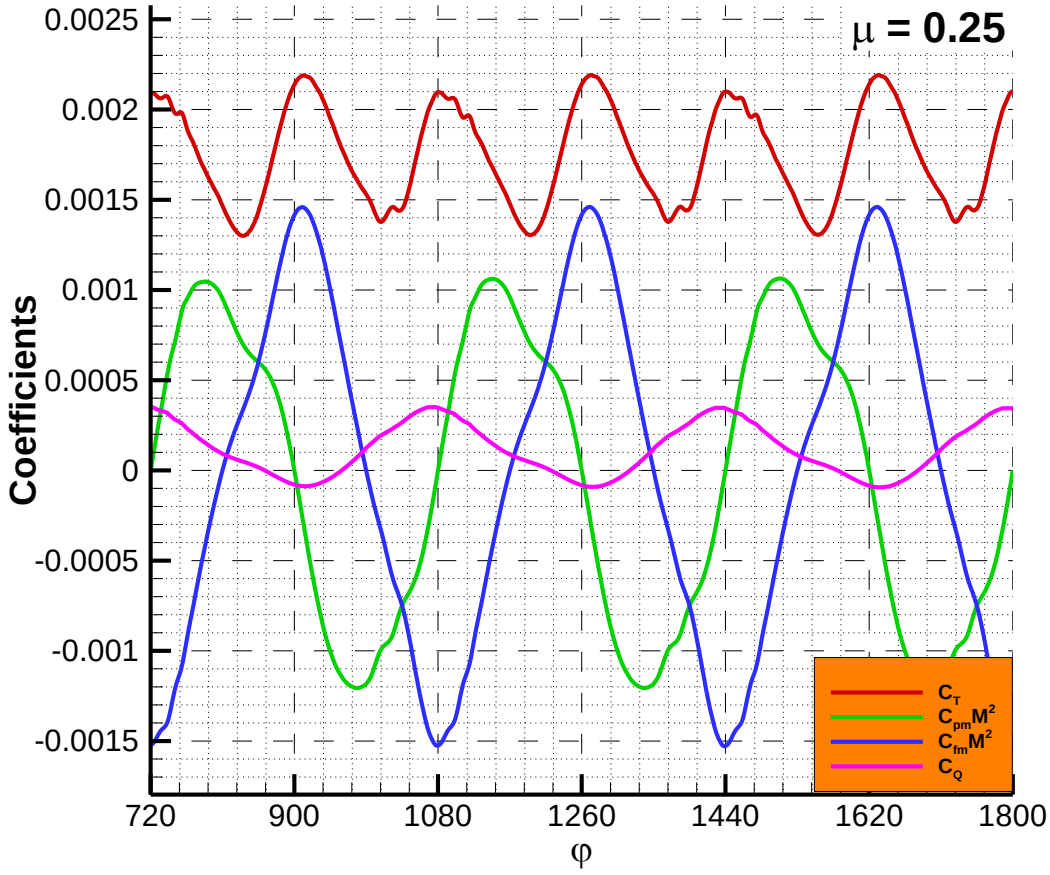

Figure 33 Historical integrated force coefficients, flapping moment coefficients, pitching moment coefficient

Figure 34 shows the variation of the torque coefficient with the thrust setting. For comparison, the measured data for the baseline S-76 rotor are also shown. The agreement for the Baseline S-76 between the predictions and measurements is reasonable, given the fact that elastic effects and the hinge offset effects were not included. It is also seen that the integrated performance is not affected significantly by the addition of anhedral to the tip. The reason is as follows. The power consumed by the rotor is the sum of induced power, parasite power, and profile power. As advance ratio increases, parasite power and

profile power increase, and induced power decrease. Any benefits (or reductions) in induced power attributable to the tip effects becomes very small, and make negligible contributions to the total power. Figure 35 indicates that the wake structures are nearly the same at this advance ratio and thrust setting for the baseline rotor and the rotor with anhedral. Finally, Figure 36 indicates that the induced velocity at a representative instance in time is nearly identical for these two rotors. This further confirms that induced power for these two rotors are likely to be equal.

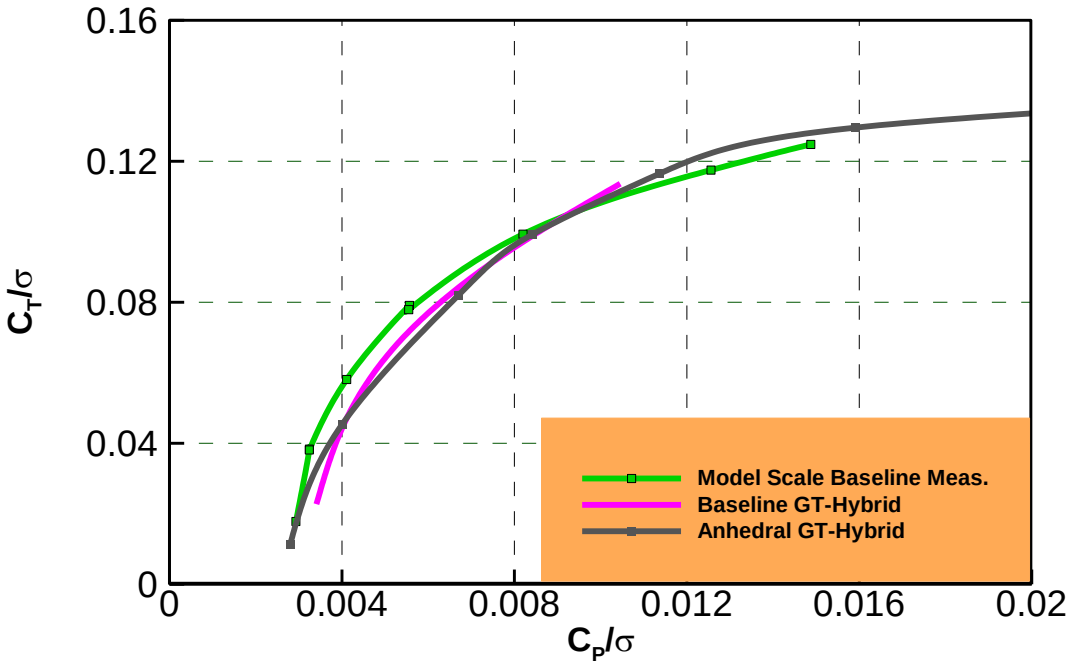

Figure 34 Performance comparisons of the baseline and the anhedral tip

In addition to integrated data, stability and aeroelasticity are also important in rotor aerodynamics. It is known in fixed wing design that anhedral wing decreases the lateral stability of the aircraft [96]. Some of rotorcraft studies indicate that the effect of tip droop (anhedral) is stabilizing, particularly for the first lag mode in hover [97]. The same studies also indicate that with a proper optimized twisted and anhedral tip, there are beneficial

effects in hover and a slightly decrease in vibration levels at high flight speeds. It is further known that the performance of a rectangular planform rotor with a drooped tip is degraded compared to rectangular tip without any droop in forward flight. as much [98].

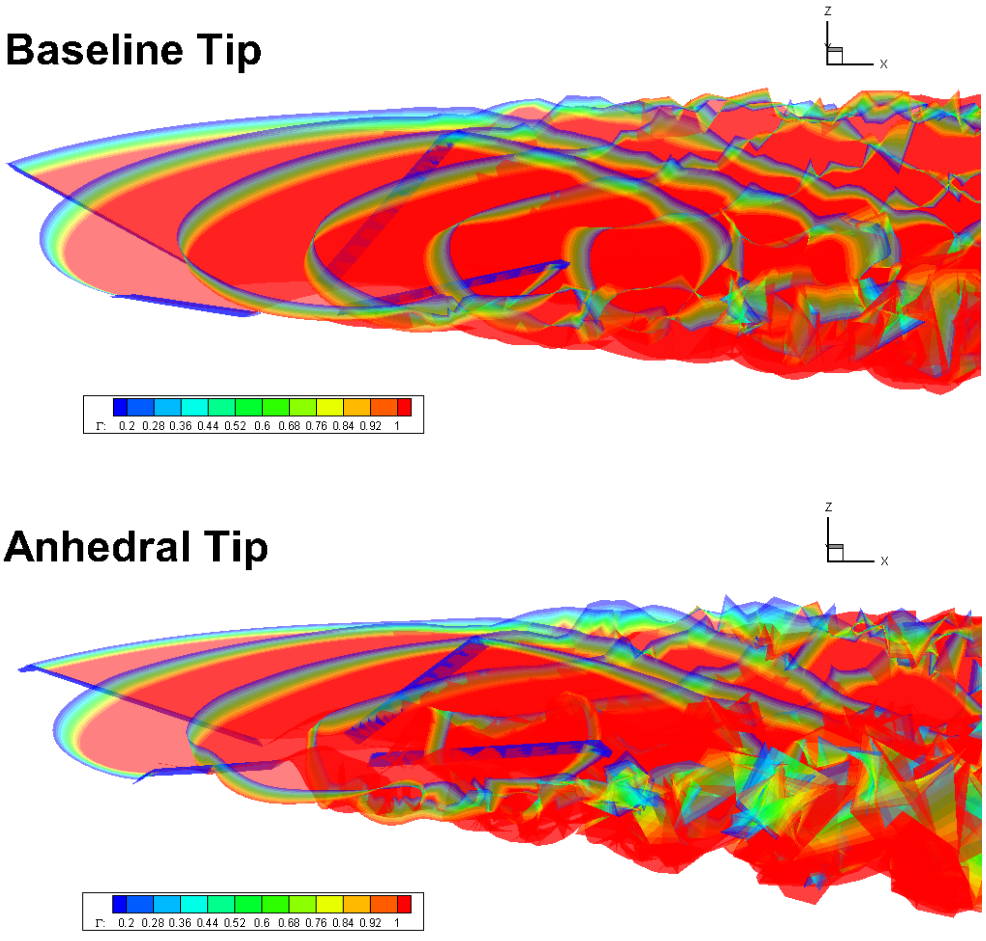

Figure 35 Non-dimensionalized wake circulation colored by strength for the baseline tip and the anhedral tip at C_T=0.0023

However, some other studies indicate that anhedral decreases rotor performance significantly in forward flight offsetting the improvement anhedral provides in hover, due to a downward deflection of the blade tip [99]. Although those aspects are not considered

in the study, there are important aspects of helicopter rotor performance that must be considered in future studies.

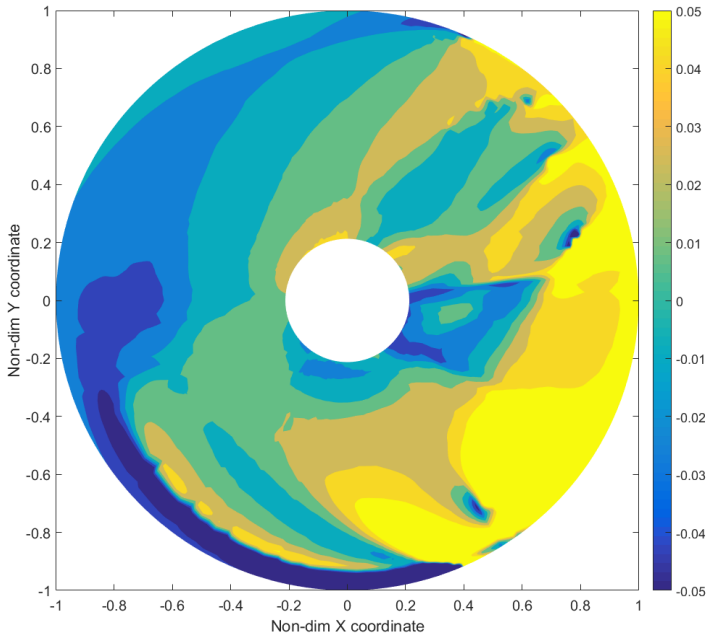

(a) Baseline Tip

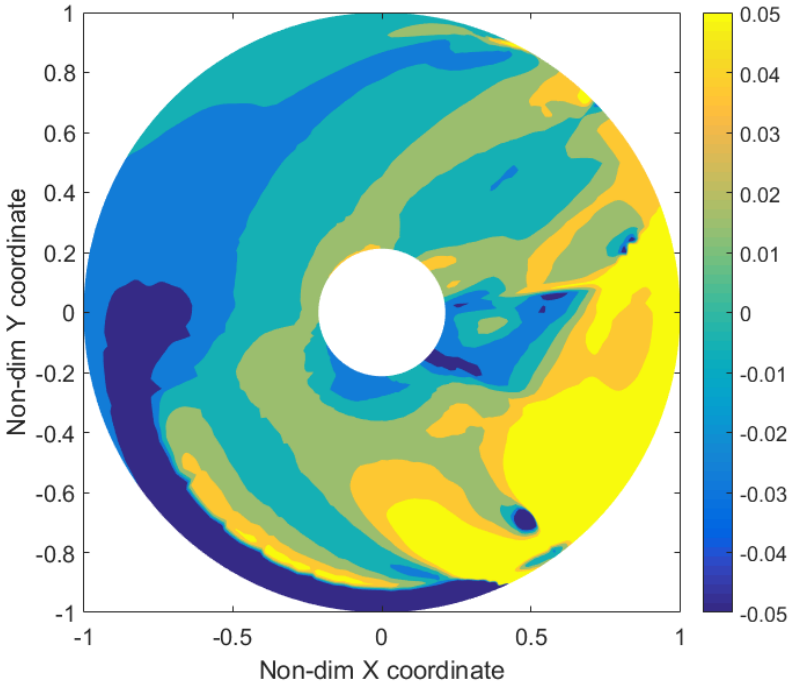

(b) Anhedral Tip

Figure 36 Induce velocity on rotor blades

CHAPTER 7. CONCLUSIONS AND RECOMMENDATIONS

A systematic study of the effects of tip shape on the hover performance of a S-76 rotor has been conducted using two computational fluid dynamics methodologies – a hybrid Navier-Stokes/free wake solver (GT-Hybrid) and a wake capturing commercial Navier-Stokes solver (STAR-CCM+ package). In addition to the baseline S-76 planform, a rectangular unswept tip, and S-76 with parametrically varying anhedral have been considered. Comparisons with available test data and other numerical solutions have been performed. The results from present CFD simulations and the experimental data from various other sources all show that rotors with an anhedral tip achieve the best performance in hover.

In addition to quantitative comparisons of the rotor performance, underlying physical mechanisms behind this improved hover performance of the anhedral tip planform have been studied. This was done through comparisons of surface pressure distributions, radial distribution of the bound circulation, radial distribution of the induced velocity, and tip vortex structures. The thrust loading C_T/σ was kept constant when comparing one planform against another.

7.1 Conclusions of the Current Study

Based on the studies performed, the following conclusions can be drawn:

1. The straight blade is more efficient at lower thrust settings. As thrust setting increases, its performance diminishes relative to swept tips presumably due to

transonic effects. The swept tapered tip with anhedral performs significantly better than all the other planforms over the entire range.

2. For a specified thrust loading C_T/σ, sweep and taper both tend to reduce the tip loading, relative to the rectangular planform. The reduction in the wetted area relative to the rectangular planform also has a small effect on the profile power. These factors collectively improve the figure of merit of the baseline S-76 rotor compared to the rectangular planform. An examination of the blade loading for the rotor with anhedral tip indicates that a further reduction in tip loading compared to the rectangular planform or the baseline S-76 planform.
3. Since tip loading will influence the tip vortex strength, it also follows that a swept-tapered-anhedral tip will have weaker tip vortices. This observation is independently confirmed from estimates of the bound circulation. The bound circulation was numerically computed by a contour integral of the velocity vector. It was observed that the anhedral tip has a smoother variation of bound circulation compared to the baseline tip and the rectangular tip.
4. Rotor with the anhedral tip was found to have more uniform inflow velocity distribution along the radial direction. This could be explained as follows. The radial variation in bound circulation gives rise to trailing vortices, which in turn influence the induced flow. A smoother radial distribution of bound vortices imply weaker trailing vortices, which in turn imply a smoother induced velocity distribution. From Calculus of Variations, at a given thrust level, the kinetic energy dumped into the wake is the lowest when the inflow is uniform. As a result, induced power is the least for anhedral planforms at a given thrust level.

5. There is a point of diminishing return as the anhedral angle is progressively increased. No significant improvement in the figure of merit was observed above an anhedral angle of 20 degrees.
6. In forward flight, the anhedral tip and the baseline rotor both behaved similarly. The inflow velocity distribution at selected time levels, the tip vortex structures and strength, and the total power as a function of the thrust setting were comparable.

7.2 Recommendations for Future Work

Based on the computational studies and conclusions, the following recommendations are made for future research:

1. Because of the large number of simulations needed (three blade planforms, 5 to 10 thrust settings), all the wake capturing calculations were done on a 22 Million point engineering quality grid. Follow-on studies on denser grids for a selected subset of these cases would yield better captured wake structures, and may yield additional insight into the flow phenomena.
2. In the present studies, the flow was assumed to be fully turbulent. Future studies should include the effects of transition.
3. The present calculations were limited to rotors in hover and forward flight at a single advance ratio $\mu = 0.25$. The blades were assumed to be rigid. It would be interesting to conduct forward flight studies with over a broad range of advance ratios. It is also recommended that the elastic effects be included to assess the effects of anhedral on power consumption, and vibratory loads. It would also be

interesting to study descent flight to explore how the anhedral changes the BVI phenomena that invariably arise during descent.

4. Finally, the effects of rotor planform on rotor noise must be studied in hover, forward flight, and in descent, and further more optimization of the blade made.

APPENDIX A GT-HYBRID METHODOLOGY

GT-Hybrid is a three-dimensional unsteady viscous compressible flow solver. The flow is modeled by first principles using the Navier-Stokes methodology. GT-Hybrid solves the three-dimensional unsteady Navier-Stokes equations in the transformed body-fitted coordinate system using a time-accurate, finite volume scheme.

The Navier-Stokes equations in transformed generalized curvilinear coordinate system are given as

$$\frac{\partial \hat{q}}{\partial \tau} + \frac{\partial\left(\hat{E} - \hat{R}\right)}{\partial \xi} + \frac{\partial\left(\hat{F} - \hat{S}\right)}{\partial \eta} + \frac{\partial\left(\hat{G} - \hat{T}\right)}{\partial \zeta} = 0, \tag{A. 1}$$

where ξ denotes the chord-wise direction, η denotes the radial direction and ζ the normal direction. is the flow vector, represented as

$$\hat{q} = J^{-1}\begin{Bmatrix} \rho \\ \rho u \\ \rho v \\ \rho w \\ e \end{Bmatrix} \tag{A.2}$$

The inviscid flux vector is defined as follows,

$$\hat{E} = J^{-1}\begin{Bmatrix} \rho U \\ \rho u U + \xi_x p \\ \rho v U + \xi_y p \\ \rho w U + \xi_z p \\ (e+p)U - \xi_t p \end{Bmatrix} \tag{A.3}$$

where *J* is Jacobian and *u,v,w* are the Cartesian components of velocity in an inertial coordinate system. Also, *e* is the total energy per unit volume and pressure *p* is given by the equation of state as follows:

$$p = (\gamma - 1)\left\{e - \rho\left(\frac{u^2 + v^2 + w^2}{2}\right)\right\} \tag{A.4}$$

The contravariant velocities *U, V, W* in the flux vectors are related to the grid metrics.

$$U = \xi_t + \xi_x(u - x_\tau) + \xi_y(v - y_\tau) + \xi_z(w - z_\tau)$$

$$V = \eta_t + \eta_x(u - x_\tau) + \eta_y(v - y_\tau) + \eta_z(w - z_\tau)$$

$$W = \zeta_t + \zeta_x(u - x_\tau) + \zeta_y(v - y_\tau) + \zeta_z(w - z_\tau) \tag{A.5}$$

where x_τ, y_τ, z_τ represent the motion of the grid relative to the inertial coordinate system (*x,y,z*). The viscous flux vector is given by,

$$\hat{R} = \boldsymbol{J^{-1}} \begin{Bmatrix} 0 \\ \xi_x \tau_{xx} + \xi_y \tau_{xy} + \xi_z \tau_{xz} \\ \xi_x \tau_{yx} + \xi_y \tau_{yy} + \xi_z \tau_{yz} \\ \xi_x \tau_{zx} + \xi_y \tau_{zy} + \xi_z \tau_{zz} \\ \xi_x \beta_x + \xi_y \beta_y + \xi_z \beta_z \end{Bmatrix}$$

$$\hat{S} = \boldsymbol{J^{-1}} \begin{Bmatrix} 0 \\ \eta_x \tau_{xx} + \eta_y \tau_{xy} + \eta_z \tau_{xz} \\ \eta_x \tau_{yx} + \eta_y \tau_{yy} + \eta_z \tau_{yz} \\ \eta_x \tau_{zx} + \eta_y \tau_{zy} + \eta_z \tau_{zz} \\ \eta_x \beta_x + \eta_y \beta_y + \eta_z \beta_z \end{Bmatrix}$$

$$\hat{T} = \boldsymbol{J^{-1}} \begin{Bmatrix} 0 \\ \zeta_x \tau_{xx} + \zeta_y \tau_{xy} + \zeta_z \tau_{xz} \\ \zeta_x \tau_{yx} + \zeta_y \tau_{yy} + \zeta_z \tau_{yz} \\ \zeta_x \tau_{zx} + \zeta_y \tau_{zy} + \zeta_z \tau_{zz} \\ \zeta_x \beta_x + \zeta_y \beta_y + \zeta_z \beta_z \end{Bmatrix} \qquad \text{(A.6)}$$

By assuming Stokes hypothesis (λ = -2/3μ), the shear terms are written as

$$\tau_{xx} = -\frac{2}{3}\mu\left(u_x + v_y + w_z\right) + 2\mu u_x$$

$$\tau_{yy} = -\frac{2}{3}\mu\left(u_x + v_y + w_z\right) + 2\mu v_y$$

$$\tau_{zz} = -\frac{2}{3}\mu\left(u_x + v_y + w_z\right) + 2\mu w_z$$

$$\tau_{xy} = \tau_{yx} = \mu(u_y + v_x)$$

$$\tau_{yz} = \tau_{zy} = \mu(v_z + w_y)$$

$$\tau_{zx} = \tau_{xz} = \mu(w_x + u_z)$$

$$\beta_x = u\tau_{xx} + v\tau_{xy} + w\tau_{xz} + k\left(\xi_x \frac{\partial T}{\partial \xi} + \eta_x \frac{\partial T}{\partial \eta} + \zeta_x \frac{\partial T}{\partial \zeta}\right)$$

$$\beta_y = u\tau_{xy} + v\tau_{yy} + w\tau_{yz} + k\left(\xi_y \frac{\partial T}{\partial \xi} + \eta_y \frac{\partial T}{\partial \eta} + \zeta_y \frac{\partial T}{\partial \zeta}\right)$$

$$\beta_z = u\tau_{xz} + v\tau_{yz} + w\tau_{zz} + k\left(\xi_z \frac{\partial T}{\partial \xi} + \eta_z \frac{\partial T}{\partial \eta} + \zeta_z \frac{\partial T}{\partial \zeta}\right) \quad \text{(A.7)}$$

where k is the coefficient of thermal conductivity, and μ is the dynamic viscosity.

A.1 Spatial Discretization

Equation (A.1) is discretized using a semi-discrete finite difference approximation in three dimensions as

$$\left(\frac{\partial \hat{q}}{\partial \tau}\right)_{i,j,k} + \frac{\hat{E}_{i+\frac{1}{2},j,k} - \hat{E}_{i-\frac{1}{2},j,k}}{\Delta\xi} + \frac{\hat{F}_{i,j+\frac{1}{2},k} - \hat{F}_{i,j-\frac{1}{2},k}}{\Delta\eta} + \frac{\hat{G}_{i,j,k+\frac{1}{2}} - \hat{G}_{i,j,k-\frac{1}{2}}}{\Delta\zeta} = \frac{\hat{R}_{i+\frac{1}{2},j,k} - \hat{R}_{i-\frac{1}{2},j,k}}{\Delta\xi} + \frac{\hat{S}_{i+\frac{1}{2},j,k} - \hat{S}_{i-\frac{1}{2},j,k}}{\Delta\xi} + \frac{\hat{T}_{i+\frac{1}{2},j,k} - \hat{T}_{i,j,k-\frac{1}{2}}}{\Delta\zeta} \quad \text{(A.8)}$$

where

$$\Delta\xi = \xi_{i+\frac{1}{2},j,k} - \xi_{i-\frac{1}{2},j,k} = 1$$

$$\Delta\eta = \eta_{i,j+\frac{1}{2},k} - \eta_{i,j-\frac{1}{2},k} = 1 \qquad \text{(A.9)}$$

$$\Delta\zeta = \zeta_{i,j,k+\frac{1}{2}} - \zeta_{i,j,k-\frac{1}{2}} = 1$$

A.1.1 *Computation of Inviscid Fluxes*

The inviscid fluxes *E, F, G* above represent the fluxes in mass, momentum and energy respectively. Solutions to NS equations encompass acoustic, vortical and entropy waves. A variety of flux-vector splitting and flux-difference splitting schemes split the flux terms based on contributions from the individual waves. In the current work, Roe's approximate solver is used in the inviscid flux vector splitting. $\hat{E}$ is computed as

$$\hat{E}_{i+\frac{1}{2},j,k} = \frac{1}{2}\left\{\left(\hat{E}_L + \hat{E}_R\right) - \left|\hat{A}\right|(q_R - q_L)\right\} \qquad \text{(A.10)}$$

where, $q_R$is set equal to the value of q just to the right of the $\left(i \pm \frac{1}{2}, j, k\right)$ node and q_L is set to the value of q just to the left of $\left(i \pm \frac{1}{2}\ or\ j \pm \frac{1}{2}\ or\ k \pm \frac{1}{2}\right)$ node. The fluxes $\hat{E}_L$ and $\hat{E}_R$are evaluated at the half node $\left(i \pm \frac{1}{2}, j, k\right)$ using the flow properties from the left and the right of the cell face, which are given as

$$\hat{E}_L = \begin{Bmatrix} \rho_L U_L \\ \rho_L u_L U_L + \eta_x p_L \\ \rho_L v_L U_L + \eta_y p_L \\ \rho_L w_L U_L + \eta_z p_L \\ \rho_L U_L h_{0L} - \eta_t p_L \end{Bmatrix}, \hat{E}_R = \begin{Bmatrix} \rho_R U_R \\ \rho_R u_R U_R + \eta_x p_R \\ \rho_R v_R U_R + \eta_y p_R \\ \rho_R w_R U_R + \eta_z p_R \\ \rho_R U_R h_{0R} - \eta_t p_R \end{Bmatrix}. \tag{A.11}$$

The quantities U, h_0 and η_t are contravariant velocity, specific total enthalpy and the grid velocity of the coordinate surface $(i+\frac{1}{2}, j, k)$ in the normal direction of the surface, respectively. The term $|\hat{A}|(q_R - q_L)$ in Equation. (A.12) represents the numerical viscosity term as computed by the approach presented by Vinokur and Liu [94], where

$$\left|\hat{A}\right|(q_R - q_L) = \left|\tilde{\lambda}_1\right| \begin{Bmatrix} \Delta\rho \\ \Delta\rho u \\ \Delta\rho v \\ \Delta\rho w \\ \Delta e \end{Bmatrix} + \delta_1 \begin{Bmatrix} \tilde{\rho} \\ \tilde{\rho}\tilde{u} \\ \tilde{\rho}\tilde{v} \\ \tilde{\rho}\tilde{w} \\ \tilde{\rho}\tilde{h}_0 \end{Bmatrix} + \delta_2 \begin{Bmatrix} 0 \\ \eta_x \\ \eta_y \\ \eta_z \\ \tilde{U}_c \end{Bmatrix} \tag{A.12}$$

$$\delta_1 = C_1 \tilde{\rho} \Delta U_c + \frac{1}{2} C_2 \frac{\Delta p}{\tilde{a}}$$

$$C_1 = -\left|\tilde{\lambda}_1\right| + 0.5\left(\left|\tilde{\lambda}_2\right| + \left|\tilde{\lambda}_3\right|\right) \tag{A.13}$$

$$C_2 = -\left|\tilde{\lambda}_2\right| - \left|\tilde{\lambda}_3\right|$$

The operator Δ is defined as a jump across the cell face. The characteristic wave speeds are given by:

$$\tilde{\lambda}_1 = \widetilde{U}$$

$$\tilde{\lambda}_2 = \widetilde{U} + a \tag{A.14}$$

$$\tilde{\lambda}_3 = \widetilde{U} - a$$

All the "Roe-averaged" quantities are denoted by tilde sign, and are given by

$$R = \sqrt{\frac{\rho_R}{\rho_L}}$$

$$\tilde{\rho} = \sqrt{\rho_R \rho_L}$$

$$\tilde{u} = u_L\left(\frac{1}{1+R}\right) + u_R\left(\frac{R}{1+R}\right)$$

$$\tilde{v} = v_L\left(\frac{1}{1+R}\right) + v_R\left(\frac{R}{1+R}\right)$$

$$\widetilde{w} = w_L\left(\frac{1}{1+R}\right) + w_R\left(\frac{R}{1+R}\right) \tag{A.15}$$

$$\tilde{e} = e_L\left(\frac{1}{1+R}\right) + e_R\left(\frac{R}{1+R}\right)$$

$$\tilde{u} = u_L\left(\frac{1}{1+R}\right) + u_R\left(\frac{R}{1+R}\right)$$

$$\tilde{a} = \sqrt{\gamma(\gamma-1)\left[\frac{e}{\rho} - \frac{1}{2}(\tilde{u}^2 + \tilde{v}^2 + \widetilde{w}^2)\right]}$$

In the current implementation, the Monotone Upstream Centered Scheme for Conservation Laws (MUSCL) [95] is used. The MUSCL scheme is given as:

$$q_L = \left\{1 + \frac{[(1-k)\nabla + (1+k)\Delta]}{4}\right\} q_i$$

$$q_R = \left\{1 - \frac{[(1+k)\nabla + (1-k)\Delta]}{4}\right\} q_{i+1} \tag{A.16}$$

where Δ and ∇ are the forward and backward difference operators, respectively.

The choice of parameter k determines the spatial accuracy of the scheme. The value of k = -1 yields a second-order fully upwind scheme, while k = 1 yields a second-order central difference scheme. In the present work, k = $\frac{1}{3}$ yields a third-order accurate upwind scheme.

In regions of large gradients and discontinuities, a high-order scheme must be reduced to a lower order to maintain stability and to restrict numerical oscillations in the solution. This may be accomplished by employing a flux limiter. A limiter is defined as a nonlinear algorithm that reduces the high-derivative content of a subgrid interpolant in order to make it non-oscillatory [96]. In the present methodology, the alternative form of Van Albada flux limiter [97] typically used in high order spatial schemes is used. It is defined as follows:

$$\varphi = \frac{2r}{r^2 + 1} \tag{A.17}$$

where *r* represents the ratio of the successive gradients on the flow solution, i.e.,

$$r_i = \frac{\nabla q_i}{\Delta q_i} = \frac{q_i - q_{i-1}}{q_{i+1} - q_i}. \tag{A.18}$$

Thus, the flux limiter is implemented as

$$\varphi^l = \frac{2(\nabla q_i)(\Delta q_i) + \varepsilon}{(\nabla q_i)^2 + (\Delta q_i)^2 + \varepsilon}$$
$$\varphi^r = \frac{2(\nabla q_{i+1})(\Delta q_{i+1}) + \varepsilon}{(\nabla q_{i+1})^2 + (\Delta q_{i+1})^2 + \varepsilon} \tag{A.19}$$

where ε is a parameter that ensures there is no indeterminancy in regions of zero gradients.

A.1.2 *Computation of Viscous Fluxes*

The viscous fluxes R, S, T are computed using a symmetric second order central difference scheme. The viscous fluxes contain derivatives of the velocity components, such as u_ξ which is computed as,

$$u_\xi|_{i+\frac{1}{2},j,k} = \frac{u_{i+1,j,k} - u_{i,j,k}}{\Delta\xi}, \qquad u_\xi|_{i-\frac{1}{2},j,k} = \frac{u_{i,j,k} - u_{i-1,j,k}}{\Delta\xi} \tag{A.20}$$

A.1.3 *Temporal Discretization*

With the above discretizations, the Navier-Stokes equations are expressed as follows:

$$\hat{q}^{n+1} = \hat{q}^{n} - \Delta\tau\left(\delta_{\xi}\hat{E} + \delta_{\eta}\hat{F} + \delta_{\zeta}\hat{G}\right)\Big|^{n+1} + \Delta\tau\frac{M}{Re}\left(\delta_{\xi}\hat{R} + \delta_{\xi}\hat{S} + \delta_{\xi}\hat{T}\right)\Big|^{n} \tag{A.21}$$

where the superscripts refer to the time levels 'n' and '$n+1$'. The semi-implicit time marching scheme with first-order backward differencing is used to advance the governing parabolic equations. The operators $\delta_{\xi}, \delta_{\eta}, \delta_{\zeta}$ are the standard central difference operators. The inviscid and viscous fluxes are computed at the half-points.

Note that the vector $\hat{q}$ contains the Jacobian term which is not a constant for deforming grids. The above discretization yields a nonlinear system of algebraic equations for the unknown flow properties. The non-linear fluxes are linearized by performing a Taylor series expansion, so that

$$\begin{aligned} \hat{E}^{n+1} &= \hat{E}^{n} + [A^{n}](\hat{q}^{n+1} - \hat{q}^{n}) \\ \hat{G}^{n+1} &= \hat{G}^{n} + [B^{n}](\hat{q}^{n+1} - \hat{q}^{n}) \\ \hat{H}^{n+1} &= \hat{H}^{n} + [C^{n}](\hat{q}^{n+1} - \hat{q}^{n}) \end{aligned} \tag{A.22}$$

where the quantities $[A^{n}]$, $[B^{n}]$ and $[C^{n}]$ are 5×5 flux Jacobian matrices, defined as:

$$A = \frac{\partial \hat{E}}{\partial \hat{q}}; \quad B = \frac{\partial \hat{F}}{\partial \hat{q}}; \quad C = \frac{\partial \hat{G}}{\partial \hat{q}} \tag{A.23}$$

The Jacobian matrices are given by Pulliam and Steger [98]. First,

$$\boldsymbol{A} = \begin{bmatrix} \xi_t & \xi_x & \xi_y & \xi_z & 0 \\ -u\theta + \xi_x\varphi^2 & \Theta - (\gamma-2)\xi_x u & \xi_y u - \sigma\xi_x v & \xi_z u - \sigma\xi_x w & \sigma\xi_x \\ -v\theta + \xi_y\varphi^2 & \xi_x v - \sigma\xi_y u & \Theta - (\gamma-2)\xi_y v & \xi_z v - \sigma\xi_y w & \sigma\xi_y \\ -w\theta + \xi_z\varphi^2 & \xi_x w - \sigma\xi_z u & \xi_y w - \sigma\xi_z v & \Theta - (\gamma-2)\xi_z w & \sigma\xi_z \\ \theta(\varphi^2 - E) & \xi_x E - \sigma u\theta & \xi_y E - \sigma v\theta & \xi_z E - \sigma w\theta & \xi_t + \gamma\theta \end{bmatrix}$$

$$\varphi^2 = (\gamma - 1)\left(\frac{u^2 + v^2 + w^2}{2}\right)$$

$$\theta = \xi_x u + \xi_y v + \xi_z w$$

$$\sigma = \gamma - 1$$

$$\Theta = \xi_t + \theta$$

$$E = \frac{\gamma e}{\rho} - \varphi^2$$

Then, the matrices [B] and [C] are evaluated in terms of the respective generalized coordinates η and ζ. Eq. (A.21) can be rearranged as:

$$\left[I + \Delta\tau\left(\delta_\xi \hat{A}^n + \delta_\eta \hat{B}^n + \delta_\zeta \hat{C}^n\right)\right]\Delta\hat{q}^{n+1} = [RHS]^n \tag{A.24}$$

where $\Delta\hat{q}^{n+1} = \hat{q}^{n+1} - \hat{q}^{n}$, and I is the identity matrix. The term [RHS], referred to as the residual, is given by:

$$[RHS]^n = -\Delta\tau(\delta_\xi \hat{F}^n + \delta_\eta \hat{G}^n + \delta_\zeta \hat{H}^n) + \Delta\tau \frac{M}{\mathrm{Re}}(\delta_\xi \hat{R}^n + \delta_\eta \hat{S}^n + \delta_\zeta \hat{T}^n) \tag{A.25}$$

A second order temporal accuracy version of the current temporal scheme is also available, which uses Newton sub-iterations denoted by superscript 'l'.

$$\begin{aligned}[RHS]^{n+1,l} = &-\Delta\tau\left(\delta_\xi \hat{F}^{n+1,l} + \delta_\eta \hat{G}^{n+1,l} + \delta_\zeta \hat{H}^{n+1,l}\right) \\ &+ \Delta\tau \frac{M}{Re}\left(\delta_\xi \hat{R}^{n+1,l} + \delta_\eta \hat{T}^{n+1,l} + \delta_\zeta \hat{F}^{n+1,l}\right) \\ &- \frac{(3\hat{q}^{n+1,l} - 4\hat{q}^{n} + \hat{q}^{n-1,l})}{2}\end{aligned} \tag{A.26}$$

In this context, $\hat{q}^{n+1,l}$ is the latest estimate of $\hat{q}$ at new time level $n+1$, and a previous sub-iteration l.

In Eq. (A.23), then $\Delta\hat{q}^{n+1}$ is viewed as

$$\Delta\hat{q}^{n+1} = \hat{q}^{n+1,l+1} - \hat{q}^{n+1,l} \tag{A.27}$$

In steady-state problems, the residual $\Delta\hat{q}$ should be reduced to an acceptably small value for the calculation to be considered converged. In time dependent or unsteady problems, however, the residual does not need to reach a minimum value and may vary

with time depending on the flow situation. Equation (A.25) may be viewed as a matrix system,

$$[M]\{\Delta\hat{q}\} = [RHS] \tag{A.28}$$

Solution of Eq. (A.28) is computationally expensive because the unfactored coefficient matrix [*M*], which is a seven-diagonal matrix, requires vast computer storage and computing time to invert. In order to reduce the computational work, this sparse matrix [*M*] is approximately factored into three sparse matrices using a Lower-Upper Symmetric Gauss-Seidel (LU-SGS) implicit scheme proposed by Yoon and Jameson [99]. The LU-SGS method ensures that the matrix is diagonally dominant. This scheme is widely used to solve the compressible Navier-Stokes equations.

A.2 Geometric Conservation Law

The geometric conservation law (GCL) is used to satisfy the conservative relations of the surfaces and volumes of the control cells. In moving meshes, the GCL states that the volumetric increment of a moving cell must be equal to the sum of the changes along the surfaces that enclose the volume. Thomas and Lombard [100] formulated the differential form of the geometric conservation law. The GCL terms can be identified from the differential form of the Navier-Stokes equations in generalized coordinates.

The differential form of the Navier Stokes equations may be expressed as

$$\frac{\partial VQ}{\partial t} + \frac{\partial \hat{F}}{\partial \xi} + \frac{\partial \hat{G}}{\partial \eta} + \frac{\partial \hat{H}}{\partial \zeta} = \frac{M}{\mathrm{Re}}\left[\frac{\partial \hat{R}}{\partial \xi} + \frac{\partial \hat{S}}{\partial \eta} + \frac{\partial T}{\partial \zeta}\right] \tag{A.29}$$

Where V is the cell volume is

$$V = \frac{1}{J}$$

This can be expressed as

$$\frac{V\partial Q}{\partial t} + \frac{Q\partial V}{\partial t} + \frac{\partial \hat{F}}{\partial \xi} + \frac{\partial \hat{G}}{\partial \eta} + \frac{\partial \hat{H}}{\partial \zeta} = \frac{M}{Re}\left[\frac{\partial \hat{R}}{\partial \xi} + \frac{\partial \hat{S}}{\partial \eta} + \frac{\partial T}{\partial \zeta}\right] \tag{A.30}$$

The term $Q\frac{\partial V}{\partial t}$ is known as the GCL term and can be expressed in term of generalized coordinates as

$$Q\frac{\partial V}{\partial t} = -Q\left[\frac{\partial}{\partial \xi}\left(\frac{\xi_t}{J}\right) + \frac{\partial}{\partial \eta}\left(\frac{\eta_t}{J}\right) + \frac{\partial}{\partial \zeta}\left(\frac{\zeta_t}{J}\right)\right] \tag{A.31}$$

The refined governing equation accounting for GCL term becomes

$$\frac{1}{\mathrm{J}}\frac{\partial Q}{\partial \mathrm{t}} + \frac{\partial F}{\partial \xi} + \frac{\partial G}{\partial \eta} + \frac{\partial G}{\partial \zeta} = \frac{\partial R}{\partial \xi} + \frac{\partial S}{\partial \eta} + \frac{\partial T}{\partial \zeta} + \mathrm{RHS_{GCL}} \tag{A.32}$$

where

$$\mathrm{RHS_{GCL}} = Q\left[\frac{\partial}{\partial \xi}\left(\frac{\xi_t}{J}\right) + \frac{\partial}{\partial \eta}\left(\frac{\eta_t}{J}\right) + \frac{\partial}{\partial \zeta}\left(\frac{\zeta_t}{J}\right)\right]$$

A.3 Boundary and Interface Conditions

At the surface of the blade, the solid wall, no-slip, and adiabatic wall boundary conditions and zero pressure gradient at the wall are applied as follows:

$$\vec{V}_{wall} = \vec{V}_{grid} \qquad \text{No slip boundary condition}$$

$$\left.\frac{\partial T}{\partial n}\right|_{wall} = 0$$

$$\left.\frac{\partial p}{\partial n}\right|_{wall} = 0$$

The boundary conditions must be formulated to keep the solution physical and prevent any non-physical reflection at the boundary. The upstream and downstream Riemann invariants imposed at the far-field boundary are given by

$$R^{+} = \vec{V}_n + \frac{2a}{\gamma - 1}$$
$$R^{-} = \vec{V}_n - \frac{2a}{\gamma - 1} \tag{A.33}$$

The Riemann invariants correspond to the incoming R^{-} and outgoing R^{+} characteristic waves. Eigen values associated with the characteristic velocities are given by

$$\lambda_1 = \vec{V}_n + a \tag{A.34}$$

$$\lambda_2 = \vec{V}_n - a$$

The normal velocity vector $\vec{V}_n$ is outwardly directed from the interior computational domain. The velocity at the outer boundary consists of free-stream velocity, velocity component due to grid movement, and the induced velocity due to all the wake filaments and boundary vorticity from other blades. When $\vec{V}_n$ is negative, λ_2 is negative as well and therefore the inflow condition is applied. In such a case, if λ_1 is also negative, all the information comes from the free-stream. On the other hand, if λ_1 is positive, one piece of information comes from the interior and the others come from the free-stream. At the far-field, inboard and outboard surfaces, the characteristics based inflow/outflow boundary condition which are non-reflective are used.

A.4 Turbulence Model

In order to predict turbulent flows by numerical solutions to the Reynolds equations, it is necessary to make closing assumptions about the apparent turbulent stress. The Reynolds stress terms $\overline{u_i' u_j'}$, cannot be solved directly and therefore are modeled. Boussinesq assumption states that the apparent turbulent shearing stresses are related to the rate of the mean strain through an "eddy" viscosity concept, which is represented in the tensor form as:

$$-\rho\overline{u_i' u_j'} = \mu_T \left[\frac{\partial \overline{u}_i}{\partial x_j} + \frac{\partial \overline{u}_j}{\partial x_i}\right] \tag{A.35}$$

where μ_T is the turbulent viscosity, u_i', u_j' are the instantaneous velocity fluctuations about the mean velocity components $\overline{u}_i$ and $\overline{u}_j$ respectively and $\overline{u_i'u_j'}$ is the time-averaged value of the product u_i' and u_j'. The turbulence models currently implemented in the hybrid CFD solver are Spalart-Allmaras (SA) [101], Spalart-Allmaras-DES (SA-DES) [102], and Kinetic Eddy Simulation (KES) [103], [104].

A.4.1 *Spalart Allmaras Model*

Some of the key features of the SA model are described. The SA model uses the Boussinesq approximation to relate the Reynolds stresses to a kinematic turbulent eddy viscosity and the mean strain-rate tensor.

$$\nu_t = \tilde{\nu} f_{v1} \tag{A.36}$$

The transport equation for the variable $\tilde{\nu}$ is given by

$$\frac{D\tilde{\nu}}{Dt} = \underbrace{C_{b1}\tilde{\nu}\left(\Omega + \frac{\tilde{\nu}}{k^2 d^2} f_{v2}\right)}_{\text{Production}} - \underbrace{C_{w1} f_w \left(\frac{\tilde{\nu}}{d}\right)^2}_{\text{Dissipation}} + \underbrace{\frac{1}{\sigma}\left[\nabla \cdot \left((\nu + \tilde{\nu})\nabla\tilde{\nu}\right) + C_{b2}(\nabla\tilde{\nu})^2\right]}_{\text{Diffusion}} \tag{A.37}$$

The terms on the right hand side consist of the source terms for production, dissipation and diffusion. The turbulent length scale d is defined as the distance to the nearest wall. The functions f_{v1}, f_{v2}, f_w and the model constants $C_{b1}, C_{b1}, C_{b1}, k, \sigma$ are described in detail by Spalart and Allmaras [101]. Ω represents the magnitude of vorticity.

A.4.2 *Spalart-Allmaras Detached Eddy Simulation (SA-DES)*

For modeling separated flows, an extension to the SA model has been proposed by Spalart [102] which blends the RANS turbulence model in boundary layers, together with coarse-mesh LES in regions of separated flow. This approach is called the SA-DES model. Within the boundary layer, the turbulent scales are very small and need to be modeled, and therefore the DES model operates in RANS mode. Outside the boundary layer, SA-DES switches to an LES-type model, where the turbulence scales are well resolved by the grid. In regions away from the wall, this definition is replaced by the maximum cell size as follows:

$$\tilde{d} = \min(d, C_{DES}\Delta) \tag{A.38}$$

where $\Delta = \max(\Delta x, \Delta y, \Delta z)$. The model constant used in this study is $C_{DES} = 0.65$.

A.4.3 *Menter's k-ω-SST Model*

Menter's k- ω -SST model [100] solves the two equations for k (turbulent kinetic energy) and ω (specific turbulent dissipation rate). Near the walls, k- ω -SST model solves the k- ω equations that do not require any near wall damping functions. Away from walls, the k –ω -SST model switches over to the k-ε equations which do not suffer from the free stream dependency found in the k- ω model. The following equations are solved:

$$\frac{\partial \rho k}{\partial t}+\frac{\partial \rho u_i k}{\partial x_j}=\underbrace{\tau_{ij}\frac{\partial u_i}{\partial x_j}}_{\text{Production term}}-\underbrace{\frac{k^{\frac{3}{2}}}{l}}_{\text{Dissipation term}}+\underbrace{\frac{\partial}{\partial x_j}\left[(\mu+\frac{\mu_t}{\sigma_k})\frac{\partial k}{\partial x_j}\right]}_{\text{Diffusion term}}$$

$$\frac{\partial \rho \omega}{\partial t}+\frac{\partial \rho u_i \omega}{\partial x_j}=\overbrace{\frac{\gamma}{\upsilon_t}\tau_{ij}\frac{\partial u_i}{\partial x_j}}-\overbrace{\beta\rho\omega^2}+\overbrace{\frac{\partial}{\partial x_j}\left[(\mu+\frac{\mu_t}{\sigma_\omega})\frac{\partial \omega}{\partial x_j}\right]}+\underbrace{2(1-F_1)\rho\sigma_{\omega 2}\frac{1}{\omega}\frac{\partial k}{\partial x_j}\frac{\partial \omega}{\partial x_j}}_{\text{Cross-diffusion term}} \tag{A.39}$$

These equations are expressed in the curvilinear coordinate system the same way the mean flow transport equations are cast. A first order accurate time marching scheme is used. A first order upwind scheme is used for the transport of k and ω. The diffusion terms are computed using second order accurate central differences in the transformed plane. The length scale is computed from

$$l=\frac{\sqrt{k}}{\beta^*\omega} \tag{A.40}$$

The following empirical constants and functions are used:

$$\begin{aligned}&\sigma_{k1}=1/0.85,\ \sigma_{\omega 1}=1/0.5,\ \beta_1=0.075\\&\beta^*=0.09,\ \kappa=0.41,\ \gamma_1=\frac{\beta_1}{\beta^*}-\frac{\kappa^2}{\sigma_{\omega 1}\sqrt{\beta^*}}\end{aligned} \tag{A.41}$$

$$\sigma_{k2} = 1.0,\ \sigma_{\omega 2} = 1/0.856,\ \beta_2 = 0.0828$$

$$\beta^* = 0.09,\ \kappa = 0.41,\ \gamma_2 = \frac{\beta_2}{\beta^*} - \frac{\kappa^2}{\sigma_{\omega 2}\sqrt{\beta^*}}$$

$$CD_{k\omega} = \max[2\rho\sigma_{\omega 2}\frac{1}{\omega}\frac{\partial k}{\partial x_j}\frac{\partial \omega}{\partial x_j};10^{-20}] \tag{A.42}$$

$$F_1 = \tanh((\min[\max[\frac{2\sqrt{k}}{\beta^*\omega y};\frac{500\nu}{y^2\omega}];\frac{4\rho\sigma_{\omega 2}k}{CD_{k\omega}y^2}])^4)$$

$$\varphi = F_1 * \varphi_{1+} (1-F_1) * \varphi_2$$

The eddy viscosity is computed from

$$\mu_t = \frac{a_1 \rho k}{\max(a_1\omega;\Omega F_2)}$$

Where a_1=0.3

A.5 Rotor Inflow Modeling

In low speed operations, the rotor flow environment is strongly modified by the interaction between the rotor blade and the vortices shed from the neighboring blades. The ability to predict this wake is important, especially for blade-vortex interactions (BVI) in forward flight. In addition to the near wake, the rotor far wake that extends up to 4-6 rotor

diameters needs to be captured or modeled to accurately predict the rotor inflow field. The requirement that the vortex core in the far wake be resolved without dissipation can make CFD wake capturing methods like OVERFLOW computationally expensive. GT-Hybrid CFD solver utilizes a hybrid methodology where the flow field near the blade is resolved through the Navier-Stokes solution, whereas the influence of the other blades and of the trailing vorticity in the far field wake are accounted for by modeling them as a collection of piece-wise linear bound and trailing vortex elements. The near wake is captured inherently in the Navier-Stokes analysis. The use of such a hybrid Navier-Stokes/vortex modeling method allows for an accurate and economical modeling of viscous features near the blades, and an accurate "non-diffusive" modeling of the trailing wake in the far field.

A.5.1 *Rigid/Free Wake Model*

The vortex model is based on a Lagrangian wake approach where a collection of vortex elements are shed from the rotor blade trailing edge. This wake model is based on the assumption that all shed vorticity from blade coalesce downstream into a strong tip vortex. The convection of the tip vortex elements depends on differing approaches – rigid wake or free wake model. In the rigid wake model, the wake elements are non-distorting hence they maintain their initial helical structure and they are convected at a speed determined by linear superposition of free stream velocity components and a uniform inflow velocity. This inflow velocity is determined using the Prandtl-Glauert's formula [105]. The convection velocity components in free/distorting wake model include velocity components induced by wake elements on each other in addition to above mentioned velocity components. The effect of bound vortex is also included for computation of self-induced velocity components. These self-induced velocity components are determined

using the Biot-Savart law. Free wake methods provide more generality with a minimum dependence on experimental data but they are also computationally more expensive than rigid wake modeling.

In the current implementation, the free/rigid wake model is initialized with prescribed wake geometry. The wake strengths are initialized using an analytical model developed by Mello *et al.* [106]. The number of revolutions of the wake preserved in the model is chosen by the user. In forward flight, 3 to 5 wake revolutions are chosen, depending on the advance ratio. In the hybrid method, the wake strength and geometry are assumed to vary periodically with blade azimuthal location. New wake filaments are added at the vortex shedding point as the rotor is advanced in the azimuthal direction. To keep the fixed number of wake elements small, the oldest elements are dropped from the end of the wake. The induced velocity components and wake geometry distortion are updated for all wake elements each time new wake filaments are shed. Also, in order to reduce the computational cost, the frequency of updating the wake distortion can be controlled, permitting induced velocity and wake geometry updates at periodic azimuthal intervals. The free wake model is a better physical representation of the wake than a rigid wake model, and therefore it is used for all the studies presented in this work.

A.5.2 *Navier-Stokes/Wake Model Coupling*

The wake model derives its vortex strength from the Navier-Stokes solutions. The effect of the wake model on the Navier-Stokes solution is accounted for by applying wake induced velocity components as a boundary condition on the Navier-Stokes far-field boundaries. This coupling between the Navier-Stokes solution and the wake model is explicit in nature. The effect of the wake lags the Navier-Stokes solution. The strength of

the vortex elements in the tip vortex is set to be equal to the peak bound circulation on the rotor blade at the instant the element is shed. The peak bound circulation is obtained from airloads predicted by Navier-Stokes solution using the Kutta-Joukowski theorem. The shedding point of the vortex element is based on the centroid of trailed circulation between the tip and location of peak bound circulation. The wake induced velocity components are computed at domain boundary points using the Biot-Savart law. The wake trailers used for boundary condition computation includes trailing and bound wake from all blades but neglects the contribution of the elements within the CFD volume grid trailed immediately from the blade. It is necessary to exclude the wake trailers inside the CFD volume grid to avoid double counting the vorticity already captured by the Navier-Stokes solution. An imaginary bounding box is used to determine whether a wake marker is inside or outside the Navier-Stokes domain. The induced velocity of the wake trailers inside the bounding box is not considered.

A.6 Multiple Trailer Wake Model

The wake model represented by a single concentrated tip vortex trailing from a region near the blade tip assumes that all inboard wake is either weak or coalesces into the tip vortex immediately that the effect of inboard wake can be easily ignored. This assumption would be appropriate for high speed flight but would be physically less accurate for rotors in low speed forward and descent flight since location and strength of the inboard vortices are critical for predicting blade vortex interaction (BVI) phenomena. To address this issue, a full-span wake model or multiple trailer wake model is available in the GT-Hybrid solver as an alternative to the tip vortex model. The multiple trailer wake

model is based on Prandtl's lifting-line theory [107]. For a three-dimensional blade, the bound vorticity, located at quarter chord line of the blade is trailed into the wake from the blade tip and root. Vorticity is also shed from the blade mid-span regions because of radial changes in the bound circulation. Therefore, the single tip vortex is replaced by user specified number of multiple vortex segments trailed from all the blades. The trailers are equally distributed along the blade span. The strength of the vortex elements is based on radial gradient of bound circulation and number of wake trailers chosen by the user. The vorticity strength of first wake element of trailer *n* at any azimuthal position Ψ is given by

$$\Gamma_{tr}(\Psi, n) = \Gamma(\Psi, n+1) - \Gamma(\Psi, n) \tag{A.43}$$

The geometry of the far wake undergoes distortion due to the influence of the self-induced velocity components and also due to the time rate of change in circulation of each wake trailer segment. The multiple trailer wake model uses the Vatistas core model [108], [109] and the Bhagwat-Leishman core growth model [110]. Turbulence in the tip vortex affects the diffusion of vorticity, and these effects were incorporated using an empirically validated correction for the average apparent or "eddy" viscosity. The vortex induced velocity profiles measured in experiments were found to exhibit strong self-similarity when using the vortex core radius as a length-scale, suggesting that a generalized model is possible. This model accounts for the effect of both laminar and turbulent viscosities on viscous core growth. The analytical expression for the core growth is given as follows,

$$r_c = \sqrt{4\alpha\delta\nu\left(\frac{z+z_0}{V_\infty}\right)} \qquad \delta = 1 + a_1 \mathrm{Re}_\nu \tag{A.44}$$

where $\overrightarrow{r_c}$ is viscous core radius, a_1 and α are empirical parameters, V_∞ is freestream velocity.

The use of the multiple trailer model significantly increases computational time because the calculation of wake geometries scale approximately as n^2 where n is the number of wake trailers. A comparison of single tip vortex model vs. multiple trailer model on airloads predictions for UH-60A will be addressed in the next chapter.

A.7 Shed Wake Model

The multiple trailer vortex does not include the wake shed due to temporal change in bound vorticity strength. Kelvin's theorem [107] states that the circulation around a closed curve moving with the fluid remains constant with time. This means a counter-rotating vortex is shed equal in magnitude to the change in bound circulation. This additional wake is modeled through a shed wake model. The effect of the shed wake on the source blade is adequately captured by the Navier-Stokes solution but its effect on adjacent blades needs to be modeled. The vorticity strength of wake element shed between trailer n and $n+1$ at azimuth Ψ is given as follows,

$$\Gamma_{sh}(\Psi, n) = \Gamma(\Psi, n) - \Gamma(\Psi - \Delta\Psi, n) \tag{A.45}$$

A.8 Computational Time

The efficiency of the hybrid methodology depends on the computational grid resolution, the order of the numerical scheme used in discretization, and the type of the wake model. In this study, hover calculations typically required 5 rotor revolutions. The total computational time is 10 hours per case on a 24 core workstation; for forward flight, which requires 4 revolutions, approximately 6 hours are needed to complete the simulations on the same workstation.

APENDIX B

B.1 STAR-CCM+ Numerical Methodology

STAR-CCM+ has several solvers within the commercial package, and each solver is tailored for a specific set of flow conditions. The solver used in the present study models air as a compressible ideal gas, and the turbulence parameters are modeled by solving the RANS equations with Menter's $k-\omega$ SST model [100]. The conservation equations for mass and momentum are solved simultaneously using implicit spatial interpolation in an unsteady analysis with a coupled algebraic multi-grid method [101].

B.2 Temporal and Spatial Discretization

The wake-capturing simulations performed using STAR-CCM+ employ a density-based approach where the conservation of mass, the momentum equations and the energy equations are coupled and solved simultaneously at each time step. The integral form of Navier-Stokes equations is used for a fixed, arbitrary control volume V with differential surface area $d\boldsymbol{A}$, as shown below.

$$\Gamma \frac{\partial}{\partial t}\int_V \boldsymbol{W} dV + \oint [\boldsymbol{F} - \boldsymbol{G}] \cdot d\boldsymbol{A} = \int_V \boldsymbol{S} dV \tag{B.1}$$

Here $\boldsymbol{W}$ is the vector of primitive variables in the Navier-Stokes equations, Γ is a preconditioning matrix, $\boldsymbol{F}$ and $\boldsymbol{G}$ are the convective and diffusive flux vectors, and $\mathbf{S} = [0, \rho\Omega \times \mathrm{u}, 0]^T$ is the source vector associated with the rotation of the reference frame at an angular velocity Ω.

$$\boldsymbol{W} = \begin{Bmatrix} \rho \\ \rho u \\ \rho v \\ \rho w \\ e \end{Bmatrix}$$

The fluid is assumed to be Newtonian, and the influence of the gravity on the flow is negligible.

B.3 Surface and Volume Integrals for flux calculation

The surface integrals in Equation B.2 above are evaluated on two levels using quadrature approximations:

The integral is expressed in terms of variable values at one location on the cell face. STAR-CCM+ employs the second-order midpoint rule, that is, the integral is evaluated as the product of the value at the cell face center and the cell face area:

$$\int_A \boldsymbol{\Phi} d\boldsymbol{a} \approx \sum_s \boldsymbol{\Phi}_s \, \boldsymbol{a}_s \tag{B.2}$$

where $\boldsymbol{\Phi}$ could be the convective or the diffusive flux of fluid property, and $\boldsymbol{a}_s$ is the surface area vector of face s of the cell. The values at the cell face center are evaluated through a numerical (linear) interpolation of the values at the neighbor corners (cell nodes). The integrals are computed at any cell associated with the node $(i\,, j, k)$ on the six cell faces $(i \pm 1/2, j \pm 1/2, k \pm 1/2)$. Thus, this scheme is spatially second order accurate.

An upwind scheme is used. The flow solver has numerous choices (flux splitting, and flux difference splitting). In the present work, the convective flux is approximated by a step function:

$$(\dot{m}\boldsymbol{F})_s = \begin{cases} \dot{m}_s F_{s,0} & if \quad \dot{m}_s > 0 \\ \dot{m}_s F_{s,1} & if \quad \dot{m}_s < 0 \end{cases} \tag{B.3}$$

where $F_{s,0}$ and $F_{s,1}$ are the linearly interpolated central convective value calculated from the side of the surface with positive properties flux. The gradients are reconstructed with limiters which bound the maximum and minimum values of the local gradients.

The diffusive flux term is discretized similarly to the convective flux term, but with an extra gradient term [101] [100]. The source term in Equation B.2 requires integration over the volume of the cell. The code approximates the volume integral as the product of the mean value of the source term at the cell center and the volume of the cell. This approximation maintains the overall second-order accuracy of the solution. To ensure second-order spatial accuracy of the discretization on stretched grids, the values of the interested properties at the node center are area weighted or volume weighted using values from the adjacent nodes.

B.4 Time Discretization

In the present work, simulations are performed using a second-order time-accurate scheme with dual-time sub-iterations. That is, for each physical time step, 10 to 20 sub-iterations are conducted to reach a values of the flow properties at the following time step.

In order to expedite the convergence of the simulation, a multi-grid method is also applied in the study. The simulation starts on a coarse mesh at every time step, and switches to a fine mesh when the low frequency components of the errors are dissipated within a few iterations on the coarse mesh. As a result, multi-grid methodology can significantly reduce the overall computational time. In addition to simply switch from a coarser mesh to a finer mesh, there are levels of mesh densities defined in the program, and a V-Cycle is used to define how many levels of grid densities are needed and to control how many iterations are needed at each coarse grid levels.

B.5 Overset Grid Methodology

Overset mesh topology is used in the present STAR-CCM+ full wake model simulations. Compared with other mesh topologies, overset mesh is favorable for simulations with complex motions and complicated geometries. Rotor performance simulation is precisely one of the cases. The S76 rotor blades have a large aspect ratio and consist of three airfoil shapes. That means, for a 3D simulation, a well captured boundary layer and blade shape at leading & trailing edge require a large number of nodes (or control volume cells) surrounding the blade. If this grid is extended all the way to far field boundaries, a highly skewed and highly stretched mesh would arise. However, with an overset mesh topology, the skewness can be dramatically decreased. Overset mesh topology also gives more freedom for placing embedded fine meshes in regions of interest.

Overset mesh separates the mesh into two parts: near-body region and background region. The near-body region needs not to be very large and the background mesh does not need to be too dense. The near-body mesh moves with the solid body, in this case the blade, with

proper control of pitching and flapping angles. The background mesh is stationary. It receives the near body mesh information and feeds far field information to the moving region. It is a time marching process, and flow field information is continuously exchanged several times during the sub-iterations within a single time step

An example of overset mesh near the body and in the background region is shown in Figure 37.

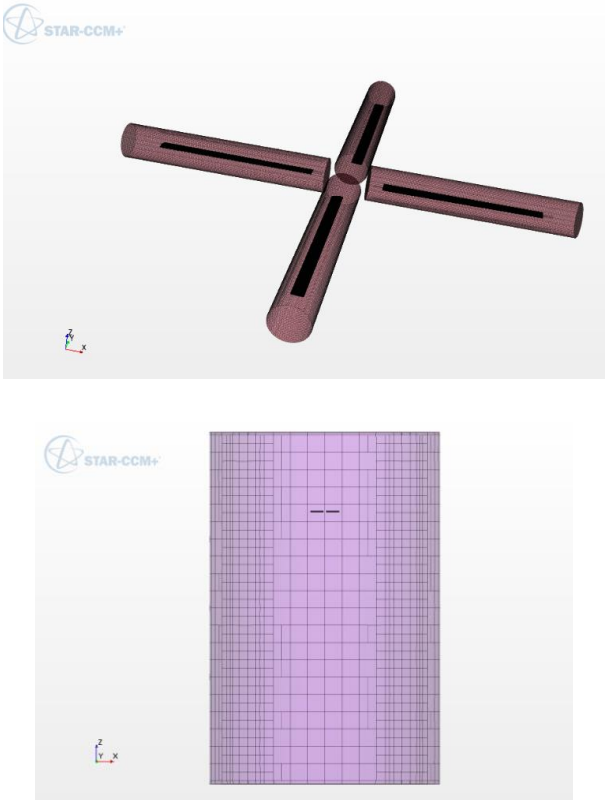

Figure 37 Mesh example (transparent view) of the overset mesh topology: near body region (Left) and background region (Right)

In an overset mesh, cells are categorized into three classes: active, inactive, or acceptor cells. In active cells, discretized form of the governing equations are solved. Inactive cells

are not involved in the simulation, but they can become active if the space they occupy gets out of the non-fluid region (e.g. inside rotor blade). Acceptor cells are a layer of cells separating active and inactive cells in the background region and are attached to the overset boundary in the overset region. They work as the interface for information communication between the two regions. The values of the parameter are sent from one region to the acceptor cells of another region, through interpolations. The direction of the information flow depends on the nearest distance from the two acceptors (one is called donor, and the pother is called acceptor). The interpolation method applied in the case is the linear interpolation.

The discretized form of equations are iteratively solved for all active cells in the whole computational domain which means all the values in all the regions are computed at the current time step. Therefore, there are two sets of values available at the acceptor and donor region. When a value in an acceptor cell is needed to solve the control equations at the current time step, the available values at donor cells from the other region are used. This tight coupling of the overset and background regions allows for a solution that is within an arbitrary low level of iteration errors. The rate of convergence of the iterative solution method is therefore similar to that of a single mesh of the same resolution [101].

B.6 Computational Time

Due to starting the solution from quiescent flow conditions, a starting vortex was manifested in the flow domain. In order to convect the starting vortex out of the flow domain to reach the equilibrium state, the solution was computed for 20 rotor revolutions.

A physical time step of 1 degree azimuth with 15 sub iterations at the equilibrium state was found to be sufficient (it may need more sub-iterations at the beginning of the simulation from CFD stability concern).

The overall computational time for each run with settings shown above is on the order of 90 CPU hours per case, using 60 cores on a Linux Cluster. It is reasonable for rotor simulations, but it is still relatively computational expensive for the large number of simulations conducted in this research. Therefore, the hybrid RANS – free wake methodology is first used to model the rotor, and trim the collective pitch (for a specific thrust setting) before switching to STAR-CCM+.

REFERENCES

[1] H., Glauert, Airplane propellers, Springer, Berlin, Heidelberg, 1935.

[2] M. Y., George, et al, "Attack Helicopter Evaluation, Blackhawk S-67 Helicopter," National Technical Information Service, Edwards Air Force Base, CA, July 1972.

[3] T. Y., William , "Performance and Vibratory Loads Data From a Wind-Tunnel Test of a Model Helicopter Main-Rotor Blade With a Paddle-Type Tip," ARL Technical Report 1283, May 1997.

[4] M. McVeigh, F.J., McHugh, "Influence of tip shape, chord, blade number, andairfoil on advanced rotor performance," *Journal of the American Helicopter Society*, p. 55–62, 1984.

[5] Abras, J., Hariharan, N., "Performance Impact of Tip Shape Variations on the S-76 Rotor Using kCFD," in *AIAA SciTech 54th Aerospace Sciences Meeting*, San Diego, CA, 4-8 January 2016.

[6] Balch, D., and J.Lombardi, "Experimental Study of Main Rotor Tip Geometry and Tail Rotor Interactions in Hover," *National Aeronautics and Space Administration*, vol. 1, 1985.

[7] Muller R., "The influence of winglets on rotor aerodynamics," in *12th European rotorcraft forum*, 1986.

[8] Muller R., " Winglets on rotorblades in forward flight—a theoretical and experimental investigation," in *14th European rotorcraft forum*, Milano, Italy, 1988.

[9] Muller R., "Special vortices at a helicopter rotor blade," *Journal of the American Helicopter Society,* vol. 35, no. 4, p. 16–22, 1990.

[10] Brocklehurst, A. and Barakos, G. N., " A Review of Helicopter Rotor Blade Tip Shapes," *Progress in Aerospace Sciences,* vol. 56, pp. 35-74, 2013.

[11] Abras, J. N., and Hariharan, N., "Parameter Studies on the S-76 Rotor Using Helios," in *55th AIAA Aerospace Sciences Meeting,* Grapevine, Texas, 2017.

[12] Balch, D. T., "Full-Scale Wind Tunnel Tests of a Modern Helicopter Main Rotor Correlation with Model Rotor Test Data and with Theory," in *Annual National Forum of The American Helicopter Society*, Washington, D. C., May 1978.

[13] Balch, D., and J.Lombardi, "Experimental study of main rotor tip geometry and tail rotor interactions in hover. Volume 2: Run log and tabulated data," *National Aeronautics and Space Administration,* vol. 2, 1985.

[14] Johnson, W., "Performance and Loads Data From a Wind Tunnel Test of a Full-Scale Rotor With Four Blade Tip Planforms," NASA Technical Memorandum 81229, ADA091690.

[15] "AIAA Applied Aerodynamics Rotorcraft Working Group,https://info.aiaa.org/tac/ASG/APATC/Web%20Pages/RotorSim-DG_Info.aspx".

[16] Jain, R., "A Comparison of CFD Hover Predictions for the Sikorsky S-76 Rotor," in *AIAA SciTech 54th Aerospace Sciences Meeting*, San Diego, CA, 4-8 January 2016.

[17] Hwang, J., Choi, J., Kwon, O., "Assessment of S-76 Rotor Hover Performance in Ground Effect Using an Unstructured Mixed Mesh Method," in *AIAA SciTech 54th Aerospace Sciences Meeting*, San Diego, CA, 4-8 January 2016.

[18] Gardarein, P., Le Pape, A., "Numerical Simulation of Hover S-76 Helicopter Rotor Including Far-Field Analysis," in *AIAA SciTech 54th Aerospace Sciences Meeting*, San Diego, CA, 4-8 January 2016.

[19] Duque, E., Toyoda, M., Burklund, M., Hariharan, N., Narducci, R., Stone, C., "Direct Comparison of Hover Prediction Workshop Results," in *AIAA SciTech 54th Aerospace Sciences Meeting*, San Diego, CA, 4-8 January 2016.

[20] Hariharan N., Egolf T.A., Sankar, L.N., "Simulation of Rotor in Hover: Current State and Challenges," in *AIAA SciTech 52nd Aerospace Sciences Meeting*, National Harbor, Maryland, 13-17 January 2014.

[21] Barakos, G., "Accurate Predictions of Hovering Rotor Flows Using CFD," in *AIAA SciTech 55th Aerospace Sciences Meeting*, Grapevine, TX, 9-13 January 2017.

[22] Sheng, C., Zhao, Q., Hill, M., "Investigation of XV-15 Rotor Hover Performance and Flow Field Using U2NCLE and Helios Codes," in *AIAA SciTech 54th Aerospace Sciences Meeting*, San Diego, CA, 4-8 January 2016.

[23] Sheng, C., et al., "S76 Main Rotor Hover Performance Predictions Using U2NCLE Solver," in *AIAA SciTech*, National Harbor, MD, January 2014.

[24] Jain, R.K., Potsdam, M.A., "Hover Predictions on the Sikorsky S-76 Rotor using Helios," in *AIAA SciTech 52nd Aerospace Sciences Meeting*, National Harbor, Maryland, 13-17 January 2014.

[25] Narducci, R., "OVERFLOW Simulation of Rotors in Hover: The Boeing Company," in *AIAA SciTech 52nd Aerospace Sciences Meeting*, National Harbor, Maryland, 13-17 January 2014.

[26] Tadghighi, H., "Helios Simulation of Rotors in Hover: The Boeing Company," in *AIAA SciTech 52nd Aerospace Sciences Meeting*, National Harbor, Maryland, 13-17 January 2014.

[27] Wong, T-C., "Application of CREATE-AV Helios in Engineering Environment Hover Prediction Assessment," in *AIAA SciTech 55th Aerospace Sciences Meeting*, Grapevine, TX, 9-13 January 2017.

[28] Jacobson, K., Grubb, A., Smith, M., "Performance and Physics of an S-76 Rotor in Hover with Non-Contiguous Hybrid Methodologies," in *AIAA SciTech 54th Aerospace Sciences Meeting*, San Diego, CA, 4-8 January 2016.

[29] Jung et al., "Assessment of Rotor Aerodynamic Performance in Hover Using an Unstructured Mixed Mesh Method," in *AIAA SciTech*, National Harbor, MD, January 2014.

[30] Abras, et al., "Parameter Studies on the S-76 Rotor Using Helios," in *AIAA SciTech 55th Aerospace Sciences Meeting*, Grapevine, TX, 9-13 January 2017.

[31] Barakos, G., Jimenez-Garcia, A., "Hover Predictions of the S-76 Rotor using HMB2 – Model to Full Scale," in *AIAA SciTech 54th Aerospace Sciences Meeting*, San Diego, CA, 4-8 January 2016.

[32] Baeder, J.D., Medida, S., Kalra, T.S., "OVERTURNS Simulations of S-76 Rotor in Hover," in *AIAA SciTech 52nd Aerospace Sciences Meeting*, National Harbor, Maryland, 13-17 January 2014.

[33] Tadghighi, H., "Simulations of Rotor in Hover: Boeing Mesa," in *AIAA SciTech* , National Harbor, MD, January 2014.

[34] Hariharan N., Egolf T.A., Narducci, R., Sankar, L.N., "Helicopter Rotor Aerodynamic Modeling in Hover: AIAA Standardized Hover Evaluations," in *AIAA SciTech 53rd Aerospace Sciences Meeting*, Kissimmee, Florida, 5-9 January 2015.

[35] Narducci, R., "Hover Performance Assessment of Several Tip Shapes using OVERFLOW," in *AIAA SciTech 53rd Aerospace Sciences Meeting*, Kissimmee, Florida, 5-9 January 2015.

[36] Jain, R., "Hover Predictions for the S-76 Rotor with Tip Shape Variation using CREATE-AV Helios," in *AIAA SciTech 53rd Aerospace Sciences Meeting*, Kissimmee, Florida, 5-9 January 2015.

[37] Duque et al., "Standardized Post-Processing and Visualization of Participants Simulations of Rotor in Hover," in *AIAA SciTech 55th Aerospace Sciences Meeting*, Grapevine, TX, 9-13 January 2017.

[38] Anusonti-Inthra, P., "The Effects of Turbulence Modelings on CFD Simulations of S76 Hovering Rotor," in *AIAA SciTech 53rd Aerospace Sciences Meeting*, Kissimmee, Florida, 5-9 January 2015.

[39] Narducci, R., "Comparison of Steady-state and Time-dependent Solutions for the S-76 Model-Scale Rotor in Hover," in *AIAA SciTech 55th Aerospace Sciences Meeting*, Grapevine, TX, 9-13 January 2017.

[40] Hariharan N., Narducci, R., Egolf, T.A., Reed, E., "Helicopter Rotor Aerodynamic Modeling of S-76 Rotor with Tip-Shape Variations," in *54th Aerospace Sciences Meeting*, San Diego, CA, 4-8 January 2016.

[41] Whitehouse, G.R., Wachspress, D.A., Quackenbush, T.R., "Predicting the Influence of Blade Tip Shape on Hovering Rotor Performance with Comprehensive Analyses," in *AIAA SciTech 53rd Aerospace Sciences Meeting*, Kissimmee, Florida, 5-9 January 2015.

[42] Kim, J.W., Sankar, L.N., Marpu, R., Egolf, T.A., Hariharan, N., "Assessment of Planform Effects on Rotor Hover Performance," in *AIAA SciTech 53rd Aerospace Sciences Meeting*, Kissimmee, Florida, 5-9 January 2015.

[43] Brocklehurst A., Barakos, G.N., "Evaluating Tail Rotor Tip Shapes using Computational Fluid Dynamics," in *AIAA SciTech 52nd Aerospace Sciences Meeting*, National Harbor, Maryland, 13-17 January 2014.

[44] Sankar et al., "Application of Hover Prediction Methodologies to Anhedral Tip Shapes," in *AIAA SciTech 55th Aerospace Sciences Meeting*, Grapevine, TX, 9-13 January 2017.

[45] Smith, M.J., Jacobson, K.E., Grubb, A.L., Daniel A. Wachspress, D.A., Whitehouse, G.R, "Evaluation of Rotor Hover Performance With Differing Blade Tip Shapes Using A Carefree Hybrid Methodology," in *AIAA SciTech 53rd Aerospace Sciences Meeting*, Kissimmee, Florida, 5-9 January 2015.

[46] Walther, J.H., et al., "A numerical study of the stability of helical vortices using vortex methods," *Journal of Physics*, 2007.

[47] Widnall, S., "The stability of a helical vortex filament," *Journal of Fluid Mechanism*, vol. 54, pp. 641-663, 1972.

[48] Sheng, C., Wang, J., Zhao, Q., "S-76 Rotor Hover Predictions Using Advanced Turbulence Models," in *AIAA SciTech 53rd Aerospace Sciences Meeting*, Kissimmee, Florida, 5-9 January 2015.

[49] Coder, J., "OVERFLOW Rotor Simulations Using Advance Turbulence and Transition Models," in *AIAA SciTech 55th Aerospace Sciences Meeting*, Grapevine, TX, 9-13 January 2017.

[50] Viera, B., "CFD Hover Predictions Including Boundary Layer Transition," in *AIAA SciTech 55th Aerospace Sciences Meeting*, Grapevine, TX, 9-13 January 2017.

[51] Jain, R., "CFD Performance and Turbulence Transition Predictions on an Installed Model-Scale Rotor in Hover," in *AIAA SciTech 55th Aerospace Sciences Meeting*, Grapevine, TX, 9-13 January 2017.

[52] Overmeyer, A., et al., "Measured Boundary Layer Transition and Rotor Hover Performance at Model Scale," in *AIAA SciTech 55th Aerospace Sciences Meeting*, Grapevine, TX, 9-13 January 2017.

[53] Hwang, J.Y., Choi, J.H., Kwon, O.J., "Assessment of S-76 Rotor Aerodynamic Performance in Hover on Unstructured Mixed Meshes," in *AIAA SciTech 53rd Aerospace Sciences Meeting*, Kissimmee, Florida, 5-9 January 2015.

[54] Min, B.Y., Wake, B., "Analysis of a Hovering Rotor using UT-GENCAS: A Modified Hybrid NavierStokes/Free-Wake Method," in *AIAA SciTech 53rd Aerospace Sciences Meeting*, Kissimmee, Florida, 5-9 January 2015.

[55] Jung, M.K., Hwang, J.Y., Kwon, O.J., "Assessment of Rotor Aerodynamic Performances in Hover Using an Unstructured Mixed Mesh Method," in *AIAA SciTech 52nd Aerospace Sciences Meeting*, National Harbor, Maryland, 13-17 January 2014.

[56] Lee et al., "Methods for Efficient Resolution of Vortical Structures of an S-76 Rotor in Hover," in *AIAA SciTech 55th Aerospace Sciences Meeting*, Grapevine, TX, 9-13 January 2017.

[57] Abras, J.N., Hariharan, N., "Comparison of CFD Hover Predictions on the S-76 Rotor," in *AIAA SciTech 53rd Aerospace Sciences Meeting*, Kissimmee, Florida, 5-9 January 2015.

[58] Garcia, A.J., Barakos, G.N., "Hover Predictions on the S-76 Rotor using HMB2," in *AIAA SciTech 53rd Aerospace Sciences Meeting*, Kissimmee, Florida, 5-9 January 2015.

[59] Chaderjian, N., Buning, P., "High Resolution Navier-Stokes Simulation of Rotor Wakes," in *AHS 67th Annual Forum*, Virginia Beach, VA, May 3-5, 2011.

[60] Barakos, George N., "Evaluating Rotor Tip Shapes Using Computational Fluid Dynamics," in *AIAA SciTech 2014*, National Harbor, MD, January 2014.

[61] Jain et al., "Hover Predictions for the S-76 Rotor Using Helios," in *AIAA SciTech*, National Harbor, MD, January 2014.

[62] Brocklehurst, A., Barakos, G., "A review of helicopter rotor blade tip shapes," *Progress in Aerospace Sciences*, vol. 56, pp. 35-74, 2013.

[63] Glauert, H. , The Airscrew: Blade Element Theory. In The Elements of Aerofoil and Airscrew Theory (Cambridge Science Classics, pp. 208-221), Cambridge: Cambridge University Press, 1983.

[64] Gray, R.B., "An aerodynamic analysis of a single-bladed rotor in hovering and low speed forward flight as determined from the smoke studies of the vorticity distribution in the wake," Princeton Aeronautical Engineering Department Report 356 , 1956.

[65] Landgrebe, A.J., "An analytical and experimental investigation of helicopter rotor hovering performance and wake geometry characteristics," United States Army Air Mobility Research and Development Laboratory, USAAMRDL TR 71-24, 1971.

[66] Scully, M.P., "A method of computing helicopter vortex wake distortion," Massachusetts Institute of Technology, Report ASRL TR 138-1, 1967.

[67] Bhagwat, M.J., Leishman, J.G., "Stability, consistency and convergence of time-marching free-vortex rotor wake algorithms. J. Am.," *Helicopter Society*, vol. 46, no. 1, p. 59–71, 2001.

[68] A. J., Landgrebe, R. C., Moffitt, D. R., Clark, "Aerodynamic Technology for Advanced Rotorcraft," *Journal American Helicopter Society*, vol. 22, no. 2, pp. 21-27, April and July 1977.

[69] Cole, J. D., Murman,E. M., "Calculation of plane steady transonic flows," *AIAA Journal*, vol. 9, no. 1, pp. 114-121, 1971.

[70] Francis, X. C., MORRIS, P. I., "Subsonic and Transonic Potential Flow over Helicopter Rotor Blades," *AIAA Journal*, vol. 10, no. 12, 1972.

[71] Philippe, J. J., Chattot, J. J. , "Preliminary Study of Transonic Flows Past Helicopter Rotor Blade Tips," 1975.

[72] Philippe, J. J., Chattot, J. J., "Experimental and Theoretical Studies on Helicopter Blade Tips at ONERA," in *6th European Rotorcraft and Powered Lift Aircraft Forum*, Bristol, England, Proceedings, Septermber, 1980.

[73] Tung, C., Caradonna, F. X., Johnson, W. R., "The Prediction of Transonic Flows on an Advancing Rotor," *Journal of the American Helicopter Society,* vol. 31, no. 3, July 1986.

[74] Sankar, L. N., Prichard, D., "Solution of transonic flow past rotor blades using the conservative full potential equation," in *3rd Applied Aerodynamics Conference*, AIAA paper 1985-5012.

[75] Strawn, R. C. and Caradonna, F. X., "Conservative full-potential model for unsteady transonic rotor flows," *AIAA Journal,* vol. 25, no. 2, 1987.

[76] Steger, J. L., "Implicit Finite Difference Simulation of Flow About Arbitrary Two Dimensional Geometries," *AIAA Journal,* vol. 16, no. 7, July 1978.

[77] "Thomas H. Pulliam and Joseph L. Steger. "Implicit Finite-Difference Simulations of Three-Dimensional Compressible Flow," *AIAA Journal,* vol. 18, no. 2, pp. 159-167, 1980.

[78] Sankar, L.N., Wake, B.E., Lekoudis, S.G., "Solution of the Unsteady Euler Equations for Fixed and Rotor Wing Configurations," *Journal of Aircraft,* vol. 23, no. 4, pp. 283- 289, 1986.

[79] Sankar, L.N., Tung, C., "Euler Calculations for Rotor Configurations in Unsteady Forward Flight," in *Proceedings of the 42nd Annual Forum of the American Helicopter Society*, Washington, DC,, June 1986.

[80] Wake, B. E., Sankar, L. N., "Solutions of the Navier- Stokes Equations for the Flow About a Rotor Blade," in *Journal of the American Helicopter Society*, April 1989.

[81] Agarwal, R., "Navier-Stokes calculations of the flowfield of a helicopter rotor in hover," in *26th Aerospace Sciences Meeting*, 1988-106.

[82] Srinivasan, G. R., Baeder, J. D., Obayashi, S., Mccroskey, W. J., "Flowfield of a lifting rotor in hover - A Navier-Stokes simulation," *AIAA Journal*, vol. 30, no. 10, pp. 2371-2378, 1992.

[83] Earl, D., "A Numerical Analysis of the British Experimental Rotor Program Blade," *Journal of American Helicopter Society*, vol. 37, no. 46, 1989.

[84] Brocklehurst, A., Duque, E.P.N., "Experimental and Numerical Study of the British Experimental Rotor Programme Blade," in *8th Applied Aerodynamics Conference*, Portland, Oregon, August 1990.

[85] Perry, F.J., "Aerodynamics of the World Speed Record," in *43rd Annual Forum of the American Helicopter Society*, May, 1987.

[86] Harrison, R., Stacey, S., Hansford, R., "BERP IV. The Design, Development and Testing of an Advanced Rotor Blade," in *64th Annual Forum of the American Helicopter Society*, May, 2008.

[87] Srinivasan, G. R., Baeder, J. D. , "TURNS: A Free-Wake Eule/Navier-Stokes Numerical Method for Helicopter Rotors," *AIAA Journal*, vol. 31, no. 5, pp. 959-962, 1993.

[88] Marpu, R., Zhou, C., Kim, J., and Sankar, L. N., "A Comparative Study of Two Hover Prediction Methodologies," in *AIAA SciTech Forum*, San Diego, California,, 4-8 January 2016.

[89] Tsukahara T, Ota T, Obukata M, Araki R, Obayashi S, Nakahashi K. , "Numerical analysis around rotor blade by vortex confinement," in *58th annual forum of the American Helicopter Society*, Montreal, Quebec, Canada, 2002.

[90] O'Regan, M. S.,Griffin, P. C.,Young, T. M., " A vorticity confinement model applied to URANS and LES simulations of a wing-tip vortex in the near-field," *International Journal of Heat and Fluid Flow*, vol. 61, pp. 355-365, 2016.

[91] R., Narducci, et.al, "OVERFLOW Simulation of Rotors in Hover: The Boeing Company," in *52nd Aerospace Sciences Meeting*, National Harbor, Maryland , 13-17 January 2014.

[92] J. D. Baeder, et. al, "OVERTURNS Simulations of S-76 Rotor in Hover," in *52nd Aerospace Sciences Meeting* , National Harbor, Maryland , 13-17 January 2014.

[93] R. K., Jain, M. A. Potsdam, "Hover Predictions on the Sikorsky S-76 Rotor using Helios," in *52nd Aerospace Sciences Meeting*, National Harbor, Maryland, 13-17 January 2014.

[94] Z., Liu, J., Kim, L. N., Sankar, N., Hariharan, T. A., Egolf, "High Order Evaluation of S-76 in Hover," in *53rd AIAA Aerospace Sciences Meeting*, Kissimmee, Florida, 5-9 January 2015.

[95] Narducci R., "Hover Performance Assessment of Several Tip Shapes using OVERFLOW," in *53rd AIAA Aerospace Sciences Meeting*, Kissimmee, Florida, 5-9 January 2015.

[96] "The Study and Analysis of Using Wing Dihedral on the Side of an Aircraft's Static Stability," *World Congress on Engineering*, vol. 2, 2015.

[97] G. S., BIR, I., CHOPRA , "Aeromechanical Stability of Rotorcraft with Advanced Geometry Blades," *Mathl. Comput. Modelling* , vol. 19, no. 314, pp. 159-191, 1994 .

[98] M., Imiela, G., Wilke, "Passive Blade Optimization and Evaluation in Off-Design Conditions," 2013.

[99] Hollands, M., "Influence Of An-/Dihedral And Of Different Blade Shapes On Performance And Aeroacoustics Of An Isolated Rotor," 2012.

[100] Menter, F.R., "Two-equation eddy-viscosity turbulence modeling for engineering applications," *AIAA Journal*, vol. 32, no. 8, pp. 1598-1605.

[101] Hadzic, H., "Development and application of Finite Volume Method for the Computation of Flows Around Moving Bodies on Unstructure, Overlapping Grids," Ph.D. Dissertation, Technische Universität Hamburg-Haburg.

[102] Yoon, S., and Jameson, A., "Lower-upper Symmetric-Gauss-Seidel method for the Euler and Navier-Stokes equations," *AIAA Journal* , vol. 26, no. 9, pp. 1025-1026, 1988.

[103] Van Albada, G., Van Leer, B., and Roberts Jr, W., "A comparative study of computational methods in cosmic gas dynamics," *Astronomy and Astrophysics*, vol. 108, pp. 76-84, 1982.

[104] Vinokur, M., and Liu, Y., "Equilibrium gas flow computations. II-An analysis of numerical formulations of conservation laws," *26th AIAA Aerospace Sciences Meeting*, vol. 1, 1988.

[105] Hariharan, N., Egolf, T. A., and Sankar, L. N., "Simulation of Rotor in Hover: Current State, Challenges and Standardized Evaluation," in *52nd Aerospace Sciences Meeting*, National Harbor, Maryland, 2014-0041.

[106] Pope, S., Turbulent Flows, Cambridge: Cambridge University Press, doi:10.1017/CBO9780511840531.

[107] Van Leer, B., "Towards the ultimate conservative difference scheme. V. A second-order sequel to Godunov's method," *Journal of computational Physics*, vol. 32, no. 1, pp. 101-136, 1979.

[108] Vatistas, G. H., Kozel, V., and Mih, V. , "A simpler model for concentrated vortices," *Experiments in Fluids*, vol. 11, no. 1, pp. 73-76, 1991.

[109] Vatistas, G. H., "New model for intense self-similar vortices," *Journal of Propulsion and Power*, vol. 14, no. 4, pp. 462-469, 1998.

[110] Caradonna, F.X., and Tung, C., "Experimental and Analytical Studies of a Model Helicopter Rotor in Hover," NASA TM 81232, 1981.

[111] Lorber, P.F., et al., "A Comprehensive Hover Test of the Airloads and Airflow of an Extensively Instrumented Model Helicopter Rotor," *American Helicopter Society*, pp. 281-295, 1989.

[112] Marpu, R., Sankar, L. N., Egolf, T. A., and Hariharan, N., "Simulation of S-76 Rotor in Hover Using a Hybrid Methodology," in *AIAA SciTech*, January 2014.

[113] Baeder, J., Medida, S., "OVERTURNS Simulation of S-76 Rotor in Hover," in *AIAA SciTech Forum*, National Harbor, MD, January 2014.

[114] Sheng, C., Zhao, Q., Wang, J., "S-76 Rotor Hover Prediction Using U2NCLE Solver," in *AIAA SciTech Forum*, National Harbor, Maryland, January 2014.

[115] Jain, R. K., and Potsdam, M., "Hover Predictions on the Sikorsky S-76 Rotor using Helios," in *AIAA SciTech Forum*, January 2014.

[116] Barakos, George N., "Evaluating Rotor Tip Shapes Using Computational Fluid Dynamics," in *AIAA SciTech Forum*, National Harbor, MD, January 2014.

[117] Jung, M. K., Hwang, J. Y., and Kwon, O. J., "Assessment of Rotor Aerodynamic Performance in Hover Using an Unstructured Mixed Mesh Method," in *AIAA SciTech Forum*, National Harbor, MD, January 2014.

[118] Tadghighi H., "Helios Simulation of Rotors in Hover: The Boeing Company," in *AIAA SciTech Forum*, National Harbor, MD, January 2014.

[119] Narducci R., "Simulations of Rotor in Hover: Boeing Philadelphia," in *AIAA SciTech Forum*, National Harbor, MD, January 2014.

[120] Caradonna, F. X., "The Transonic Flow on a Helicopter Rotor," Ph.D. Dissertation, Stanford University, March 1978.

[121] Caradonna, F. X. and Philippe, J. J., "The Flow over a Helicopter Blade Tip in the Transonic Regime," *Second European Rotorcraft and Powered Lift Aircraft Forum*, vol. 2, pp. 43-60, 1978.

[122] Philippe, J. J. and Chattot, J. I., "Experimental and Theoretical Studies on Helicopter Blade Tips at ONERA," in *Sixth European Rotorcraft and Power Lift Aircraft Forum*, Bristol, U.K., Sept 1980.

[123] Monnerie, B. and Phillippe, J. J., "Aerodynamic Problems of Helicopter BladeTips," in *3th European Helicopter Forum*, Verfica, Val. 2, 1978, pp. 217-231.

[124] Sankar, L. N., and Prichard, D., "Solution of transonic flow past rotor blades using the conservative full potential equation," in *3rd Applied Aerodynamics Conference*, *AIAA Paper* , Colorado Spring, CO, October 14-16, 1985.

[125] Strawn, R. C. and Caradonna, F. X., "Conservative full-potential model for unsteady transonic rotor flows," *AIAA Journal*, vol. 25, no. 2, pp. 193-198, 1987.

[126] Steinhoff, J. and Ramachandran, K., "Free-Wake Analysis of Compressible Rotor Flows," *AIAA Journal*, vol. 28, no. 2, pp. 426-431, 1989.

[127] Tapia, F., Sankar, L. N., Schrage, D. P., "An Inverse Aerodynamic Design Method for Rotor Blades in Forward Flight," *Journal of the American Helicopter Society*, vol. 42, no. 4, pp. 321-326(6), 1 October 1997.

[128] Sankar, L.N. and Tung, C., "Euler Calculations for Rotor Configurations in Unsteady Forward Flight," in *42nd Annual Forum of the American Helicopter Society*, Washington, DC, June 1986.

[129] Agarwal,R. K. and Deese, J. E., "Euler calculations for flow field of a helicopter rotor in hover," *Journal of Aircraft*, vol. 24, no. 4, pp. 231-238, 1987.

[130] Wake, B. E. and Sankar, L. N., "Solutions of the Navier- Stokes Equations for the Flow About a Rotor Blade," *Journal of the American Helicopter Society*, vol. 34, pp. 13-23, April 1989.

[131] Srinivasan, G. R. and Mccroskey, W. J. , "Navier-Stokes calculations of hovering rotor flowfields," *Journal of Aircraft*, vol. 25, no. 10, pp. 865-874, 1988.

[132] Duque E. P. N., Srinivasan GR. , "Numerical simulation of a hovering rotor using embedded grids," in *48th annual national forum of the American Helicopter Society*, Washington, DC, February 1992.

[133] Srinivasan, G. R., Ragavan V, Duque, E. P. N., McCroskey, W. J., "Flowfield analysis of modern helicopter rotors in hover by Navier–Stokes method," *AIAA Journal*, vol. 30, no. 10, pp. 2371-2378, 1993.

[134] "Jennifer N. Abras, Nathan Hariharan. 2018. Comparison of Computational Fluid Dynamics Hover Predictions on the S-76 Rotor," *Journal of Aircraft*, vol. 55, no. 1, pp. 12-22, January–February 2018.

[135] Jennifer Abras and Nathan S. Hariharan, "Parameter Studies on the S-76 Rotor Using HELIOS," in *55th AIAA Aerospace Sciences Meeting*, Grapevine, Texas, 2017.

[136] Coder, J. G., "OVERFLOW Rotor Simulations Using Advanced Turbulence and Transition Modeling," in *55th AIAA Aerospace Sciences Meeting*, Grapevine, Texas, 2017.

[137] Zhou, C., Sankar, L. N. and Griffin, P., "Effects of Anhedral on S-76 Hover Aerodynamics," in *AIAA SciTech Forum*, San Diego, California, 2019.

[138] Rajmohan, N., "Application of hybrid methodology to rotors in steady and maneuvering flight," School of Aerospace Engineering. Georgia Institute of Technology, Atlanta, GA, 2010.

[139] Steger, J. L., and Warming, R. F, "Flux vector splitting of the inviscid gasdynamic equations with application to finite-difference methods," *Journal of Computational Physics*, vol. 40, no. 2, pp. 263-293, 1981.

[140] Roe, P. L., and Pike, J., "Efficient construction and utilisation of approximate Riemann solutions," in *North-Holland Publishing Co.*, Versailles, France, 1985.

[141] Van Leer, B., "Towards the ultimate conservative difference scheme. V. A second-order sequel to Godunov's method," *Journal of computational Physics*, vol. 32, no. 1, pp. 101-136, 1979.

[142] Kuethe, A., and Chow, C.-Y., Foundations of Aerodynamics, New York: John Wiley and Sons Inc, 1998.

[143] N. Wagner, High Performance Computing in Science and Engineering, Transactions of the High Performance Computing Center, Stuttgart (HLRS), 2009.

[144] Orszag, S. A., "Analytical Theories of Turbulence," *Journal of Fluid Mechanics*, vol. 41, p. 363–386, 1970.

[145] Sullivan, P. P.; McWilliams, J. C.; Moeng, C., "A subgrid-scale model for large-eddy simulation of planetary boundary-layer flows," *Boundary-Layer Meteorology. Kluwer Academic Publishers,* vol. 71, no. 3, p. 247–276. , 1994.

[146] Clark, R., Ferziger, J., Reynolds, W. , "Evaluation of subgrid-scale models using an accurately simulated turbulent flow," *Journal of Fluid Mechanics,* vol. 91, pp. 1-16, 1979.

[147] Smagorinsky J. , "General circulation experiments with the primitive equations," *Monthly Weather Review,* vol. 91, pp. 99-165, 1963.

[148] Vreman, B., Geurts, B., Kuerten, H., "Subgrid-modelling in LES of compressible flow," *Applied Scientific Research,* vol. 45, no. 3, p. 191–203, 1995.

[149] Spalart, P. R. , "Detached-eddy simulation," *Annual Review of Fluid Mechanics,* vol. 41, p. 181–202, 2009.

[150] Bhagwat, M. J., and Leishman, J. G., "Generalized viscous vortex model for application to free-vortex wake and aeroacoustic calculations," *Annual ForAmerican Helicopter Society,* vol. 58, pp. 204-205, 2002.

[151] Spalart, P.R., "Comments on the feasibility of LES for wing and on a hybrid RANS/LES approach," in *1st ASOSR CONFERENCE on DNS/LES*, Arlington, TX., August 1997.

[152] Kotapati, R. B., Squires, K. D., and Forsythe, J. R., " Prediction of the Flow over an Airfoil at Maximum Lift," in *42nd Aerospace Sciences Meeting and Exhibit*, January 2004.

[153] Tennekes, H.; Lumley, J. L. , A first course in turbulence, Cambridge, Mass: MIT Press, 1992.

[154] Bengt, A. et al. , Computational fluid dynamics for engineers, Cambridge, MA: Cambridge University Press. p. 83. , 2012.

[155] Nicolás-Pérez, F. , et. al., "On the accuracy of RANS, DES and LES turbulence models for predicting drag reduction with Base Bleed technology," *Aerospace Science and Technology*, vol. 67, pp. 126-140, 2017.

[156] Min, B., Sankar, L, N., "Hybrid Navier–Stokes/Free-Wake Method for Modeling Blade–Vortex Interactions," *Journal of Aircraft*, vol. 47, no. 3, pp. 975-982, 2010.

[157] "A Hybrid Navier-Stokes / Viscous Vortex Particle Wake Methodology For Modeling Maneuver Loads," in *European Rotorcraft Forum* , Delft, The Netherlands, November 2018.

[158] Srivastava, R. and Sankar, L. N, "Efficient Hybrid Scheme for the Analysis of Counter-Rotating Propellers," *Journal of Propulsion and Power*, vol. 9, no. 3, 1993.

[159] Yang, Z., Sankar, L. N., Smith, M. J., and Sankar, O., "Recent Improvements to a Hybrid Method for Rotors in Forward Flight," *Journal of Aircraft*, vol. 39, no. 5, pp. 804-812, September-October 2002.

[160] Zaki, M., Menon, S., and Sankar, L. N., "Hybrid Reynolds-Averaged Navier-Stokes and Kinetic Energy Simulation of External and Internal Flows," *Journal of Aircraft*, vol. 47, no. 3, pp. 805-811, May-June 2010.

[161] Leishman, J. G., Principles of helicopter aerodynamics, Cambridge, New York : Cambridge University Press, 2006.

[162] Petersson, N. A., "Hole-Cutting for Three-Dimensional Overlapping Grids," *SIAM Journal on Scientific Computing*, vol. 21, no. 2, pp. 646-665, 1999.

[163] Phanse, S., Sankar, L. N., Charles, B. D., "Efficient Coupled Fluid Structure Interaction Approach for Analysis of Rotors in Forward Flight," in *American*

Helicopter Vertical Lift Aircraft Design Conference, San Francisco, California, January 18-29, 2006.

[164] Chasapogiannis, P., Voutsinas, S. G., "Free-wake modeling of rotor aerodynamics: recent developments and future perspectives," in *European Wind Energy Conference*, Copenhagen Denmark, 2001.

[165] Quackenbush,T. R.,Boschitsch, A. H., Wachspress, D. A. and Chua, K., "Rotor Design Optimization Using a Free Wake Analysis," NASA-CR-177612), April 1993.

[166] Komerath, N., Smith, M. J. , "Rotorcraft Wake Modeling: Past, Present, and Future," in *35th European Rotorcraft Forum*, Hamburg, Germany, January 2009.

[167] Rand, O. & Khromov, V., "Helicopter Sizing by Statistics," *Journal of the American Helicopter Society* , vol. 49, no. 3, 2004.

[168] Froude, R. E., "On the Elementary Relation Between Pitch, Slip, and Propulsive Efficiency," *Naval Arch*, vol. 19, pp. 47-65, 1878.

[169] A.F. Antoniadis, D. Drikakis, B. Zhong, G. Barakos, R. Steijl, M. Biava,Vigevano, L., et al., "Assessment of CFD methods against experimental flow measurements

for helicopter flows," *Aerospace Science and Technology,* vol. 19, no. 1, pp. 86-100, 2012.

[170] Tapia, F., Sankar, L. N., Schrage, D. P., "An Inverse Aerodynamic Design Method for Rotor Blades," *Journal of the American Helicopter Society,* vol. 42, pp. 321-326, 1997.

[171] Singh,R., Corle,Ethan ., Jain, R. and Lim, J., "Computation and Quantification of Uncertainty in Predictions of HVAB Rotor Performance in Hover," in *AIAA Scitech 2019 Forum*, San Diego, California, 2019.

[172] Lee, B, Jung, Y. S., Jude, D. and Baeder, J. D., "Turbulent Transition Prediction of PSP Hovering Rotor Using γ-Reθt-SA with Crossflow Transition Model," in *AIAA SciTech Forum*, San Diego, California, 2019.

[173] Barakos, G. N., Fitzgibbon, T.,Woodgate, M. A. and Jimenez-Garcia, A., "Numerical Simulations of Various Rotor Designs in Hover and Forward Flight," in *AIAA SciTech Forum*, San Diego, California, 2019.

[174] Carnes, J. and Coder, J. G., "Computational Assessment of the HVAB Rotor in Hover Using Laminar-Turbulent Transition Modeling," in *AIAA SciTech Forum*, San Diego, California, 2019.

[175] "AIAA Applied Aerodynamics Rotorcraft Working Group,https://info.aiaa.org/tac/ASG/APATC/Web%20Pages/RotorSim-DG_Info.aspx".